

Advanced Control Methods for Optimization of Arc Welding

Ph.D. Thesis

Jesper Sandberg Thomsen

Department of Control Engineering
Aalborg University
Fredrik Bajers Vej 7, 9220 Aalborg East, Denmark

31st May 2005

ISBN 87-90664-18-3
August 2004

Copyright 2001–2004 ©Jesper Sandberg Thomsen

This thesis was typeset using $\text{\LaTeX}2_{\epsilon}$ in `report` document class.

Preface

This thesis is submitted as partly fulfillment of the requirements for the Doctor of Philosophy at the Department of Control Engineering at the Institute of Electronic Systems, Aalborg University, Denmark. The Ph.D. study is partly sponsored by ATV (The Danish Academy of Technical Sciences), and partly sponsored by Migatronic A/S. ATV is an independent institution with the aim of promoting technological and scientific research in Danish industry. Migatronic A/S is a company which develops and produces welding machines. The subject of the thesis is development of advanced control methods for optimization of arc welding. The work has been carried out in the period September 2000 to May 2004 under the supervision of Professor Jakob Stoustrup from Aalborg University, and Martin Riisgaard-Jensen and Knud Jørgen Poulsen from Migatronic A/S. Also, Associate Professor Palle Andersen from Aalborg University and Christian Lauritsen from Migatronic A/S have been involved in the work. Moreover, the author has been a guest researcher at University of Kentucky, Lexington, USA, for seven months, visiting Professor Yu Ming Zhang.

Aalborg University, May 2004
Jesper Sandberg Thomsen

Abstract

In this thesis the objective is to optimize the control algorithms for the manual pulsed Gas Metal Arc Welding (GMAW) process, with the aim of enhancing the quality of welded joints. To be able to develop controllers for the GMAW process, and also for enabling process simulation, a mathematical model describing the GMAW process is developed. The mathematical model includes a description of the electrical circuit, the drop dynamics, and the melting rate, and also, the model includes criteria for drop detachments. Basically, the electrical circuit consists of the welding machine, the wires, the electrode, and the electrical arc. The drop is modelled as a mass-spring-damper system influenced by a number of external forces. Of these external forces the electromagnetic force is the most significant. Due to the importance of the electromagnetic force, a thorough derivation of the electromagnetic force is included in the thesis. The melting rate of the consumable electrode is modelled both from a statically (steady-state) point of view, and from a dynamically point of view. The static model is a simple equation describing the melting rate, while the dynamic model is more complex.

The structure of GMAW control is discussed, and based on this discussion a general control structure is presented. This structure includes an arc length controller and a metal transfer controller, and also, an inner loop controlling the welding current. The current is assumed to be controlled by a traditional PI-controller, and therefore, this inner control loop is not considered in the thesis. For arc length control, a nonlinear controller based on feedback linearization is proposed, and robustness and performance are considered. For metal transfer control an approach based on obtaining a uniform drop size prior to pulse initiation is proposed. This is carried out by calculating the amount of melted electrode between the current pulses during the welding process. The purpose of the uniform drop size approach is to enhance the robustness of the drop detachment process. In addition to the arc length controller and the metal transfer controller, an arc length minimization algorithm is proposed for enhancing the ability to focus the arc, and also, to minimize the heat input into the workpiece. Simulation programs for testing the controllers and algorithms have been developed, and successful tests have been carried out.

Synopsis

Denne afhandling omhandler udvikling og optimering af reguleringsalgoritmer til regulering af manuel pulseret MIG/MAG svejsning (GMAW). Det overordnede formål er i den forbindelse at opnå en bedre svejse kvalitet. For at være i stand til at udvikle regulatorer til MIG/MAG processen, og endvidere for at være i stand til at simulere processen, er der blevet opstillet en matematisk model af processen. Den matematiske model inkluderer en beskrivelse af det elektriske kredsløb, som processen udgør, og endvidere inkluderer modellen dråbedynamik, smelterate, og kriterier for dråbeafrivning. Grundlæggende består det elektriske kredsløb af svejsemaskinen, kabler, elektroden samt lysbuen. Dråben er modelleret som en masse-fjeder-dæmper system, som er påvirket af ydre kræfter. Af disse kræfter er den elektromagnetiske kraft dominerende, og af den grund er der i afhandlingen inkluderet en grundig udledning af modellen for den elektromagnetiske kraft. Smelteraten for elektroden er modelleret udfra både en statisk og en dynamisk betragtning. Disse betragtninger resulterer i en simpel statisk model, samt en mere kompleks dynamisk model.

Strukturen af den samlede regulator til MIG/MAG processen er undersøgt, og i den forbindelse er der foreslået en generel regulatorstruktur. Der er tale om en kaskadekoblet struktur, som inkluderer en regulator til regulering af lysbuelængden, en regulator til håndtering af dråbeafrivning, samt en indre strømregulator. Den indre strømregulering kan håndteres med en ordinær PI-regulator, hvorfor denne regulator ikke undersøges yderligere i afhandlingen. Til regulering af lysbuelængden er der i afhandlingen foreslået en ulineær regulator baseret på linearisering ved tilbagekobling, og endvidere er robusthed og ydeevne undersøgt for denne regulator. Til regulering af dråbeafrivning er der foreslået en algoritme, som baserer sig på at opnå en ensartet dråbestørrelse før initiering af en puls. Dette gøres ved løbende at beregne mængden af afsmeltet elektrode. Formålet med en ensartet dråbestørrelse er at opnå robusthed i afrivningsprocessen. Udover disse regulatorer er der udviklet en algoritme til minimering af lysbuelængden, idet en sådan minimering giver god fokus af lysbuen samt minimerer den tilførte varme til svejseemnet. Til test af de forskellige regulatorer og algoritmer er der udviklet en række simuleringsprogrammer, hvormed succesfulde efterprøvninger er foretaget.

Contents

1	Introduction	1
1.1	Background and Motivation	1
1.2	Objective and Focus	2
1.3	Overview of Previous and Related Work	3
1.4	Contributions	6
1.5	Thesis Outline	7
1.6	Important Remarks	10
I	Modelling the Gas Metal Arc Welding Process	11
2	The Gas Metal Arc Welding Process	13
2.1	Electrical Arc Welding in General	13
2.2	The GMAW process	15
3	The Gas Metal Arc Welding Model	19
3.1	System Overview	19
3.2	The Electrical System	21
3.3	The Electrical Arc	23
3.4	Drop Dynamics	28
3.5	Drop Detachment	37
3.6	Melting Rate	39
3.7	The GMAW model	40
3.8	Simulations	43
3.9	Discussion and Conclusion	45
4	Dynamic Melting Rate Model	51
4.1	Melting Rate	51
4.2	A Dynamic Melting Rate Model	52
4.3	A Reduced Melting Rate Model	61
4.4	Simulations	65
4.5	Discussion and Conclusion	70

CONTENTS

II	Controlling the Gas Metal Arc Welding Process	75
5	Objectives and Control Topology	77
5.1	Control and Objectives in GMAW	77
5.2	Control Configurations	79
5.3	Discussion and Conclusion	86
6	Nonlinear Arc Length Control	89
6.1	Arc Length Control	89
6.2	Dynamic Arc Length Model	90
6.3	Feedback Linearization	93
6.4	Control and Tracking	96
6.5	Uncertainty Analysis	101
6.6	Performance	113
6.7	Arc Length Reference	126
6.8	Discussion and Conclusion	127
7	Model Based Metal Transfer Control	131
7.1	Objectives and Strategies in Pulsed GMAW	131
7.2	Uniform Drop Size	139
7.3	Simulations	143
7.4	Discussion and Conclusion	149
8	Arc Length Minimization	153
8.1	Optimization by Arc Length Minimization	153
8.2	Method for Arc Length Minimization	154
8.3	Simulations	156
8.4	Discussion and Conclusion	159
III	Conclusion	161
9	Conclusions and Future Work	163
9.1	Conclusion	163
9.2	Future Work	166

IV Appendices	169
A Maxwell Stresses	171
B The Electromagnetic Force	175
B.1 The drop and solid electrode surface	179
B.2 The drop and gas surface	180
B.3 The total electromagnetic force	184
C The Pinch Effect	187
Nomenclature	195
Bibliography	203

Introduction

Gas Metal Arc Welding (GMAW) is a process used for joining pieces of metal, and probably, it is the most successful and widely used welding method in industry today. The quality of a weld is a key issue in welding, and in many cases a weld must fulfill some specific quality requirements. However, it is very difficult to handle or control the GMAW process for the welder (human operator), and therefore, it might not be possible to achieve the desired weld quality. To ease the task of the welder, the internal machine control of the process can be enhanced. Such enhanced control of the process is the topic of this thesis.

1.1 Background and Motivation

Migatronic A/S is a company which develops and produces welding machines. The company was established in 1970, and during the first year four welding machines were produced. Today the company produces and manufactures around 25,000 welding machines each year. Many different types of welding machines are produced, and in general, high quality machines are produced which are suited for industry. In year 2000, Migatronic was developing a new inverter machine for GMAW welding (also called MIG/MAG welding). This machine was a major leap forward for the company with respect to welding machine technology, as basically, every part of the machine was based on new technology. For example, the machine included a completely new and faster inverter module. Also, a relative powerful computer system was included in the machine, which was supposed to control the welding process through the inverter module. Even though inverter technology and computers were used in older machines, the computation capability was limited in those machines, and the control algorithms were based on emulation of traditional transformer welding machines. To take advantage of the powerful computational capability and the new inverter module, better control algorithms were needed, but Migatronic did not know how to solve this problem.

Therefore, in September 2000 a cooperation between Migatronic A/S and Department of Control Engineering at Aalborg University was initiated. The cooperation was initiated by the start of an Industrial Ph.D. project sponsored by the Academy of Technical Science (ATV, Akademiet for tekniske videnskaber) in Denmark. The results of this Ph.D. project are presented in this thesis.

1.2 Objective and Focus

Initially, it was decided that the project should aim on developing new and improved control algorithms for the GMAW process, and during the project, the aim and the focus of the work were specified in greater detail. It was decided that the focus should be on

- Manual (hand-held) welding.
- Pulsed GMAW.
- The process excluding the weld pool.

Manual welding was preferred over automated (robotic) welding, because the market for manual welding machines is much bigger than the market for welding machines used for automated processes. Thus, Migatronic, as a machine manufacturer, is much more interested in manual welding. However, this does not mean that the ideas presented in this thesis can only be applied to the manual welding process, but rather, it means that certain control problems or specifications will be derived from that process. Also, it means that there is a limited number of sensors available for controlling the process. Typically, when using an advanced manual GMAW machine, either pulsed GMAW or short arc GMAW are used. However, to limit and specify the research area, it was chosen to focus on pulsed GMAW. Pulsed GMAW was chosen over short arc welding, as it was considered that, especially, the pulsed GMAW process could be improved. Control of the welding process can be split up into an inner loop in which the arc length and the transfer of metal to the weld pool are controlled, and an outer loop in which the weld pool is controlled. Normally, in manual welding the machine does only control the inner system, while the welder (human operator) controls the outer loop. In this work, focus is on the inner control loop, and thus, the weld pool is not considered in this thesis.

Based on the focus areas and the goal of improving welded joints, an overall objective for the Ph.D. project can be formulated. The objective is state in the

following.

Objective: *The objective is to optimize the control algorithms for the manual pulsed GMAW process, with the aim of enhancing the quality of welded joints.*

In Chapter 5 the objective is discussed in further detail, and moreover, a number of additional, but more specific, objectives are presented.

1.3 Overview of Previous and Related Work

Researching the GMAW process involves a large number of topics. These topics can be divided into control of the process, and investigation and modelling of the physics characterizing the process. Yet again, the control area can be divided into control of the weld pool, and control of the arc and the electrode. The former is concerned about the quality of the weld, which can be related to topics like weld pool geometry, such as penetration, and also, the heating and cooling of the workpiece plays a significant role for quality of the weld. A deep penetration gives a large area of the metal edges to be joined, and the heating and cooling rate are associated with the grain size in metal. Control of the arc and the electrode can also be related to the quality of the weld, but more indirectly. This area of research is concerned with control algorithms for electrode melting, drop detachment, and stabilization of the arc length. In the area of analysis and modelling of the GMAW process a variety of topics exists. Some topics are the electrode melting rate, the electrical arc, the forces acting on the drop, and the forces acting in the weld pool. Also, research concerning the use of different welding gases has been carried out. The research is an ongoing process, and in this thesis, yet another contribution is given.

Control of the total GMAW process can be separated into weld pool control and drop and arc control. Weld pool control can be considered as an outer control loop, while drop and arc control can be considered as the inner loop. This is illustrated in Figure 1.1. In manual welding the outer loop is handled by the welder, but for both automatic and manual welding the inner loop is handled by the machine. To achieve an overall high performance control system, and be able to produce welds of high quality, both loops must be handled by high performance controllers. In manual welding, the outer loop is the welder, and a high performance controller can be considered as a skilled welder. In the literature, in spite of the importance

of both loops, far most attention are devoted to the outer loop. Probably, this is because most people working with welding have a manufacturing background. In this thesis only the inner loop will be considered, and thus, control of the weld pool will not be considered. In the rest of the thesis the inner loop will be referred to as GMAW control, unless stated otherwise.

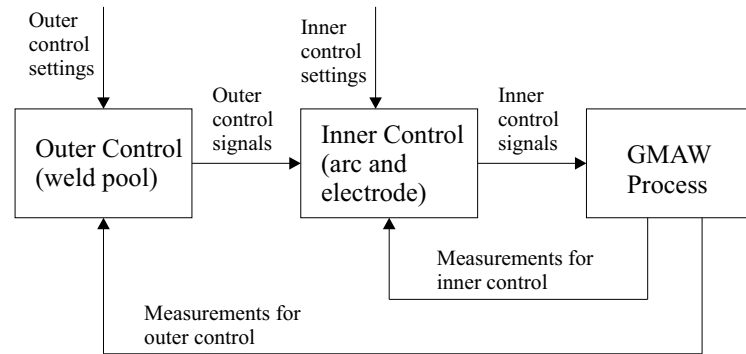


Figure 1.1: GMAW control can be divided into an inner control and an outer control in a cascade coupled system. The outer control addresses the weld pool, while the inner control addresses the electrode and the arc.

Typically, the GMAW process is divided into three modes of operation depending on the current. These modes are the short arc mode, the globular mode, and the spray mode, where pulsed GMAW can be considered as special case of the spray mode. A more detailed division of the modes of operation can be found in [28, Chapter 7]. For example, for even stronger currents, the process enters the streaming mode. In this thesis focus is on pulsed GMAW, and basically, two tasks should, or must, be handled in pulsed GMAW. These are arc length control (or alternatively, arc voltage control) and metal transfer control, where the former also applies to the ordinary spray mode GMAW. The most simple way to approach the arc length control problem is to apply a constant voltage potential to the process. Because of the relatively low voltage drop over the electrode compared to the arc voltage, disturbances in the distance from the welding pistol to the workpiece will not have a large effect on the arc length. In [8] and in several other works this is referred to as a "self-regulating" behavior. For high performance arc length control, the constant voltage potential approach is not sufficient, and instead, arc length feedback control is used. Such arc length control is presented in several works. In

[22] and in [45] the welding process is considered as a MIMO (multi-input multi-output) system, which is controlled using two decoupled PI-controllers for a fixed operating point. This approach is refined in [1] and [20] where linearization and decoupling are handled using a feedback approach. The same approach is used in [13], but sliding mode control is included in the control system. In [48] and in [10, Chapter 5] an adaptive control scheme is presented. In [53] and [54] a robust linear arc controller is proposed in which system uncertainty is taken into account. Furthermore, in [30] arc length control is performed using fuzzy logic control. The second task which must be handled in pulsed GMAW is metal transfer control. Advanced methods for metal transfer control can be found in [52] and in [56]. Weld pool control and other aspects of the GMAW process are mentioned in the survey paper [9], and also, in the book [10] in which a large number of references can be found.

The control algorithms presented in this thesis are based on knowledge of the process, that is, a model of the process. Important topics involve the melting rate, the arc, the drop, the forces acting on the drop, drop detachment, the electrical circuit of the process, and the shielding gas used.

In GMAW the electrode is melted at some melting rate, and new electrode are continuously supplied to the process. The melting rate of the process is modelled in [29], [41], [38], [37], and [57]. In [35] heat transfer in the drop is considered, which is important for a precise model of the melting rate. During welding an electrical arc exists between the anode and the cathode, and a model describing the arc voltage and the arc length is an important part of a total GMAW model. Typically, a simple model describing the arc voltage as a function of the arc length and the welding current is used, see for example [28, Chapter 6] or [10, Chapter 2]. The simple model is not exact, and in fact, deriving a precise model of the arc is very difficult. A description and investigation of the arc physics can be found in [28, Chapter 5], [46], [40], [6], and [44]. As stated above another important topic is the liquid drop of melted metal at the tip of the electrode. During welding the drop grows as melted metal is added to the drop, and at some point detaches from the electrode. The shape and the growth of the drop are considered in [50], [14], [41], [55], and [33]. In [32] and in [36], drop parameters and drop detachment are considered for pulsed GMAW. The drop is attached to the tip of electrode by the surface tension. It has been shown that such a system can be modelled by a mass-spring-damper system, see [2]. During welding a number of

forces acts on the drop, and among these forces the electromagnetic force is the most important. A model describing the electromagnetic force is derived in [5] and in [27], and also, the electromagnetic force is considered in [25] and in [34]. A overview and description of all significant forces can be found in [10, Chapter 2], and the forces in overhead welding are discussed in [47]. Another important aspect with respect to the drop is drop detachment. Drop detachment occurs when the surface tension is no longer able to keep the drop attached to the electrode. Basically, two models exists for predicting drop detachments. The first model is based on the surface tension and the axial forces acting on the drop, see [11], [26], and [16]. The second model is based on instability of a liquid cylinder, see [3], [4], and [28, Chapter 3 and 7]. After a drop is detached from the electrode it is transferred to the weld pool, and the velocity of the drop affects the weld pool and the final quality of the weld. The drop velocity is considered in [28, Chapter 7], [17], and [43]. The total metal transfer process, that is, drop growth and detachment, is considered in several of the papers already mentioned, but typically, the papers focus on one particular aspect. Another contribution to with respect to the total metal transfer process can be found in [51], in which metal transfer is evaluated using dimensional analysis. With respect to control and simulation it is important to have a complete model, which includes all the different aspects of the process. For control, at least, important topics like the the electrical circuit (current dynamic), the melting rate, and the arc must be considered. The total model is considered in [21], [11], [58], [23], [24], [42], and [59], where the instability with respect to the "self-regulating" mechanism is investigated in [58]. Moreover, a model describing the electrical circuit can be found in these papers. Also, with respect to the complete model data collection is important, see [15]. Other experiments and modelling topics are presented in [51].

1.4 Contributions

The thesis contains a number of contributions which are summarized below. Mainly, the contributions are in the area of GMAW control.

Dynamic Melting Rate Model : In general, for control of the GMAW process a steady state melting rate model is used. In pulsed GMAW the melting rate changes with the current pulses, but because of the melting rate dynamics, the melting rate goes through a transient phase for each change in current. This is not accounted for in the steady state model, and therefore, a dynamic melting rate model suitable

for control is derived. In spite of this, the model is not used for GMAW control in this thesis. Rather, it is considered as a stand-alone result, able to improve control algorithms relying on a melting rate model. Such improvement could be carried out in future work.

Nonlinear Arc Length Controller : An arc length controller is an important component in a control system for the GMAW process. In this thesis a novel nonlinear feedback linearization arc length controller is presented.

Metal Transfer Controller : In pulsed GMAW current pulses are used for providing drop detachments. Thus, a pulse generation algorithm is needed and this is referred to as a metal transfer controller. In this thesis a novel approach for metal transfer control is presented. The approach is based on obtaining a uniform drop size prior to detachment.

Arc Length Minimization : In most GMAW applications it is important to have a small arc length. Normally, a small arc length is obtained by adjusting the arc length reference off-line. In this thesis an on-line arc length minimization algorithm is proposed.

Electromagnetic Force Derivations : An important aspect of the GMAW process is the forces acting on the drop at the tip of the electrode. Normally, the electromagnetic force is the most significant of these forces. An expression for the electromagnetic force can easily be retrieved from the literature. However, it has been difficult to identify under which conditions the expression is valid, and moreover, it has not been possible to retrieve a detailed presentation of the calculations in the literature. Therefore, the expression for the electromagnetic force has been recalculated in this thesis, with the aim of providing a full and detailed presentation of the derivations.

1.5 Thesis Outline

Part I: Modelling the Gas Metal Arc Welding Process

Chapter 2: The Gas Metal Arc Welding Process

A short overview over the various manual electrical arc welding processes are given, which includes the stick welding process, the gas tungsten arc welding

(GTAW) process, and the gas metal arc welding (GMAW) process. The GMAW process is described in greatest detail, and also, an overview of the hardware architecture of a modern GMAW machine is given.

Chapter 3: The Gas Metal Arc Welding Model

A mathematical model describing the GMAW process is presented. A simulation program based on the GMAW model is developed, and the simulation program is used for illustrating the behavior of the GMAW process.

Chapter 4: Dynamic Melting Rate Model

The electrode is divided into three sections, which are the drop, the melting point, and the solid electrode. Furthermore, the solid electrode is divided into a number of small elements. Based on these divisions, a melting rate model is derived. This model is referred to as the *full dynamic melting rate model*. To reduce the number of calculations the model order is reduced by introducing an alternative partition of the solid electrode. This leads to an alternative melting rate model, denoted as the *reduced dynamic melting rate model*.

Part II: Controlling the Gas Metal Arc Welding Process

Chapter 5: Objectives and Control Topology

A number of specific objectives based on the objective stated in Section 1.2 is derived. These are direct objectives for the control system for the GMAW process, that is, the inner control system, see Section 1.3. Also, the structure, or topology, of the control system for the GMAW process is discussed.

Chapter 6: Nonlinear Arc Length Control

Based on the control structure presented in Chapter 5 a model suited for arc length control is derived. This model is a single input single output (SISO) system. A feedback linearization method is used for transforming the nonlinear system into a linear system, and a controller for the resulting linear system is developed based on a number of performance criteria. Also, robustness is addressed by considering system perturbations. Stability is proved using the Small Gain Theorem for a set of realistic perturbations. Moreover, a simulation program is developed and used for testing the nonlinear arc length controller.

Chapter 7: Model Based Metal Transfer Control

Metal transfer control is discussed, and various pulse shapes are presented. A novel metal transfer control approach based on obtaining a uniform drop size prior to pulse initiation is proposed, and two methods based on this principle is presented. A simulation program is developed and used for testing the methods.

Chapter 8: Arc Length Minimization

An algorithm for minimizing the arc length in GMAW is presented. The arc length is minimized by measuring the time between short circuits. For testing the algorithm a simulation program is developed.

Part III: Conclusions and Future Work

Chapter 9: Conclusions and Future Work

The conclusions for each chapter are summarized and discussed, and moreover, a number of suggestions for the future work on GMAW control related topics are presented.

Part IV: Appendices

Appendix A: Maxwell Stresses

This appendix is part of the derivation of the electromagnetic force presented in Chapter 3. Maxwell stresses on the drop are considered, and it is shown that the stresses results in an rotational force component, and moreover, a force component acting both inward and axial.

Appendix B: The Electromagnetic Force

Based on the result of Appendix A, the expression for the electromagnetic force is derived. Also, the appendix includes a list of the assumptions used.

Appendix C: The Pinch Effect

Based on the pinch effect theory, a criterium for drop detachment can be derived. The calculations can be found in this appendix.

1.6 Important Remarks

During the work on this Ph.D. project a real experimental welding facility suited for the task has not been available. Mainly, it has not been possible to acquire a high speed camera, which must be considered as an essential part of a practical welding test facility when working with the model based control algorithms presented in this thesis. Therefore, all experiments have been performed in software simulation programs. The simulation programs have been based on models which have been validated in literature. However, when using simulation only, one should be extra cautious or careful when drawing conclusions. In spite of the fact that all tests have been performed using simulation programs, the work presented in this thesis has a practical dimension as well. The practical dimension comes from the close cooperation with the engineers at Migatronik during the project, and also, during the work the author has been involved in the development of control algorithms for Migatronik's Flex 4000 welding machine. This is one of the most advanced GMAW machines at the market today.

With respect to the simulation programs developed, miscellaneous parameters and constants are needed to facilitate numerical calculations. For this purpose parameters and constants for stainless steel have been used. Moreover, a number of parameters have been retrieved from [20], and other parameters are based on Migatronik's Flex 4000 welding machine. All constants and parameters can be found in the Nomenclature.

Part I

Modelling the Gas Metal Arc Welding Process

The Gas Metal Arc Welding Process

2

In this chapter a number of methods for electrical arc welding are presented. The basic principles in each of the methods are explained, and in particular, the GMAW process is considered.

2.1 Electrical Arc Welding in General

Several types of electrical arc welding processes exist. For manual welding these are stick welding, Gas Tungsten Arc Welding (GTAW), and Gas Metal Arc Welding (GMAW). Stick welding is also referred to as Manual Metal Arc (MMA), or Shielded Metal Arc Welding (SMAW). GTAW is also called Tungsten Inert Gas (TIG), and GMAW is also called Metal Inert Gas (MIG) or Metal Active Gas (MAG), depending on the type of gas used. Depending on the welding task to be carried out, each of these processes has some advantages.

In stick welding, a consumable electrode, having a dry flux coating and a metal core, is used. In Figure 2.1 the stick welding process is illustrated. An electrical arc is established between the electrode and workpiece, and the energy, produced in this way, melts the workpiece, the solid metal core of the electrode, and the flux coating. As the flux coating burns away, gas is released which protects the welding process from the ambient air. Primarily, the gas generated from the burning flux coating is carbon dioxide, CO_2 , and in the hot arc the carbon dioxide molecules are ionized to carbon ions and oxygen ions. These ions, and especially the oxygen, react in the arc, and thus, the gas becomes an active component in the stick welding process. In addition to the gas, a layer of slag, covering and protecting the welded area, is produced from the burning flux coating. Different kinds of electrodes and flux coating exist, designed to meet different kinds of welding conditions and requirements. The electrode material, for example, must match the workpiece material used. Stick welding can be characterized as a simple process

that can be carried out using some inexpensive equipment, but compared to the other arc welding methods, the weld quality is normally not as good.

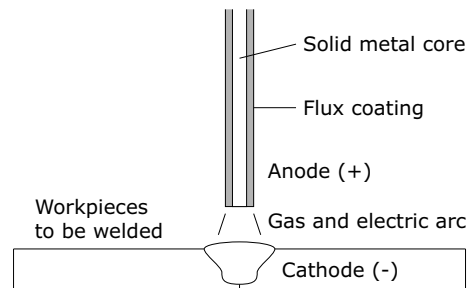


Figure 2.1: The stick welding process.

In GTAW an electrode consisting of pure tungsten, or some alloy that includes tungsten is used. Such electrode is used to give the electrode a high melting point, as the electrode in GTAW is not supposed to melt. Thus, in the GTAW process only the workpiece is melted. Similar to the stick welding process, a gas is used to protect the weld area from contamination, but unlike in stick welding, the gas is externally supplied to the process. Moreover, in GTAW only inert gases, normally argon, are used. Using GTAW, welds of high quality can be produced, but at the back side, GTAW is a slow process, and thus, it is not suited for many industrial applications requiring high welding speed. In Figure 2.2 the GTAW process is illustrated.

In GMAW a consumable electrode is used. The electrical arc is established between the consumable electrode, usually the anode, and the workpiece, then acting as the cathode. The energy produced in the arc melts the electrode, and causes drop growth and drop detachment from the tip of the electrode. The electrode, consumed in this way, is replaced by new electrode material, often referred to as the wire, as new electrode material is pushed forward by a wire feed system. Also, like in GTAW, the process is protected from the ambient air using a shielding gas. Typically, pure argon or a mixed gas of argon and CO_2 is used. In Figure 2.3 the part of the GMAW process involving the electrical arc is illustrated. In the following section, the GMAW process will be described in further detail.

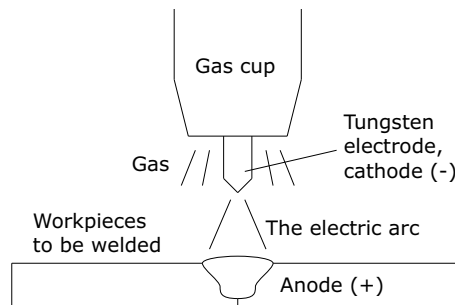


Figure 2.2: The gas tungsten arc welding (GTAW) process, also called the TIG welding process. The electrical arc exists between the electrode and workpieces. Shielding gas, emitted from the gas cup, protects the process from contamination.

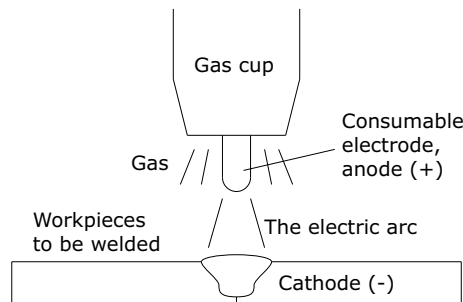


Figure 2.3: The gas metal arc welding (GMAW) process, also called the MIG/MAG welding process.

2.2 The GMAW process

In Figure 2.4 the overall welding process setup is illustrated. The specific setup described here corresponds to Migatron's Flex 4000 welding machine. As shown in the figure, the cathode wire is connected to the workpiece. The anode wire is fed from the power supply into the wire feed box, and further, through the cable connected to the welding pistol. In the pistol, the anode wire is connected to the electrode wire in the contact tube. Thus, current only flows in the electrode wire very close to the electrical arc. In addition to the current carrying anode wire and the electrode wire, the shielding gas is fed along the anode wire, and also, water is circulated for the purpose of cooling the welding pistol.

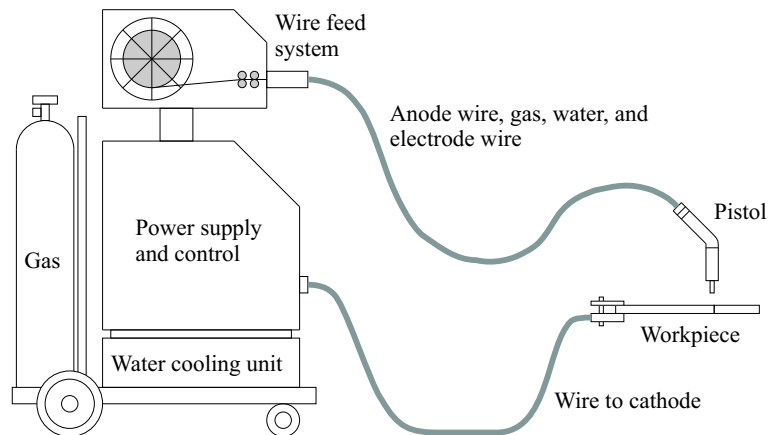


Figure 2.4: Illustration of Migatronix's Flex 4000 welding machine, the overall process setup.

The welding pistol can be operated either manually or automatically by a welding robot or some other automated setup. However, only manual welding (hand-held welding) is of concern in this thesis. Normally, in manual welding, the operator adjusts the welding machine to some desired settings, and then, the operator performs the actual weld. First, the electrical arc is ignited as the electrode touches the workpiece. After ignition has occurred, the task for the operator is to control the position of the welding pistol to achieve a good quality weld, while moving the electrode along the seam to be welded. This is a very difficult task which requires much skill to master.

In Figure 2.5, the GMAW process is illustrated again. However, in this figure, the whole electrical circuit is shown in greater detail. In Figure 2.5, the connection between the conducting anode wire and the electrode is shown, and as illustrated, the connection is established in the contact tube.

Former welding machines were based on transformer technology, such that, a high voltage and low current were transformed into a low voltage and a strong current. Such transformation is also performed in modern inverter based welding based, but a traditional transformer is not used. Instead, a hardware architecture as shown in Figure 2.6 is used. This particular architecture is used in Migatronix's Flex 4000 welding machine. First, a three phase power supply is connected to the machine from the available supply net. These phases are rectified to DC, and then,

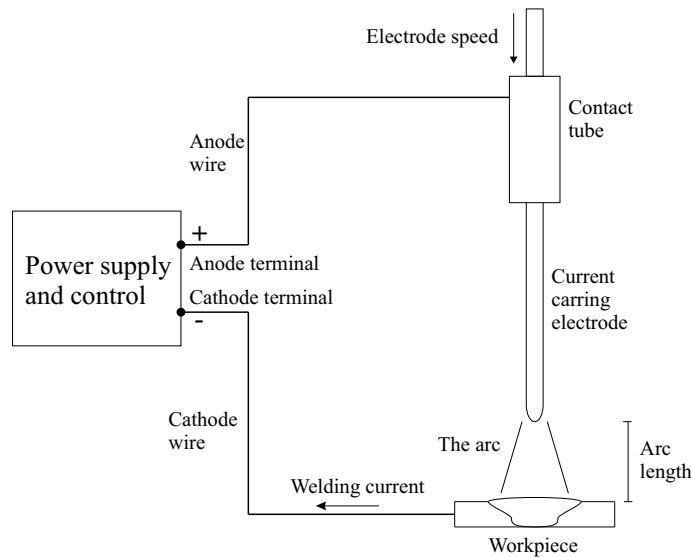


Figure 2.5: The electrical circuit of the GMAW process.

smoothed by a low pass filter. The DC voltage is modulated by the switch circuit, which is driven by the control software of the welding machine. The output of the switch circuit is either full positive voltage, zero voltage, or full negative voltage. Thus, the signal can be considered as an asynchronous signal. Afterwards, this signal is transformed by the transformer into a lower output voltage. Also, the transformer provides galvanic isolation between the supply net and the welding process. In the Flex 4000 welding machine, the voltage is reduced by a factor eight by the transformer. Next, the asynchronous output voltage from the transformer is rectified and smoothed by the output inductance and capacitor.

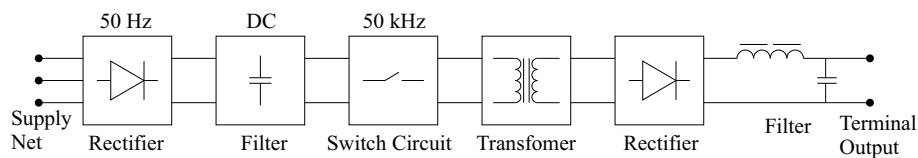


Figure 2.6: Power supply architecture of Migatron's Flex 4000 welding machine. Input is a three phase power supply (net power supply). Output is the terminal voltage.

GMAW can be divided into, at least, 3 modes of operation depending on the cur-

rent. These modes are the short arc mode, the globular mode, and the spray mode. In short arc mode, the tip of the electrode with the pendant drop is periodically short circuited with the workpiece, causing a sudden increase in current which detaches the drop. In spray mode the electrode is, ideally, never short circuited with the workpiece. A strong current causes melting and drop detachments from the electrode. The globular mode exists between the short arc mode and the spray mode, and normally produces a poor weld. Thus, in general, the globular mode must be avoided. In this thesis, focus is on pulsed GMAW. This type of welding falls within the spray mode, as drops in pulsed welding are detached by the strong current as in the spray mode. However, opposite the spray mode, the current is shifted between a low level and a high level. The advantage of using pulsed GMAW, when compared to the spray mode, is the lower heat input into the weld pool, and also, the pulses make it possible to control the drop detachment process.

The Gas Metal Arc Welding Model

3

In this chapter different parts of the GMAW process are modelled, and combining these parts a total model of the GMAW process is obtained. To illustrate the behavior of the model, a simulation program is developed and the model is simulated.

3.1 System Overview

The overall objective of the work documented in this thesis is to improve weld quality by developing an advanced control scheme for the GMAW process. One way to find such a control scheme is to develop a mathematical model describing the process, and then, based on that model, design a controller for the process. Such approach will be taken in this thesis, and therefore, in this chapter, a mathematical model describing the GMAW process will be derived. Moreover, the mathematical model derived in this chapter can be used for simulating the process. This is very important as all experiments and tests of controllers for the process will be carried out in a simulation program, and not in a real welding setup.

In Figure 3.1 the GMAW process is illustrated. The welding machines considered in this thesis are digital machines, and thus, control of the process is based on some sample time, T_s , for example, a sample time of 50 kHz as used in Migatron's Flex 4000 welding machine. Basically, at each sampling time, the control system of the welding machine calculates a PWM (Pulse Width Modulation) signal, u_{pwm} , to the inverter. This signal corresponds to some control voltage, U_c , from the inverter, see Figure 3.1. To protect the inverter and smoothen the current a small coil, described by some inductance constant L_m , is placed after the inverter. The machine terminals are placed after the coil, and here, the machine terminal voltage, U_t , can be measured.

Traditionally, in GMAW the machine terminals are connected to the process as shown in Figure 3.1, that is, the anode is connected to the consumable electrode, and the cathode is connected to the workpiece. Strong current flows through the wires connecting the terminals with the electrode and the workpiece, and because of the strong current, the voltage drop over the wires must be taken into account. As shown in Figure 3.1, the wires are modelled as a total wire inductance, L_w , and a total wire resistance, R_w .

The electrode moves through a cylindrical piece of metal connected to the anode terminal wire, and thereby, contact is established. The current flows through the electrode and through the electrical arc, thus, completing the circuit to the workpiece connected to the cathode terminal wire. In steady state, the downward electrode speed, v_e , equals the melting speed, v_m , of the electrode, and thus, in steady state, the arc length, l_a , is constant.

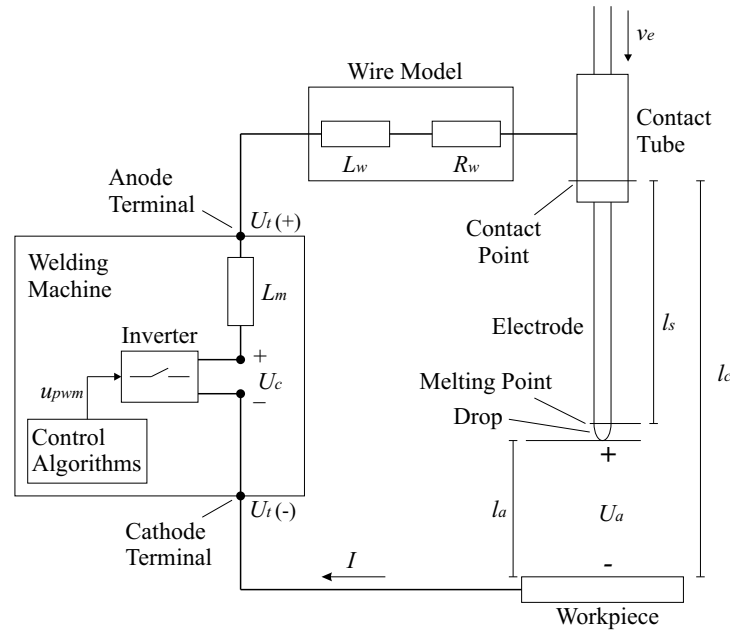


Figure 3.1: Illustration of the GMAW system.

In the following sections different aspects of the GMAW process will be modelled. In Section 3.2 the GMAW process will be modelled as an electrical circuit,

using elementary laws from the theory of electrical systems. A description of the electrical arc and a function describing the arc voltage are presented in Section 3.3. Afterwards, in Section 3.4, the dynamics of the pendant drop are considered. Next, in Section 3.5, drop detachment from the electrode is considered, and in Section 3.6 a melting rate model is presented. In Section 3.7, all the models for the different parts of the process are compiled into a set of differential equations describing the total GMAW process. Afterwards, in Section 3.8, a number of plots, illustrating the behavior of the process, are shown. The plots are obtained from a simulation program based on the total model presented in Section 3.7. The simulation program has been developed and implemented in Simulink.

3.2 The Electrical System

The GMAW process can be considered as an electrical circuit. Such circuit is shown in Figure 3.1. If the control voltage, U_c , is regarded as the input, the circuit consists of the machine inductance, L_m , the anode and cathode wires, the contact tube, the electrode, the electrical arc, and the workpiece. When a control voltage U_c is applied to the process a current, I , develops in the circuit, as shown in the figure.

The electrical wires from the welding machine to the process need to be considered and included in the model for several reasons. One reason is that the strong current used in welding gives a voltage drop over the wires, which might need to be considered when developing controllers for the process. Another reason is the current dynamics, which, basically, is determined by the wires. At least, this is true for modern inverter machines, for which, the machine inductance, L_m , is very small. In several works, see for example [21], [11], and [41], the wires are modelled as a resistance, R_w , and an inductance, L_w . In Figure 3.1, R_w and L_w are shown modelling both the anode wire and the cathode wire.

Within the contact tube, which is connected to the anode wire, the electrode touches the tube one or more places, and thus, establishes the contact to the electrode. Normally, a small voltage drop will be present from the contact tube to the electrode, which can be modelled by a resistance. Such resistance, denoted as the contact resistance, R_c , is for example included in the circuit model used in [41]. However, in this work the contact resistance will be excluded, as it is assumed to be small compared to other resistances in the circuit, and also, it can be considered

as being part of the wire resistance, R_w .

From the contact point to the beginning of the arc, the current flows through a piece of electrode. The length of this piece of electrode is very small compared to the length of the wires, but because the electrode is rather thin, then the resistance is high, and thus, the voltage drop over the electrode should be included in the model. The resistance of the electrode is denoted by R_e , and the length of the electrode, that is, the stick-out is denoted by l_s .

The most significant voltage drop in the circuit is the arc voltage, U_a . For weak currents, the control voltage, U_c , is almost equal to the arc voltage. However, for stronger currents the control voltage must be somewhat larger, because of the wire and electrode resistances, and also, because of the inductances for a changing current. Now, a model of the electrical circuit can be derived.

$$U_c = L_m \dot{I} + L_w \dot{I} + R_w I + R_e I + U_a \quad (3.1)$$

If the terminal voltage, U_t , is considered as the input to the process, the electrical circuit is by given by

$$U_t = L_w \dot{I} + R_w I + R_e I + U_a \quad (3.2)$$

The electrode resistance, R_e , can be modelled as the resistivity of the electrode times the total length of the electrode, including the drop. The length of the drop can be modelled as the average between the drop position, x_d , relative to the tip of the electrode, and the drop radius, r_d . Such model is used in [21].

$$R_e = \rho_r \left(l_s + \frac{1}{2}(x_d + r_d) \right) \quad (3.3)$$

However, both x_d and r_d are rather small compared to the stick-out, l_s , and therefore, these terms will not be included in the final model. So, we have

$$R_e = \rho_r l_s \quad (3.4)$$

As illustrated in Figure 3.1, the stick-out, l_s , is the distance from the contact point to the melting point of the electrode. The dynamics of l_s is given by the electrode

speed v_e and the melting speed v_m , and also, on the speed of the vertical velocity of the contact tube (also called contact tip). The contact tip to workpiece distance is given by l_c , and the contact tip to workpiece velocity is given by v_c . So, the stick-out dynamics is given by

$$\dot{l}_s = v_e - v_m \quad (3.5)$$

When designing controllers from the welding process it is the arc length, l_a , rather than the stick-out, which is of interest. From Figure 3.1 we have the following equation by ignoring the length of the drop.

$$l_c = l_s + l_a \quad (3.6)$$

Now, from this equation and from the stick-out dynamics, the arc length dynamics can be derived. We have

$$\dot{l}_a = v_m - v_e - v_c \quad (3.7)$$

3.3 The Electrical Arc

Normally, in GMAW, the consumable electrode is connected to the machine terminal plus, and the workpiece is connected to the machine terminal minus. Thus, when considering the electrical arc, the tip of the consumable electrode is the anode and the workpiece (the other electrode) is the cathode. During welding an arc exists between the anode and the cathode, where an arc can be described as a discharge of electricity between the electrodes, characterized by a high current density and a low voltage drop between the electrodes. In an arc electrons are released from the cathode and moves towards the anode, and at the same time, ions moves towards the cathode. In the following an arc is also referred to as an electrical arc.

The physics of the electrical arc with respect to welding have been investigated during the past half century. In [28] two chapters are devoted to the electrical arc, and here, mechanisms in different parts of the arc are described, and moreover a

number of physical characteristics of the arc are studied. These characteristics include the arc temperature, the arc pressure, the electrical field, the current density, vapor, gases, and the electrode materials used.

The purpose in this section is not to give a detailed description of every aspect regarding electrical arcs as in [28, Chapter 5 and 6], but rather, to identify and describe a model of the electrical arc, which can be used for simulating the process, and also, for developing controllers. When controlling the GMAW process, it is important to obtain a steady arc length, and also, it is important not to short circuit the electrodes, but on the other hand, it is important to have a small arc length (this will be discussed and explained in Chapter 5). It turns out that the arc voltage, U_a , among others factors, depends on the arc length, and therefore it is important to consider the arc, with the aim of identifying the relationship between the arc voltage, U_a , and the arc length, l_a .

The arc can be divided into three regions or layers [28, Chapter 5], and these are, the anode region, the arc column, and the cathode region. The length of the anode region and the cathode region (measured in the direction between anode and cathode) are very small, but both regions, and especially the cathode region, have a significant influence on the arc voltage drop.

The three regions and the associated voltage drops are shown in Figure 3.2. The figure shows how the voltage gradient differs in each region, though, it should be noted that the figure is only a sketch. For a real arc, the anode and cathode regions are much smaller, than shown in the figure, and the voltage gradients are much steeper. In the following, each region is considered.

3.3.1 The Cathode Region

The basic mechanisms for maintaining the discharge in the arc are located in the cathode region, and moreover, the most significant voltage drop of the total arc voltage exists in this region. For GTAW a typical voltage drop lies between 10 to 20 V [28, Chapter 6], which typically, are much larger than both the anode voltage drop and the voltage drop across the arc column. A similar voltage can be expected for GMAW. The cathode region can be divided into three zones [6], the cathode surface, the space charge zone, and the ionization zone. In [28, Chapter 5], the ionization zone is referred to as the contraction zone.

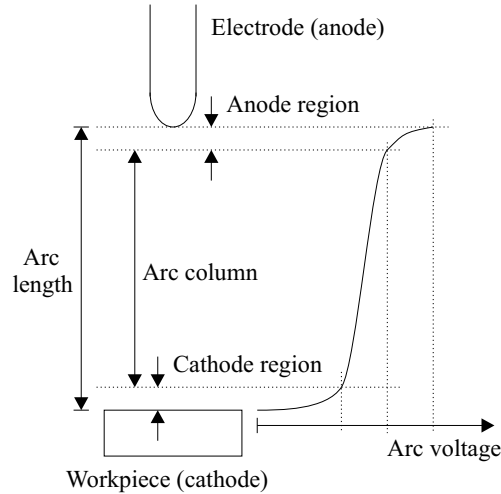


Figure 3.2: The arc is divided into three regions, that is, the anode region, the arc column, and the cathode region.

The three zones are shown in Figure 3.3. The cathode surface is charged by electrons. The negative charged electrons accelerates through the thin space charge zone of positive ions, which is a layer so thin, that statistically no collisions occur between the electrons and the other entities located in the zone. However, in the ionization zone collisions do occur. Some collisions occur between neutral entities (molecules, atoms) and electrons at high velocity. These collisions free new electrons and ionize the neutral entities. The free electrons accelerates in the electrical field towards the anode, while the ions normally accelerates towards the cathode. However, some large and slower moving ions moves against the space charge zone, and in equilibrium, replacing the ions lost in the space charge zone to the cathode surface. In Figure 3.3, the magnified region in the ionization zone illustrates a collision. An electron, e^- , collides with a neutral entity, a , which is ionized.

3.3.2 The Anode Region

Like the cathode region, the anode region can be divided into three zones, an anode surface zone, a space charge zone, and a contraction zone. The contraction zone is a transition layer between the space charge zone and the arc column.

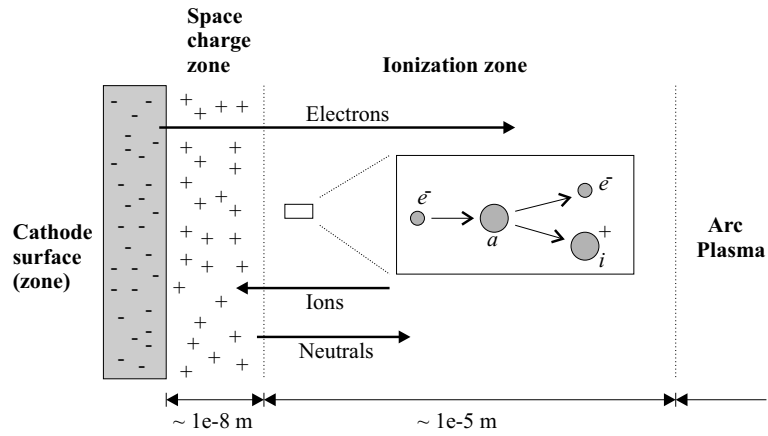


Figure 3.3: The cathode region is divided into three zones, that is, the cathode surface, the space charge zone, and the ionization zone. A small section is magnified in the ionization zone. e^- is an electron, a is a neutral entity, and i is a ion.

At the cathode surface current may be carried both by positive ions moving towards the cathode and electrons moving towards the anode, but this is not the case at the anode surface. At the anode surface current is carried entirely by electrons, because no ions are emitted from the anode.

Similar to the cathode region, a very thin space charge zone exists next to the surface of the electrode. Typically, for GTAW, the total anode voltage drop is in the range 1 to 10 V [28, Chapter 6], which is lower than the voltage drop across the cathode region. A similar voltage can be expected for GMAW. The reason for the anode voltage being smaller than the cathode voltage is the anode space charge zone. The anode space charge zone is smaller than the cathode space charge zone, which results in a smaller voltage drop. As stated before, no ions are emitted from the anode, but atoms are emitted from the anode material due to vaporization. These atoms are ionized by the electrons, and the magnitude of anode voltage drop depends on the ionization energy required, i.e. a high ionization energy increases the space charge zone, and thus, rises the anode voltage drop.

3.3.3 The Arc Column

The arc column is a plasma composed of neutral particles, such as atoms and molecules, and charged particles, such as electrons and ions. The current is carried by the free electrons and ions, and the column is characterized by electrical neutrality, i.e. in any small volume, an equal amount of positive charged particles and negative charged particles exist. The electrical neutral field produces a uniform electrical field in the arc column.

The electrical field gradient in the arc column is in the order of 10^3 V/m, and thus, much lower than the electrical field gradients in the cathode region and the anode region. This is illustrated in Figure 3.2. Also, the figure illustrates a constant electrical field by the straight line voltage characteristic.

3.3.4 A Mathematical Model of the Electrical Arc

By considering each of the three regions in the arc, a mathematical model describing the behavior of the arc can be derived. In [28, Chapter 6] and in [6], a model describing the cathode region is presented, and in [28, Chapter 6] models describing the anode region and the arc column are presented. However, these models depend on variables, such as the temperature at different locations in the arc, which are difficult to measure or estimate. Moreover, a complex and detailed model of the arc process is not necessary for controlling the GMAW process.

Instead of having a model describing the different mechanisms in the three regions, the arc can be modelled as some relationship between the total arc voltage, U_a , the welding current, I , and the arc length, l_a . Here, a linear model as shown below is used. Such model is used in numerous works for GMAW modelling and control, see for example, [11], [21], and [20].

$$U_a = U_0 + R_a I + E_a l_a \quad (3.8)$$

Considering the description given in the former three sections, the different terms in this equation can be explained. The constant U_0 could represent the two space charge zones, the latter two terms could represent the voltage drop over the arc column, as this region must depend both on the current and the length. For strong currents, more collisions occur in the arc column than for low currents, and more

collisions give a larger voltage drop. Such dependence of the current can be modelled by a resistance, R_a . The dependence of the arc length can also be explained, as the longer the arc is, the longer do the electrons and ions have to travel. This affects the arc voltage, as more collisions occur for a long arc length than for a small arc length, and more collisions give an increased voltage drop. Clearly, the model presented in equation 3.8 is not accurate, as the arc is very complex. For example, in [28, Chapter 6] it can be seen, that the arc voltage is rather a nonlinear function with respect to the welding current and the arc length.

3.4 Drop Dynamics

In GMAW, the electrode is melted by Ohmic heating and anode heating. Ohmic heating is the energy developed by the current and the ohmic resistance in the electrode, and anode heating is the energy from the arc which melts the anode. So, during welding, liquid metal is continuously added to the drop at the tip of the electrode, and at some point the pendant metal drop is detached from the electrode. Some metal is left at the tip of the electrode, and a new drop starts forming. Basically, drop detachment occurs when the surface tension, which keeps the drop attached to the electrode, is exceeded by other forces affecting the drop, or otherwise, can not stop a downward movement of the drop. Thus, to model the GMAW process, the forces affecting the drop, and also, the drop dynamics must be taken into account.

In [2], the pendant drop at the tip of the electrode was described by a mass-spring-damper system, and normally, this model will be encountered in the literature. However, in [26], the mass-spring-damper system was refined, as the shape of the drop was taken into account. No matter which model is used for describing the system, a high degree of inaccuracy will exist in the model due to the almost chaotic behavior of the pendant drop system. Therefore, the model developed in [26], being somewhat more complex, will not be used in this thesis.

The mass-spring-damper model describing the pendant drop system is stated below, and moreover, illustrated in Figure 3.4. m_d is the mass of the drop, which varies in time, F_T is the total force affecting the drop, x_d is the drop position, b_d is the damper constant, and k_d is the spring constant.

$$m_d \ddot{x}_d = F_T - b_d \dot{x}_d - k_d x_d \quad (3.9)$$

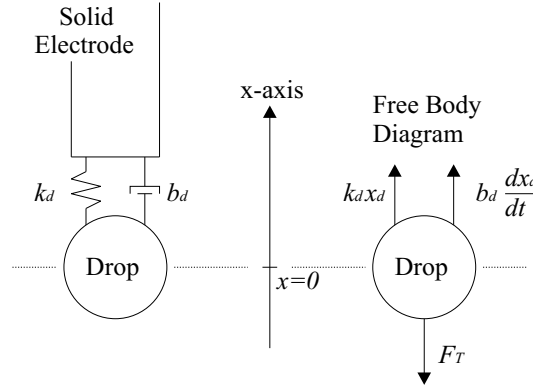


Figure 3.4: A) The pendant drop modelled as a mass-spring-damper system. B) A free body diagram of the mass-spring-damper system.

The change of mass of the drop depends on the melting rate. This can be expressed as given below. M_R is the melting rate, and ρ_e is the density of the liquid electrode material.

$$\dot{m}_d = M_R \rho_e \quad (3.10)$$

The forces that affect the drop, and which are included in F_T , are a force due to gravity, a force caused by electromagnetic induction, a force caused by aerodynamic drag, and a momentum force accounting for the change of mass in the drop, and also, accounting for the speed of the material added to the drop. Other forces also affect the drop but the four forces, suggested here, are considered as the most significant forces in the system. Also, this set of forces is used in [21] and [11]. So, the total force F_T can be described by the following expression.

$$F_T = F_g + F_{em} + F_d + F_m \quad (3.11)$$

F_g is the gravitational force, F_{em} is the electromagnetic force, F_d is the drag force, and F_m is the momentum force. In the following sections an expression for each force will be derived. In general, it is assumed that the electrode is pointing directly downwards (90° to the water surface) towards a workpiece lying flat in a horizontal position.

3.4.1 Gravity

The drop has a mass, and thus, is affected by gravity. The gravitational force F_g is given by equation (3.12).

$$F_g = m_d g \quad (3.12)$$

3.4.2 Electromagnetic Force

The electromagnetic force acting on the drop is a result of current flow within the electrode, including the drop. The current flow within the electrode generates a magnetic field circling the current path. The current path does not necessarily follow a straight line parallel to the electrode, but rather, the current path tends to diverge or converge in the drop. If the current flow either diverges or converges, an axial force acting on the drop will be generated by the current and the induced magnetic field. This axial electromagnetic force is also referred to as the Lorentz force. In Figure 3.5 the electromagnetic force acting on a small element in the drop is shown. The figure shows the electromagnetic force for a diverging and a converging current path.

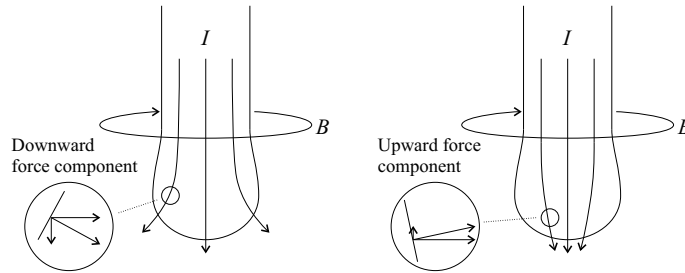


Figure 3.5: The electromagnetic force acting on a small element in the drop, respectively, for a diverging and a converging current path.

The total electromagnetic force acting on the drop can be calculated by integrating the electromagnetic force acting on all elements within the drop. The electromagnetic force \mathbf{f}_{em} for each small element can be expressed as below. Notice, that in this section, and also, in Appendix A and in Appendix B, boldface letters represent vectors, but in general, throughout the thesis, the boldface notation will not be used.

$$\mathbf{f}_{em} = \mathbf{J} \times \mathbf{B} \quad (3.13)$$

\mathbf{J} is the current density, and \mathbf{B} is the magnetic field. In [28, Chapter 3], the electromagnetic force \mathbf{f}_{em} is referred to as a Maxwell stress, and moreover, in [28, Chapter 3], it is rewritten as shown below.

$$\mathbf{f}_{em} = \mathbf{J} \times \mathbf{B} = \frac{1}{\mu} (\nabla \times \mathbf{B}) \times \mathbf{B} \quad \Rightarrow \quad (3.14)$$

$$\mathbf{f}_{em} = -\frac{1}{2\mu} \nabla(B^2) + \frac{1}{\mu} (\mathbf{B} \cdot \nabla) \mathbf{B} \quad (3.15)$$

One of Maxwell's equations and some technical calculations are used for obtaining this result. Equation (3.15) contains two terms. If the current path follows a straight line parallel to the electrode, the first term gives rise to a radial inward acting force, acting on elements within the drop. However, if the current path either diverges or converges, the electromagnetic force will either have a downward or an upward component (as shown in Figure 3.5). The second term in equation (3.15) expresses the rotational force, also acting within the drop. In Appendix A, the force contributions from, respectively, the first and the second term are calculated for a small element within the drop. From the results of these calculations one can see that the second term is purely rotational, both for a parallel current path and for a diverging or converging current path, while the first term gives rise to an axial force for a diverging or converging current path.

For a rigid and symmetrical body, every rotational force acting on a small element is cancelled out by a force acting on the opposite element in the rigid and fixed body. Thus, this results in a net force equal to zero. However, the liquid metal drop is not rigid, and the forces do not cancel out, but rather, the drop starts rotating. In spite of that, the contribution from the rotational part of the electromagnetic force is, in general, neglected in the literature when deriving the total electromagnetic force acting on the drop. The reason why the rotational part can be neglected is the relative slow time constant for the rotation in comparison with the rate of drop detachments, and moreover, as shown in [27], that the magnetic diffusion process is much faster than the fluid convection within the drop.

Now, by neglecting the second term in equation (3.15), the total electromagnetic

force acting on the drop can be found by integrating all contributions from the first term.

$$\mathbf{F}_{em} = \int_{V_d} \mathbf{f}_{em} dV = - \int_{S_d} \frac{B^2}{2\mu} \mathbf{n} dS \quad (3.16)$$

In [5], a similar expression for the total electromagnetic acting on the drop was used for deriving a number of, more suitable, expressions for the total electromagnetic force. The expressions for the total electromagnetic force were calculated for spherical drops with a radius of, respectively, greater than the electrode radius, equal to the electrode radius, and less than the electrode radius. Moreover, in [27], the electromagnetic force was calculated for drop shapes observed from experimental images. Drops were modelled as truncated ellipsoids, but having a polynomial description of the neck of the drop.

Normally, in the literature, one will find only one formula expressing the electromagnetic force acting on the drop. This is the formula derived in [5] for a drop radius greater than the radius of the electrode. That formula will also be adopted as the sole expression, used in this thesis, for the electromagnetic force. The reason for adopting this expression as well, is because of the somewhat unpredictable shape of the drop in practical welding. For example, often the arc does not necessarily follow a straight line directly to the workpiece, but rather, tends to be curved, and thereby, affecting the direction and size of electromagnetic forces acting within the drop, and causing the drop to deform. In general, the shape of the drop is a result of the surface tension and all other forces or stresses acting within the drop. So, it is difficult to model the shape of the drop, and also, it is difficult to model the current path within the drop. Therefore, with respect to the shape of the drop, a reasonable compromise seems to be a spherical shape. Moreover, drops in pulsed GMAW tends to have a diameter equal to or slightly larger than the electrode, and therefore, using an expression based on a drop radius larger or equal to the radius of the electrode also seems to be reasonable.

The derivation of the final expression is rather technical, and in [5] some parts are left out. To provide a better understanding of the expression it is derived in Appendix B. From [5] and Appendix B we have the following expression for the electromagnetic force acting on the drop.

$$F_{em} = \frac{\mu_0 I^2}{4\pi} \left[\ln \left(\frac{r_d \sin \theta}{r_e} \right) - \frac{1}{4} - \frac{1}{1 - \cos \theta} + \frac{2}{(1 - \cos \theta)^2} \ln \left(\frac{2}{1 + \cos \theta} \right) \right] \quad (3.17)$$

The parameters are the current, I , the electrode radius, r_e , the drop radius, r_d , and moreover the angle θ , which is used for describing the size of the conducting zone, see Figure 3.6.

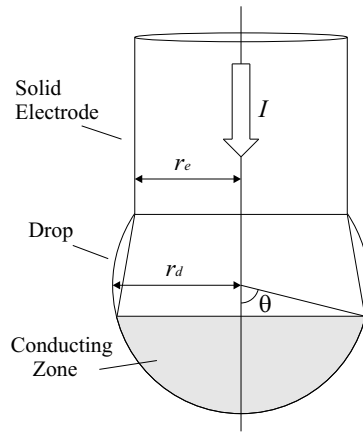


Figure 3.6: Current flows through the conduction zone, but not through the rest of the drop surface. The conduction zone is described by the angle θ .

In Figure 3.7, equation (3.17) is plotted as a function the current, and for three different θ . For all plots the electrode radius, r_e , is equal to 0.005 m, and the drop radius, r_d , is equal to 0.006 m. As it can be seen, the magnitude of the electromagnetic force increases for increasing current. In fact, it increases with the square of the current. A conducting zone described by either θ equal to 90° or θ equal to 67.5° , results in a positive force, while a conducting zone given by 45° results in a negative force. So, a θ equal to 90° or 67.5° corresponds to a diverging current, and a θ equal to 45° corresponds to a converging current. Moreover, in Figure 3.8 it can be seen how the electromagnetic force depends on the drop radius, r_d .

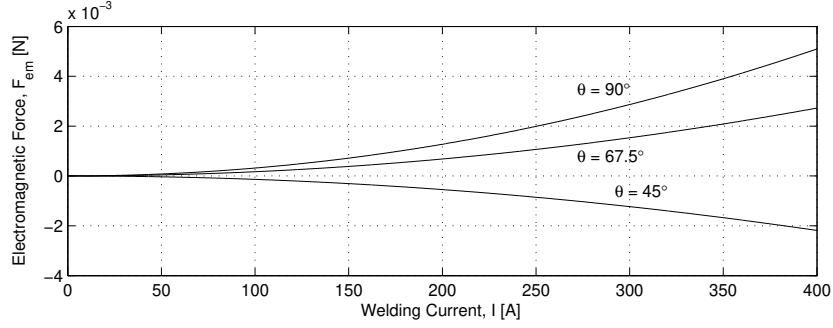


Figure 3.7: The electromagnetic force plotted for three different θ . The angle θ characterizes the area of the conducting zone.

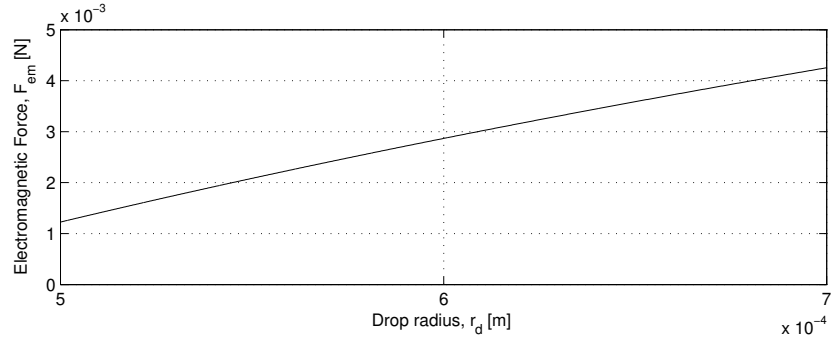


Figure 3.8: The electromagnetic force as a function of the drop radius. θ is set to 90° , and the current is set to 300 A.

3.4.3 Aerodynamic Drag

As explained in Chapter 2, a shielding gas envelops the arc region and protects the arc and the workpiece from contamination. In GMAW, the shielding gas is provided from a gas cup covering the electrode. The shielding gas, having a velocity v_p , passes around the drop and affects the drop with a force caused by aerodynamic drag. In GMAW, the contribution from aerodynamic drag on the drop can be approximated by a force acting on a spherical object immersed in a fluid stream [2].

$$F_d = \frac{1}{2} C_d A_d \rho_p v_p^2 \quad (3.18)$$

C_d characterizes the shape of the drop, in this case a sphere, A_d is the area of the drop seen from above, and not covered by the electrode cross area, ρ_p is the density of the plasma (ionized shielding gas), and v_p is the velocity of the plasma.

3.4.4 Momentum Force

In GMAW, the mass of the drop changes continuously with the metal melted from solid part of electrode. To account for this change of mass and the speed of the material added to the drop, a force F_m is introduced. This force is called the momentum force. In [2] and [21] such a force is also used to account for the change in mass. The force can be derived by considering the change in momentum of the pendant drop system. In Figure 3.9 the system is shown.

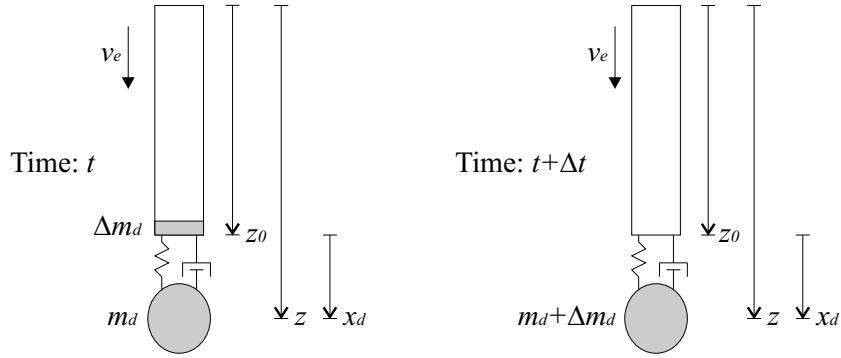


Figure 3.9: Change in momentum.

From Figure 3.9 we have that

$$z = z_0 + x_d \quad (3.19)$$

$$\dot{z} = \dot{z}_0 + \dot{x}_d \quad (3.20)$$

Figure 3.9 shows that the electrode moves towards the drop with a velocity v_e . This means that every small piece of solid electrode moves with this velocity. This includes Δm_d at time t . In steady state the melting speed equals the electrode speed v_e , and thus, the variable z_0 is a constant, and \dot{z}_0 will be equal to zero. For deriving an expression for F_m , it is assumed that z_0 is a constant.

Now, using Figure 3.9, the momentum of the shaded material at time t and the momentum at time $t + \Delta t$ can be derived, that is, $p(t)$ and $p(t + \Delta t)$.

$$p(t) = \Delta m_d v_e + m_d \dot{x}_d, \text{ because } \dot{z} = \dot{x}_d \quad (3.21)$$

At time $t + \Delta t$, the velocity of the drop, \dot{x}_d , can be expressed as $\dot{x}_d(t + \Delta t) = \dot{x}_d + \Delta \dot{x}_d$. So, we have

$$\begin{aligned} p(t + \Delta t) &= (m_d + \Delta m_d)(\dot{x}_d + \Delta \dot{x}_d) \\ &= m_d \dot{x}_d + m_d \Delta \dot{x}_d + \Delta m_d \dot{x}_d + \Delta m_d \Delta \dot{x}_d \\ &\approx m_d \dot{x}_d + m_d \Delta \dot{x}_d + \Delta m_d \dot{x}_d \end{aligned} \quad (3.22)$$

The change in momentum is given by

$$p(t + \Delta t) - p(t) = m_d \Delta \dot{x}_d + \Delta m_d \dot{x}_d - \Delta m_d v_e \quad (3.23)$$

By dividing by Δt and taking the limit, an expression for the derivative of the momentum is obtained. Also, the derivative of the momentum dp/dt equals the sum of all external forces, F_{ext} . The external forces are the gravitational force, F_g , the electromagnetic force, F_{em} , and the aerodynamic drag force, F_d .

$$\begin{aligned} \frac{p(t + \Delta t) - p(t)}{\Delta t} &= m_d \frac{\Delta \dot{x}_d}{\Delta t} + \dot{x}_d \frac{\Delta m_d}{\Delta t} - v_e \frac{\Delta m_d}{\Delta t} \Rightarrow \\ \frac{dp}{dt} &= m_d \ddot{x}_d + \dot{x}_d \dot{m}_d - v_e \dot{m}_d = F_{ext} \end{aligned} \quad (3.24)$$

Now, it is assumed that the speed of the electrode is much faster than the speed of the drop, such that $v_e \gg \dot{x}_d$, even though, this might not always be true. By introducing this assumption the same expression for F_m as used in [2] and [21] is obtained. So, the momentum force, F_m , is given by

$$F_m = v_e \dot{m}_d \quad (3.25)$$

3.5 Drop Detachment

During the welding process liquid metal is continuously added to the drop at the tip of the electrode, and at some point, the drop is detached from the electrode. Detachment happens when the surface tension of the drop is no longer able to support the drop attached to the electrode. Typically, drop detachment has been modelled by two different models: The static force balance model (SFBM) [2], and a model based on the pinch instability theory (PIT) [28, Chapter 3]. The SFBM predicts drop detachment by comparing the surface tension of the drop with the external forces exerted on the drop. Thus, in the SFBM the dynamics of the drop is not taken into account when predicting the occurrence of drop detachment. However, in [16], dynamics are taken into account by including the inertia force in the SFBM. This results in a dynamic model, which in [16] is called the dynamic force balance model (DFBM). Both the SFBM and the DFBM predicts drop detachment by evaluating forces affecting the drop against the surface tension supporting the drop. However, the pinch instability theory (PIT) results in a different detachment criterion. Based on the pinch instability theory, a detachment criterion can be derived that does not rely on balance of axial forces, but rather relies on radial forces.

The surface tension force, F_s , is in, for example, [11] expressed as the surface tension force in the zone in which the neck of the drop starts to form. The neck starts to form close to the electrode, and thus, the radius of the electrode, r_e , is used to derive the expression for the surface tension force. γ is the surface tension coefficient of the electrode material.

$$F_s = 2\pi r_e \gamma \quad (3.26)$$

The SFBM does not include any dynamics of the pendant drop. Hence, detachment occurs if the maximal surface tension force, F_s , is exceeded by the total force, F_T , affecting the drop.

$$\text{SFBM, detachment if } F_T > F_s \quad (3.27)$$

In the DFBM, described in [16], the inertia force is included in the detachment criterion. So, the following criterion is obtained.

$$\text{DFBM, detachment if } F_T + m_d \ddot{x}_d > F_s \quad (3.28)$$

In [28, Chapter 3], the detachment criterion, based on the pinch instability theory, is derived. Detachment occurs if a critical drop radius, r_{dc} , is exceeded. In Appendix C the derivations resulting in the pinch instability criterion are shown.

$$\text{PIT, detachment if } r_d > r_{dc} \quad (3.29)$$

where

$$r_{dc} = \frac{\pi(r_d + r_e)}{1.25 \left(\frac{x_d + r_d}{r_d} \right) \left(1 + \frac{\mu_0 I^2}{2\pi^2 \gamma(r_d + r_e)} \right)^{\frac{1}{2}}}, \quad r_d = \left(\frac{3m_d}{4\pi\rho_e} \right)^{\frac{1}{3}} \quad (3.30)$$

In GMAW, the current interacts with the induced magnetic field, and thus, generating forces acting inward and radially within the drop, and hence, squeezes the drop from the electrode. It is this phenomenon, called the pinch effect, that is modelled in equation (3.30). The SFBM and the DFBM do not take the pinch effect into account, and therefore, at strong currents, where the pinch effect is especially strong, the PIT model is the best drop detachment model. However, at low currents both the SFBM and the DFBM provides better estimates of drop detachment, see SFBM versus PIT in [24]. Therefore, the best solution, using the models described above, is some combination between the models. However, when considering pulsed welding, the PIT model could be used as the sole drop detachment estimator, as drops tend to detach at the strong current pulses.

At detachment, some part of the liquid metal forms an isolated drop which traverses towards the weld pool, while the rest of the liquid metal is left on the tip of the electrode. In [11], an equation is presented for the volume of the liquid material left on the electrode.

$$\text{After detachment, } V_d = \frac{m_d}{2\rho_r} \left(\frac{1}{1 + e^{-\kappa \dot{x}}} + 1 \right), \quad \kappa = 100 \text{ s/m} \quad (3.31)$$

3.6 Melting Rate

Current flows through the electrode and the arc. At the tip of the electrode, assumed to be the anode, the surface is bombarded by electrons travelling through an electrical field having a very steep gradient. The electrical field accelerates the electrons and the high energy of the accelerated electrons is absorbed into the anode, causing the anode to melt. Moreover, the electrode is heated by the current flowing through it. This heat, called Ohmic heating, is caused by the ohmic resistance of the electrode.

In [29], an extensive study of both the anode and the cathode melting rate is presented. However, only the anode melting rate is considered in this thesis. In [29], it is found that two heat sources affect the anode melting rate. These are the anode heating, H_a , and the Ohmic heating. The anode heating is expressed by the following equation.

$$H_a = c_{an}(V_{an} + \phi_w)I \quad (3.32)$$

V_{an} is the anode voltage drop (not to be confused with the arc voltage), ϕ_w is the anode thermionic work function, I is the welding current, and c_{an} is a constant. The first term, $c_{an}V_{an}I$, expresses the kinetic energy of electrons bombarding the anode. The kinetic energy is developed in the electrical field close to the anode. The second term, $c_{an}\phi_w I$, expresses the energy of condensation. This is the energy released when electrons are absorbed into the lattice of the electrode material.

In [29], an expression for the melting rate caused by anode heating is presented. Also, the expression is stated below. c_1 is a constant.

$$M_{R,a} = c_1 I \quad (3.33)$$

If the stick-out, l_s , is different from zero, which is the case in GMAW, energy loss due to electrical resistance heats the electrode, and thus, contributes to the melting rate. In [29], this component is expressed as below. c_2 is a constant.

$$M_{R,j} = c_2 l_s I^2 \quad (3.34)$$

Equation (3.33) and equation (3.34) describe the steady state melting rate for, respectively, the anode heating and the Ohmic heating. By adding the two equations, an expression for the total steady state melting rate, M_R , is obtained.

$$M_R = M_{R,a} + M_{R,j} = c_1 I + c_2 l_s I^2 \quad (3.35)$$

The constant c_2 can be calculated using the parameters describing the electrode, basically, the electrode resistivity and the electrode diameter. The other constant, c_1 , also depends on the electrode parameters. Here, the components of the electrode material and the anode diameter play a significant role. Equation (3.35) can also be expressed as a melting speed v_m , where k_1 and k_2 are melting speed constants.

$$v_m = k_1 I + k_2 l_s I^2 \quad (3.36)$$

It is interesting to notice that the melting rate does not depend on the type of gas used, even though, the arc temperature depends on the gas used. This is due to the fact that arc radiation is insignificant as a heat source affecting the electrode. This fact is reported in [29] and in [31]. Instead, the type of gas used is important when it comes to shielding the arc and the weld pool against the ambient atmosphere, and moreover, the shielding gas is important for arc ignition and arc stability [31].

3.7 The GMAW model

In the former sections, equations describing different parts of the GMAW process were presented. Using these equations, a total model describing the GMAW process is derived in this section. This model is similar to the model found in [21]. The total model presented in this section will later be used for simulating the process, and also, for developing algorithms for control of the GMAW process.

First, let us define a number of inputs, outputs, and states for the model. These are given below.

States:

- $x_1 = I$: welding current.
- $x_2 = l_a$: arc length.

- $x_3 = x_d$: drop displacement.
- $x_4 = v_d$: droplet velocity.
- $x_5 = m_d$: drop mass.
- $x_6 = l_c$: contact tip to workpiece distance.

Outputs:

- $y_1 = I$: welding current.
- $y_2 = l_a$: arc length.

Inputs:

- $u_1 = U_c$: control voltage.
- $u_2 = v_e$: electrode speed.
- $u_3 = v_c$: contact tip to workpiece velocity.

Now, the welding process can be described by the following nonlinear system.

$$\dot{x} = f(x) + g(x)u \quad (3.37)$$

$$y = h(x) \quad (3.38)$$

$$x = m(x) , \text{ if } L(x, u) > 0 \quad (3.39)$$

Equation (3.37) describes the system dynamics, equation (3.38) describes the outputs of the system, and equation (3.39) contains a reset condition, $L(x, u)$. Also, (3.39) describes how to reset the states. We have

$$\dot{x}_1 = \frac{1}{L_m + L_w} (u_1 - (R_w + R_a + \rho_r(x_6 - x_2))x_1 - U_0 - E_a x_2) \quad (3.40)$$

$$\dot{x}_2 = v_m - u_2 - u_3 \quad (3.41)$$

$$\dot{x}_3 = x_4 \quad (3.42)$$

$$\dot{x}_4 = \frac{1}{x_5} (-k_d x_3 - b_d x_4 + F_1 + M_R \rho_e u_2) \quad (3.43)$$

$$\dot{x}_5 = M_R \rho_e \quad (3.44)$$

$$\dot{x}_6 = u_3 \quad (3.45)$$

$$y_1 = x_1 \quad (3.46)$$

$$y_2 = x_2 \quad (3.47)$$

The current dynamics, stated in equation (3.40), are derived from (3.1), (3.4) and (3.8). The dynamics describing the arc length, that is equation (3.41), is derived from (3.7). The derivative of the drop position, x_3 , is the drop velocity, x_4 . This is stated in equation (3.42). The dynamics of the drop velocity is stated in equation (3.43), which is derived from (3.9) and (3.11). Equation (3.44), describing the drop mass dynamics, is given by (3.10). The derivative of the contact tip to workpiece distance, x_6 , equals the contact tip to workpiece velocity. This is stated in (3.45).

Functions used in the equations above are stated below. Notice, that the melting rate, M_R [m³/s], has been expressed as a melting speed, v_m [m/s].

$$F_1 = F_{em} + F_g + F_d \quad (3.48)$$

$$F_{em} = \frac{\mu_0 x_1^2}{4\pi} \left[\ln \left(\frac{r_d \sin \theta}{r_e} \right) - \frac{1}{4} - \frac{1}{1 - \cos \theta} + \frac{2}{(1 - \cos \theta)^2} \ln \left(\frac{2}{1 + \cos \theta} \right) \right] \quad (3.49)$$

$$F_g = g x_5, \quad g = 9.82 \text{ m/s}^2 \quad (3.50)$$

$$F_d = \frac{1}{2} C_d A_d \rho_p v_p^2 \quad (3.51)$$

$$M_R = c_1 x_1 + c_2 \rho_r x_1^2 (u_3 - x_2) \quad (3.52)$$

$$v_m = k_1 x_1 + k_2 \rho_r x_1^2 (u_3 - x_2) \quad (3.53)$$

$$r_d = \left(\frac{3x_5}{4\pi\rho_e} \right)^{\frac{1}{3}} \quad (3.54)$$

The reset values are shown below. This correspond to $m(x)$ in equation (3.39). The value for x_5 is obtained from (3.31). The reset condition $L(x, u)$ is given by either SFBM, DFBM, PIT, or a combination thereof, see Section 3.5.

Reset conditions:

IF: detachment criterion fulfilled

THEN:

$$x_1 := x_1 \quad (3.55)$$

$$x_2 := x_2 \quad (3.56)$$

$$x_3 := 0 \quad (3.57)$$

$$x_4 := 0 \quad (3.58)$$

$$x_5 := \frac{x_5}{2} \left(\frac{1}{1 + e^{-\kappa x_4}} + 1 \right), \quad \kappa = 100 \text{ s/m} \quad (3.59)$$

$$x_6 := x_6 \quad (3.60)$$

3.8 Simulations

A simulation program for simulating the GMAW process has been developed. The program has been developed in Simulink, and it is based on the model of the GMAW process described in the former section. To illustrate the behavior of the simulation program, an experiment has been performed on the simulation program, and for this experiment, series of data have been collected. The experiment and the data are presented in this section. The simulation program which has been developed in Simulink is illustrated in Figure 3.10.

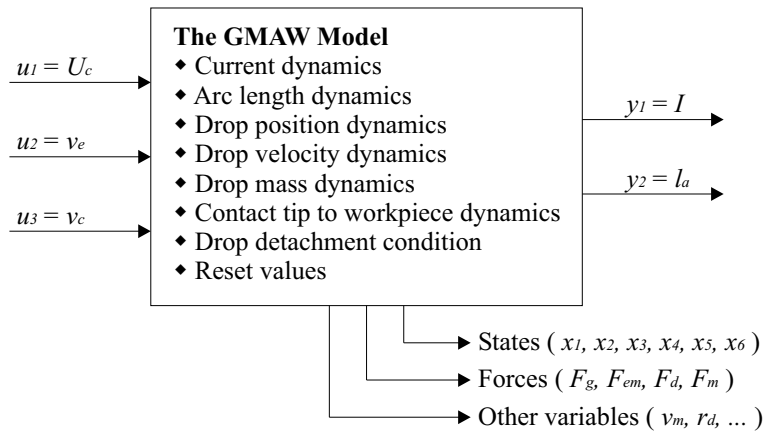


Figure 3.10: Illustration of the simulation program.

In the experiment, an input control voltage, u_1 of 21 V, plus pulses of additional 7 V, starting a time $t = 0.1$ s, are applied to the simulated process. The pulses are used to provide drop detachment. Moreover, an additional 300 Hz signal with an amplitude of 1 V is added to the input control signal to simulate voltage ripple from the welding machine. The wire feed speed, u_2 , which is the second input, is set to 10 m/min. To simulate disturbances in the contact tip workpiece distance, l_c , bandlimited Gaussian noise is added to the mean distance set to 0.015 m. The

bandlimited Gaussian noise has a mean equal to zero, a variance equal to 0.002^2 , and moreover, the Gaussian noise is bandlimited at 20 Hz, but ensuring that the energy in the noise signal is maintained. The derivative of the generated l_c is used as the third input, u_3 . The three inputs are illustrated in Figure 3.11. For simulating drop detachments, only the PIT model is used. The total length of the simulation is set to 0.5 s, and moreover, the value of all constants and parameters used in the model can be found in the Nomenclature.

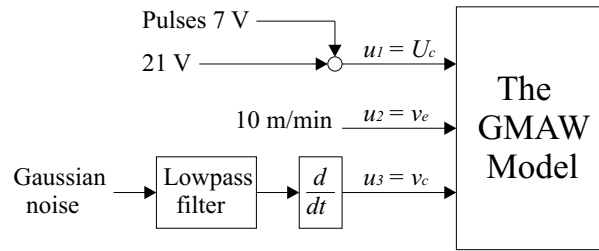


Figure 3.11: Illustration of the inputs used in the experiment.

The control voltage, u_1 , is shown in the first plot in Figure 3.12. The second plot in Figure 3.12 shows the drop detachment events generated by the PIT detachment model. As it can be seen, not all pulses result in a drop detachment.

In Figure 3.13 the welding current, $x_1 = I$, the arc length, $x_2 = l_a$, and the contact tip to workpiece distance, $x_6 = l_c$ are shown. From the first plot in Figure 3.13 it can be seen that when the sequence of pulses are initiated the current rise and fall with the pulses as it can be expected. From the second plot in Figure 3.13 it can be seen that the average arc length is increased after initiation of the pulses. This increase in arc length is caused by the increased average voltage. Also, the arc length is affected by the noise and disturbance included in the system. The last plot in Figure 3.13 shows the contact tip to workpiece distance, which varies according to bandlimited Gaussian noise.

In Figure 3.14 the drop position, $x_3 = x_d$, the drop velocity, $x_4 = v_d$, and the mass of the drop, $x_5 = m_d$ are shown. From the third plot in Figure 3.14 it can be seen that the mass of the drop grows until $t = 0.1$ s, where the first pulse is initiated, and at drop detachment the states are reset. From the first and the second plot, the oscillations of the drop can be seen.

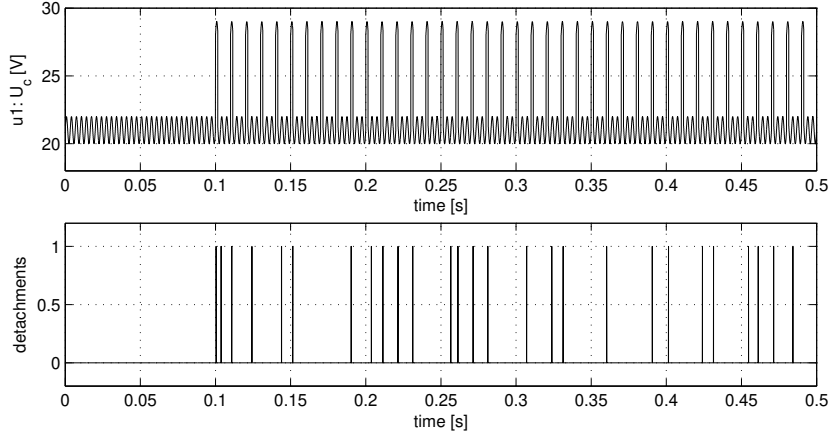


Figure 3.12: The control voltage used in the experiment. Pulses are used to provide drop detachment, and supply ripple (noise) is included.

In Figure 3.15, the electromagnetic force, F_{em} , the gravitational force, F_g , the momentum force, F_m , and the drag force, F_d , are shown. Notice that the scale on the F_{em} -plot is 5 times larger, and the scale on the F_d -plot is 5 times smaller than the scale on the plots for F_g and F_m . The electromagnetic force depends on the current, and thus, the peaks occur for strong currents. For strong currents, the electromagnetic force is much larger than the other forces, especially, the drag force and the gravitational force.

In Figure 3.16, the drop radius, r_d , and the melting speed, v_m , are shown. As it can be seen from the first plot, the drop becomes rather large before initiation of the pulses at $t = 0.1$ s. From the second plot, it can be seen that the melting speed is increased during the pulses. This is the case, as the melting speed depends on the welding current.

3.9 Discussion and Conclusion

A mathematical model describing the GMAW process has been described, and moreover, a simulation program based on the model has been developed. The model is based on mathematical descriptions of different parts of the total process

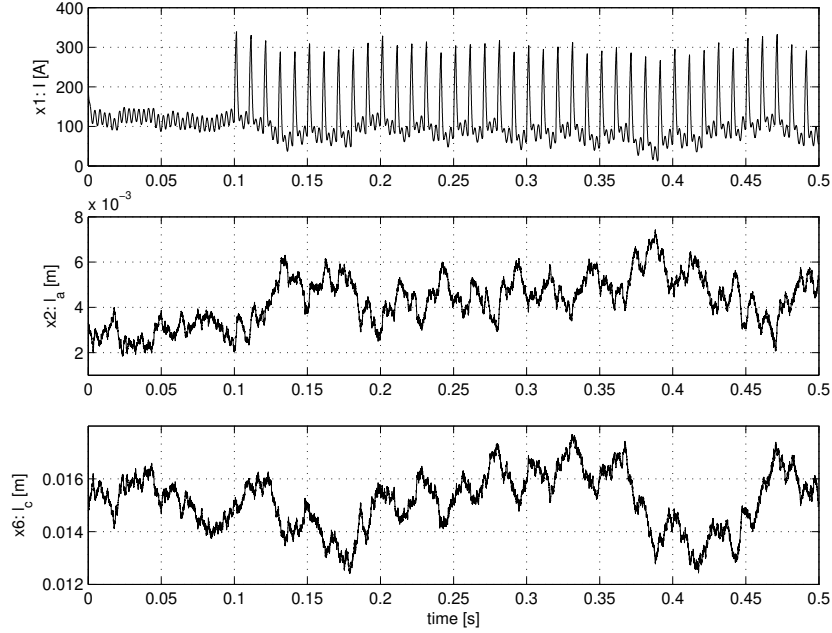


Figure 3.13: Pulses are applied to the control voltage at time $t = 0.1$ s. The plots show the welding current, the arc length, and the contact tip to workpiece distance.

excluding the weld pool. These parts are the electrical circuit, the arc, the drop dynamics, the drop detachment process, and the melting rate. The model describes the overall behavior of the process, but it is not assumed that model constitute a precise description of the process. In fact, several parts of the model are rather imprecise as explained in the following.

- The current dynamics, derived from the mathematical description of the electrical circuit, depends on the wire inductance which varies with the type of wire used and the length of the wire.
- The behavior of the arc process is very complex, and the model used in this work does only describe some basic voltage characteristic of the process. The model can only be considered to be valid for some region (current and arc length), and also, the parameters used in the model must be considered as rather imprecise. For example, the parameters depend on the exact gas mixture and the exact components in the electrode material.
- The drop dynamics is based on a lumped model describing the process as a

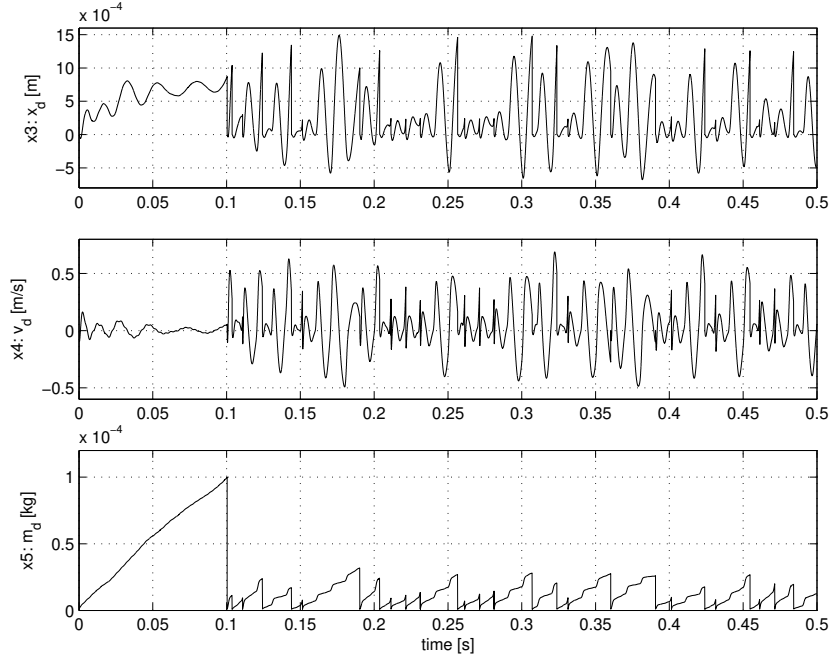


Figure 3.14: Pulses are applied to the control voltage at time $t = 0.1$ s. The plots show the drop position, the drop velocity, and the mass of the drop.

simple mass-spring-damper system, and thus, some discrepancy between the real process and the model must be expected. Also, the equation describing the electromagnetic force, which is the most significant force, can not be expected to be precise due to the assumptions made. For example, is it assumed that drop is always spherical.

- Three drop detachment models are presented, and non of these give a precise description of the complex drop detachment process.
- The melting rate model is a steady state model, and thus, in a transient phase the model is not precise.

However, in spite of these discrepancies the model should not be rejected, but instead one should be cautious when using the model for simulation and control, and likewise, one should be cautious when drawing conclusions based on the model.

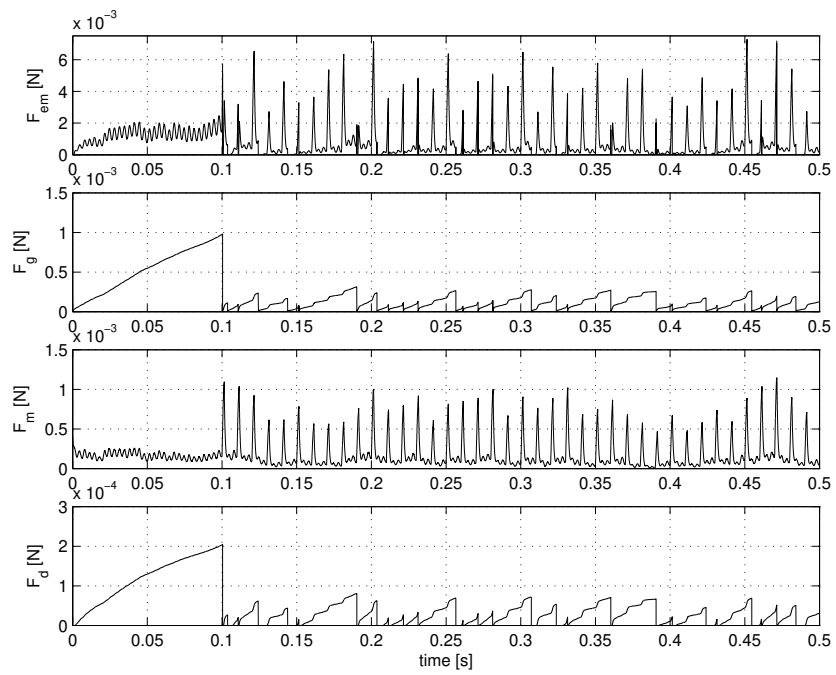


Figure 3.15: Pulses are applied to the control voltage at time $t = 0.1$ s. The plots show the electromagnetic force, the gravitational force, the momentum force, and the drag force. Notice the scale on the plots.

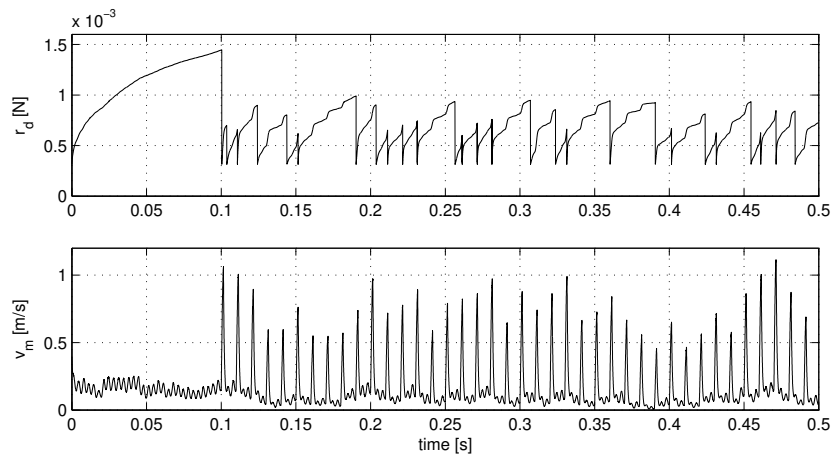


Figure 3.16: Pulses are applied to the control voltage at time $t = 0.1$ s. The plots show the drop radius and the melting speed.

Dynamic Melting Rate Model

4

In this chapter the electrode melting rate is considered. Two models are developed for calculating the melting rate. The first model is referred as the full dynamic melting rate model, and the second model is referred to as the reduced dynamic melting rate model. The second model is suited for control algorithms, while the first model is best suited for simulation due to the computations required.

4.1 Melting Rate

In GMAW, current flows through the electrode and the arc. At the tip of the electrode, assumed to be the anode, the surface is bombarded by electrons travelling through an electrical field having a very steep gradient. The electrical field accelerates the electrons and the high energy of the accelerated electrons are absorbed at the anode, causing the anode to melt. Also, Ohmic heating, caused by the current and the ohmic resistance, provides energy to the electrode. Thus, contributing to the melting of the electrode.

In Chapter 3 a steady state melting rate model was presented. For changing current, as in pulsed welding, such a model might prove to be inadequate, as it does not take melting rate dynamics into account. Therefore, in this chapter a dynamic melting rate model is derived. Moreover, derivation of a dynamic melting rate model also illuminates the actual behavior of the process, and thus, contributes to the overall understanding of the process.

In [41] a theoretical model of the GMAW process including prediction of the anode temperature profile and the melting rate is presented. Also, in [41] the anode temperature profile and the melting rate were simulated by using an energy conservation equation for describing the electrode, and moreover, to handle the moving electrode, electrode elements were added to the electrode at each time

step, and molten elements were removed. The model in [41] does not include the drop, but in [37], the drop is included in a similar melting rate model. In [35] the heat flux from the drop to the electrode is considered and theoretically explained by the thermocapillary force, also called the Marangoni effect. Basically, high temperature gradients exist within the drop causing movement of the liquid. For this reason, the heat flux from drop to electrode cannot be explained by thermal conduction. Instead, thermal convection describes this, significant, heat flux in the thermal system. In [36] the melting rate is modelled for pulsed GMAW, and results from [37] and [35] were used for developing this model.

In this chapter a dynamic melting rate model, similar to the thermal model to be found in [37], will be derived. In [37], and in similar works, the moving anode is handled by removing discrete pieces of the electrode above the melting point. This is not the case for the model derived in this chapter, because of the choice of coordinate system. Here, the coordinate system is fixed at the electrode melting point interfacing the drop. Moreover, compared to [35], the contact point heating and the effect of a changing mass are included in the model presented here. In Section 4.2, the full dynamic model describing the temperature profile and the melting rate is derived. Control of the welding process is the overall objective in this thesis, and therefore, control must be taken into account when developing a dynamic melting rate model. The full dynamic melting rate model, derived in Section 4.2, contains many states and numerous calculations, and thus, is not suitable to be included in a welding control algorithm. Therefore, in Section 4.3, the full dynamic melting rate model is recalculated and rewritten in a reduced form which is more suitable for control. In Section 4.4, the full model and the reduced model are compared, and moreover, the melting rates for both models are compared with experimental data.

4.2 A Dynamic Melting Rate Model

In this section a dynamic melting rate model is derived. This model will be referred to as the *full* dynamic melting rate model to distinguish this model from the reduced model, derived in Section 4.3. The model presented in this section has been developed in connection with a student project at Aalborg University [7].

4.2.1 System Overview

In Figure 4.1 the system is shown. T is the temperature, T_m is the melting point, T_d is the drop temperature, l_s is the stick-out, l_c is the length of the contact region, x is a distance measured from the melting point, and t is the time. To develop a detailed model of the melting rate, the system shown in this figure must be considered. Thus, the system is divided into three parts, the drop, the melting point, and the electrode above the melting point. Moreover, the latter is divided into a number of sections to characterize the temperature profile of the electrode. The three parts will be considered in the following.

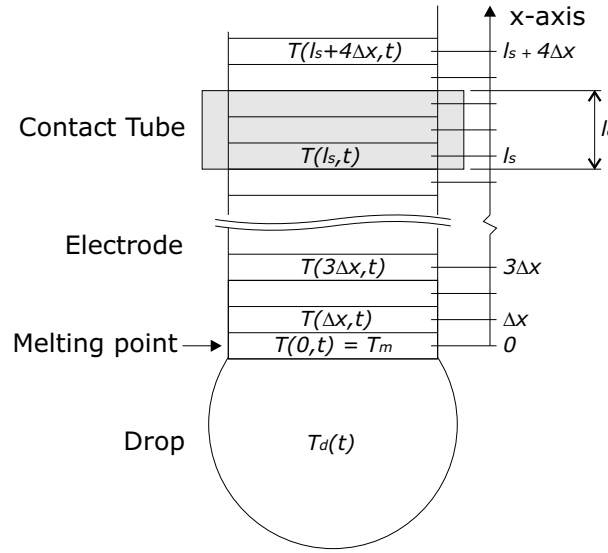


Figure 4.1: The system considered for deriving a model describing the melting rate. The drop, the melting point, the solid electrode, and the contact point are included.

4.2.2 The Drop

During welding the solid electrode is melted and liquid metal is added to the drop. At some point the drop detaches and the process starts all over. To characterize the drop, conservation of mass and energy is considered.

From drop beginning to drop detachment, the mass of the drop can be described

by an equation describing the conservation of mass.

$$\frac{dm_d}{dt} = v_m \rho A \quad (4.1)$$

m_d is the mass of the drop, v_m is the melting speed, ρ ($= \rho_e$) is the metal density, and A ($= A_e$) is the cross section area of the electrode.

Let h_d be the specific inner energy (heat per mass) of the drop, let T_m be the melting point temperature, let h_m the heat of fusion, let c be the specific heat capacity below the melting point, and let c_m be the specific heat capacity above the melting point, see Figure 4.2. Let P_a be the anode heat flow, primarily originating from electron kinetic energy and electron absorption, and furthermore, let P_d be the drop heat flow, expressing the heat flux between the drop and solid electrode. Using these terms conservation of energy for the drop can be expressed as

$$\begin{aligned} \frac{d(m_d h_d)}{dt} &= h_d \frac{dm_d}{dt} + m_d \frac{dh_d}{dt} = P_a + v_m \rho A (c T_m + h_m) - P_d \\ &\Rightarrow \\ [c T_m + h_m + c_m (T_d - T_m)] v_m \rho A + m_d c_m \frac{dT_d}{dt} \\ &= P_a + v_m \rho A (c T_m + h_m) - P_d \\ &\Leftrightarrow \\ c_m (T_d - T_m) v_m \rho A + m_d c_m \frac{dT_d}{dt} &= P_a - P_d \end{aligned} \quad (4.2)$$

According to [29] the heat supplied to the tip of the electrode comes from, respectively, kinetic energy of the electrons and the energy of condensation. A high anode temperature causes electrons to be emitted from the anode, and thus, surrounding the anode. This cloud of electrons generates a thin, but very strong electrical field. Electrons are accelerated and collect considerable kinetic energy in the electrical field, and next, when colliding with the anode surface the energy is released. Colliding electrons are absorbed into the lattice of the metal and energy is released in this process. The energy released corresponds to the work function ϕ_w , which is the minimum energy needed to remove an electron from the surface. In [29] the following equation for the anode heat flow, P_a , is presented. V_{an} is the anode voltage.

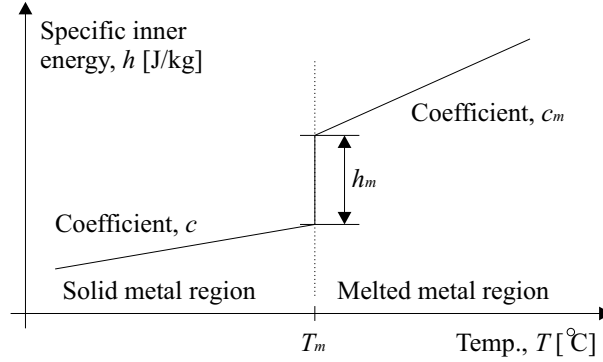


Figure 4.2: The specific inner energy, h , as a function of the temperature. T_m is the melting temperature.

$$P_a = c_{an}(V_{an} + \phi_w)I \quad (4.3)$$

Some energy is lost to ionization of gas molecules and metal vapors, and a minor fraction of the energy is lost to radiation. The constant c_{an} accounts for these losses.

P_d expresses the heat flow between the drop and the solid electrode, but it is difficult to find an equation describing this flow. Close to the arc the temperature is very high, but at the solid electrode boundary, the temperature equals the melting point temperature. This gives, as described in [35], a thermocapillary force that causes rotation within the drop from the bottom to top. This phenomenon is called the Marangoni effect. The Lorentz force from the welding current and the induced magnetic field also produces rotation within the drop, although, this rotation is directed around a center vertical axis. Rotation within the drop moves hot particles close to the solid boundary surface, and thus, heat flow is best described by thermal convection and not thermal conduction, see [35]. Also, in [35] experiments and calculations show that thermal convection compared to thermal conduction is 10 to 20 times as significant in this liquid to solid interface layer. In [35] an equation describing the heat flow is derived, and in [37] some dependence between the Peclet Number (Pe) and the heat flow is reported, and moreover some dependence between the Peclet Number and the drop temperature. Thus, a dependence also exists between the drop temperature and the heat flow. This leads to the simple expression, used in this thesis, for the heat flow P_d .

$$P_d = K_c(T_d - T_m) \quad (4.4)$$

K_c is a constant and should be chosen, such that, the convection is 10 to 20 times as significant as the thermal conduction [35].

4.2.3 The Electrode and The Contact Point

The solid part of the electrode is divided into a number of small elements as shown in Figure 4.1. The temperature of each of these elements can be calculated using the principle of conservation of energy, and thus, all elements constitute a dynamic temperature profile of the electrode. Equations describing the conservation of energy must take into account the electrode movement, and therefore, a system of particles is considered as described in [39].

The inner energy, E_p , for a system of particles (see Figure 4.1) at time instant t is given below. T is the temperature, x is the element location, and Δx is the length of the elements.

$$E_p(x, t) = A\rho cT(x, t)\Delta x \quad (4.5)$$

The inner energy for the system of particles at time instant $t + \Delta t$ is expressed below.

$$\begin{aligned} E_p(x, t + \Delta t) &= A\rho cT(x, t + \Delta t)\Delta x + A\rho v_m cT(x - \Delta x, t + \Delta t)\Delta t \\ &\quad - A\rho v_m cT(x, t + \Delta t)\Delta t \end{aligned} \quad (4.6)$$

The total heat flux, P_l , originating from heat conduction at the element boundaries can be expressed as below. λ is the thermal conductivity.

$$\begin{aligned} P_l(x, t) &= P_{l,in}(x, t) - P_{l,out}(x, t) \\ &= A\lambda \frac{T(x - \Delta x, t) - T(x, t)}{\Delta x} - A\lambda \frac{T(x, t) - T(x + \Delta x, t)}{\Delta x} \\ &= A\lambda \frac{T(x - \Delta x, t) - 2T(x, t) + T(x + \Delta x, t)}{\Delta x} \end{aligned} \quad (4.7)$$

$$\Rightarrow \Delta E_l(x, t) = A\lambda \frac{T(x - \Delta x, t) - 2T(x, t) + T(x + \Delta x, t)}{\Delta x} \Delta t \quad (4.8)$$

Also, an element is subject to an incremental change in energy due to Ohmic heating. ψ ($= \rho_r$) is the resistivity of the electrode.

$$P_J(x, t) = \frac{I^2}{A^2} \psi A \Delta x \Rightarrow \quad (4.9)$$

$$\Delta E_J(x, t) = \frac{I^2}{A} \psi \Delta x \Delta t \quad (4.10)$$

Now, the principle of conservation of energy gives the following result.

$$E_p(x, t + \Delta t) - E_p(x, t) = \Delta E_l(x, t) + \Delta E_J(x, t) \quad (4.11)$$

$$\Rightarrow \begin{aligned} A\rho cT(x, t + \Delta t)\Delta x + A\rho v_m cT(x - \Delta x, t + \Delta t)\Delta t - A\rho v_m cT(x, t + \Delta t)\Delta t \\ - A\rho cT(x, t)\Delta x = \Delta E_l(x, t) + \Delta E_J(x, t) \end{aligned} \quad (4.12)$$

Dividing by Δx , and Δt , and letting $\Delta x \rightarrow 0$ and $\Delta t \rightarrow 0$.

$$A\rho cT_t(x, t) = A\rho v_m cT_x(x, t) + A\lambda T_{xx}(x, t) + \frac{I^2}{A} \psi \quad (4.13)$$

where the following notation is used

$$T_x = \frac{\partial T(x, t)}{\partial x} \quad (4.14)$$

$$T_{xx} = \frac{\partial^2 T(x, t)}{\partial x^2} \quad (4.15)$$

$$T_t = \frac{\partial T(x, t)}{\partial t} \quad (4.16)$$

Equation (4.13) characterizes the temperature of a chosen element above the melting point, and thus, equation (4.13) can be used for simulation of the temperature profile along the electrode. However, at the contact point, the model needs to be reconsidered. At the contact point the contact tube touches the moving electrode,

and current flows from the tube to the electrode. A small voltage drop can be expected at the contact point, and thus, a contact resistance, R_c , can be used as a model. If it is assumed that contact is established in some interval $N_c \Delta x$, then the contact point can be modelled by modifying the resistivity ψ . Notice that ψ is a function of the temperature, and see Figure 4.1. ψ_1 is the resistivity of the electrode material, and ψ_2 is the resistivity in the contact point region.

$$\begin{aligned}\psi(x, T) &= \psi_1(T), \quad x < l_s \\ \psi(x, T) &= \psi_2(T), \quad l_s \leq x < l_s + N_c \Delta x \\ \psi(x, T) &= 0, \quad x \geq l_s + N_c\end{aligned}\tag{4.17}$$

4.2.4 The Melting Point and The Melting Speed

In this section the melting point is considered. By doing this it is possible to derive an equation expressing the melting speed, v_m , or melting rate, M_R .

The inner energy, E_p , of the melting point element at time instant t is given below.

$$E_p(0, t) = A \rho c T_m \Delta x \tag{4.18}$$

The inner energy, E_p , of the melting point element at time instant $t + \Delta t$ is given below. See Figure 4.3 showing the system of particles at time instant t and at time instant $t + \Delta t$.

$$E_p(0, t + \Delta t) = A \rho c T_m \Delta x + A \rho v_m h_d \Delta t - A \rho v_m c T_m \Delta t \tag{4.19}$$

The melting point element is subject to change in energy due to thermal convection from the drop, thermal conduction from the upper solid electrode element, and moreover, Ohmic heating. These energy contributions can be expressed as

$$\Delta E_d = P_d \Delta t = K_c (T_d - T_m) \Delta t \tag{4.20}$$

$$\Delta E_l = P_l \Delta t = A \lambda \frac{T(\Delta x, t) - T(0, t)}{\Delta x} \Delta t \tag{4.21}$$

$$\Delta E_J = P_J \Delta t = \frac{I^2}{A} \psi \Delta x \Delta t \tag{4.22}$$

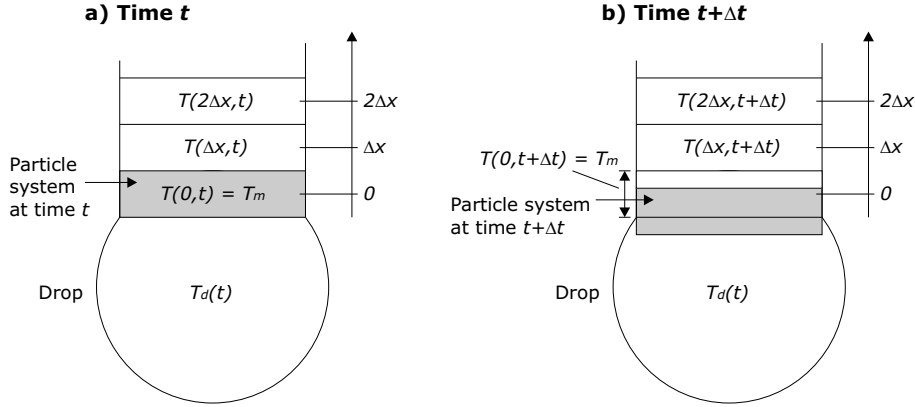


Figure 4.3: At time t the particle system has the melting temperature, but is still a part of the solid electrode. At time $t + \Delta t$ some part of the particle system is part of the liquid drop.

Now, it is assumed that $c = c_m$, see Figure 4.2. Then the conservation of energy gives the following result.

$$\begin{aligned}
 E_p(0, t + \Delta t) - E_p(0, t) &= \Delta E_d + \Delta E_l + \Delta E_J \\
 \Rightarrow \\
 A\rho v_m h_m \Delta t &= \Delta E_d + \Delta E_l + \Delta E_J
 \end{aligned} \tag{4.23}$$

Dividing by Δt , and letting $\Delta x \rightarrow 0$ results in an equation expressing the melting speed, v_m .

$$v_m = \frac{P_d + P_l}{A\rho h_m} = \frac{K_c(T_d - T_m) + A\lambda T_x(0, t)}{A\rho h_m} \tag{4.24}$$

Also, this can be expressed as a melting rate, M_R .

$$M_R = v_m A = \frac{P_d + P_l}{\rho h_m} \tag{4.25}$$

4.2.5 Model Summary

The model is illustrated in Figure 4.4, and below, the equations used are summarized.

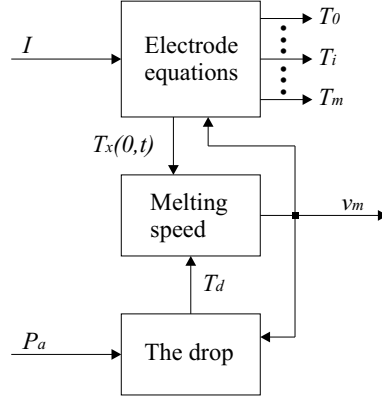


Figure 4.4: Illustration of the full dynamic melting speed model.

Dynamic equation for the mass of the drop:

$$\frac{dm_d}{dt} = v_m \rho A \quad (4.26)$$

Dynamic equation for the drop energy:

$$c_m(T_d - T_m)v_m \rho A + m_d c_m \frac{dT_d}{dt} = P_a - K_c(T_d - T_m) \quad (4.27)$$

Partial differential equation describing the dynamics of the electrode, including the contact point:

$$A \rho c T_t(x, t) = A \rho v_m c T_x(x, t) + A \lambda T_{xx}(x, t) + \frac{I^2}{A} \psi \quad (4.28)$$

Description of the contact point:

$$\begin{aligned} \psi &= \psi_1, \quad x < l_s \\ \psi &= \psi_2, \quad l_s \leq x < l_s + N_c \Delta x \\ \psi &= 0, \quad x > l_s + N_c \end{aligned} \quad (4.29)$$

Differential equation describing the melting speed, or alternatively, the melting rate, see equation (4.25):

$$v_m = \frac{K_c(T_d - T_m) + A\lambda T_x(0, t)}{A\rho h_m} \quad (4.30)$$

4.2.6 Steady State Model Behavior

In the former sections a model describing the dynamic electrode melting system has been derived. In this section a steady state temperature profile of the solid electrode will be presented, simulated at different current levels. This will be done to illustrate the steady state behavior of the process which, in Section 4.3, will be used for developing a reduced order model.

The model describing the dynamic electrode melting system has been implemented in Simulink. The electrode is chosen to be a 1 mm stainless steel electrode, and thus, the physical parameters describing such electrode have been used in the simulations, see the Nomenclature. Three plots in Figure 4.5 shows the steady state temperature profile of the electrode for different currents. Respectively, plots for 80 A, 130 A, and 180 A are shown. 100 elements are used to characterize the electrode, where each element has a length of $\Delta x = 0.0002$ m. Moreover, a contact point resistance is distributed from element 51 to element 60. From Figure 4.5 it can be seen that different temperature gradients are caused by the different currents used. However, in spite of different gradients at different currents, the temperature profile can be characterized by a high gradient part and a flat part.

4.3 A Reduced Melting Rate Model

In Section 3.6 a simple steady state melting rate model was presented. Unlike the model derived in Section 4.2, which is computational intensive, this model is a simple model suitable for control. However, the steady state melting rate model does not capture the melting rate dynamics. Therefore, the aim in this section is to develop a dynamic melting rate model suitable for control. From the temperature profile shown in Figure 4.5 some conclusions can be drawn. First, in the solid electrode close to the melting point, the temperature gradient is very steep. Second, near the contact tube the temperature gradient is rather flat, but the temperature is somewhat above the ambient temperature, T_0 . Therefore, it

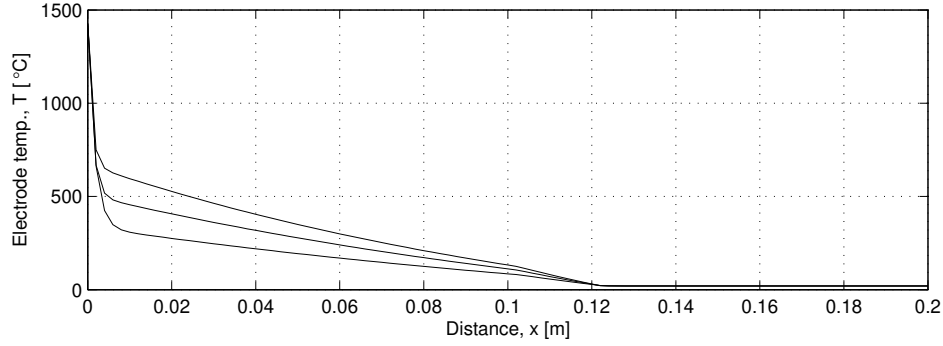


Figure 4.5: Electrode temperature profiles at different welding currents, respectively, 80 A, 130 A, and 180 A. The lower curve corresponds to 80 A, the middle curve to 130 A, and the upper to 180 A.

might be possible to simulate the electrode temperature profile using only a few elements.

4.3.1 Reduction of the Model

The solid electrode is divided into a number of small elements close to the melting point to account for the steep gradient, and then, the rest of the electrode is divided into a number of larger elements. Here, the "electrode" refers to the piece of metal from the drop to the contact point, plus a piece of electrode wire behind the contact point. In Figure 4.6 this distribution of small and large elements are shown, and as illustrated, the large elements consists of the three elements at distance M , N , and P , respectively. The contact point is located in element N .

In general the derivation of the reduced model is similar to the derivations found in Section 4.2. However, the elements at distance L and M need to be considered, as these elements are the interface between the small and the large elements. Before considering the two elements, lets us introduce the following notation.

$$T_L = T(L, t) \quad (4.31)$$

$$T_M = T(M, t) \quad (4.32)$$

$$T_N = T(N, t) \quad (4.33)$$

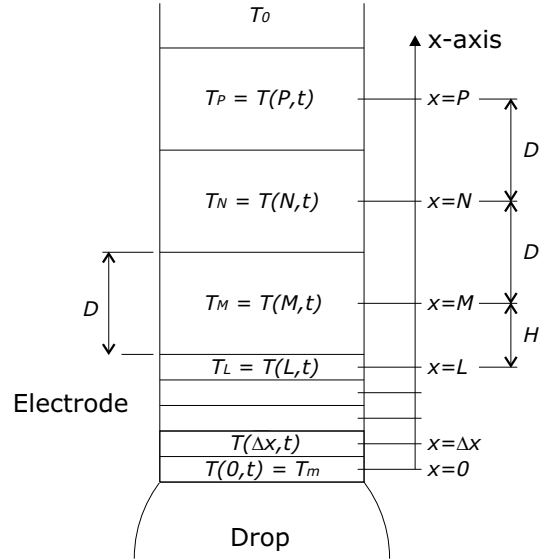


Figure 4.6: For the reduced model, the electrode is divided into small elements close to the drop, but otherwise, it is divided into larger elements.

$$T_P = T(P, t) \quad (4.34)$$

First, the element M will be considered. The inner energy, E_p , of the element at $x = M$, and at time instant t is given below. Notice, that in the following

$$E_p(M, t) = A\rho cT_M D \quad (4.35)$$

The inner energy, E_p , of the element at $x = M$, and at time instant $t + \Delta t$ is given below.

$$E_p(M, t + \Delta t) = A\rho cT(M, t + \Delta t)D + A\rho v_m cT_L \Delta t - A\rho v_m cT_N \Delta t \quad (4.36)$$

The incremental change in energy due to thermal conduction can be written as below. D is the length between element N and M , and H is the length between element M and L , see Figure 4.6.

$$P_l(M, t) = P_{l,in}(M, t) - P_{l,out}(M, t)$$

$$\begin{aligned}
 &= A\lambda \frac{T_L - T_M}{H} - A\lambda \frac{T_M - T_N}{D} \\
 &= \frac{A\lambda}{DH} (DT_L - DT_M - HT_M + HT_N) \quad (4.37)
 \end{aligned}$$

$$\Rightarrow$$

$$\Delta E_l(M, t) = \frac{A\lambda}{DH} (DT_L - DT_M - HT_M + HT_N) \Delta t \quad (4.38)$$

The incremental change in energy due to Ohmic heating can be written as

$$\Delta E_J(M, t) = \frac{I^2}{A} \psi D \Delta t \quad (4.39)$$

Now, balance of energy gives a discrete time equation describing the solid electrode temperature. A discrete time representation is used to avoid simulation between sample times, represented by Δt time intervals.

$$E_p(M, t + \Delta t) - E_p(M, t) = \Delta E_l(M, t) + \Delta E_J(M, t) \quad (4.40)$$

$$\Rightarrow$$

$$\begin{aligned}
 &A\rho cT(M, t + \Delta t)D + A\rho v_m c(T_L - T_N)\Delta t - A\rho cT_M D \\
 &= \frac{A\lambda}{DH} (DT_L - DT_M - HT_M + HT_N) \Delta t + \frac{I^2}{A} \psi D \Delta t \quad (4.41)
 \end{aligned}$$

Now, an equation describing the temperature in the element at distance M has been found. The equation describing the element at distance L can be found in a similar way. The result is

$$\begin{aligned}
 &A\rho cT(L, t + \Delta t)H + A\rho v_m c(T(L - \Delta x, t) - T_M)\Delta t - A\rho cT_L H \\
 &= \frac{A\lambda}{H\Delta x} (HT(L - \Delta x, t) - HT_L - \Delta x T_L + \Delta x T_M) \Delta t + \frac{I^2}{A} \psi H \Delta t \quad (4.42)
 \end{aligned}$$

The equations describing the drop dynamics, the melting rate, and the uniform elements in the solid part of the electrode are similar to the equations found in Section 4.2. However, the contact resistance is accounted for in the element at distance N .

4.4 Simulations

A simulation program for testing the dynamic melting speed models has been developed. The program has been developed in Simulink, and consists of three parts: A part calculating the melting speed based on the full dynamic melting speed model, a part calculating the melting speed based on the reduced dynamic melting speed model, and a part calculating the melting speed based on the steady state model stated in equation (3.36). In Figure 4.7 the structure of the simulation program for a dynamic melting speed model is shown. Same structure is used for both models.

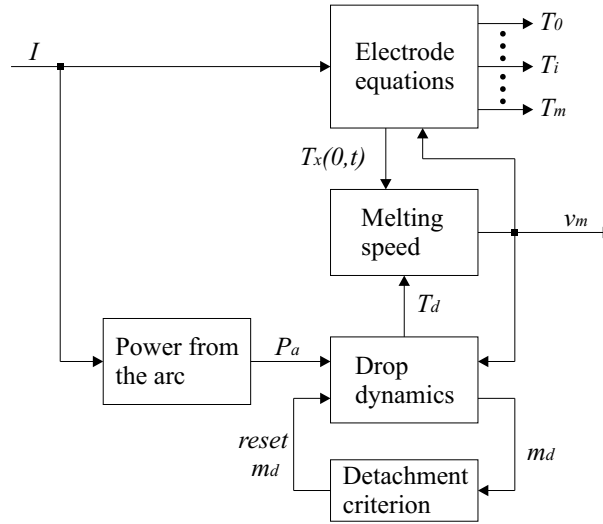


Figure 4.7: The structure of the simulation program for the dynamic melting speed algorithms.

In the simulation program, drop detachment events are generated in a simple way, as the mass of the drop, m_d , is reset when the mass exceeds a given fixed level. If one of the melting speed models was to be implemented in a simulation program simulating the whole GMAW process, drop detachment events would be generated from one of the criteria found in Section 3.5.

For calculating the melting speed using the full dynamic melting speed model, the electrode is partitioned into 100 elements of length $\Delta x = 0.2$ mm. Current

is flowing through half of the elements, as the rest of the elements are behind the contact point. For calculating the temperature of each of those elements, it must be considered how $T_x(x, t)$, $T_{xx}(x, t)$, and $T_t(x, t)$ are calculated, see equation (4.13). The following approximations are used. Δx is the length of each element, and Δt is the time between each sample, that is, the sample time T_s .

$$T_x = \frac{\partial T(x, t)}{\partial x} \approx \frac{T(x + \Delta x, t) - T(x, t)}{\Delta x} \quad (4.43)$$

$$T_{xx} = \frac{\partial^2 T(x, t)}{\partial x^2} \approx \frac{T(x + \Delta x, t) + 2T(x, t) - T(x - \Delta x, t)}{(\Delta x)^2} \quad (4.44)$$

$$T_t = \frac{\partial T(x, t)}{\partial t} \approx \frac{T(x, t + \Delta t) - T(x, t)}{\Delta t} \quad (4.45)$$

So, we have the following expression for the temperature at $T(x, t + \Delta t)$. Thus, using this expression, it is possible to calculate the temperature of all elements one time step into the future.

$$\begin{aligned} T(x, t + \Delta t) = T(x, t) + \Delta t \left(v_m \frac{T(x + \Delta x, t) - T(x, t)}{\Delta x} \right. \\ \left. + \frac{\lambda}{\rho c} \frac{T(x + \Delta x, t) + 2T(x, t) - T(x - \Delta x, t)}{(\Delta x)^2} + \frac{I^2}{\rho c A^2} \psi \right) \end{aligned} \quad (4.46)$$

For calculating the melting speed using the reduced order dynamic melting speed model, the electrode is partitioned into 4 small elements close to the melting point, and the rest of the electrode is partitioned into 3 large elements. The small elements are similar to the elements used for the full dynamic melting speed model, and thus, 4 elements of length $\Delta x = 0.2$ mm are used. The 3 large elements each have a length of 4.2 mm, and are centered around the distances $x = M$, $x = N$, and $x = P$, respectively, see Figure 4.6. The P -element is behind the contact point, and the N -element includes the contact point resistance.

The temperature of each element in the reduced order dynamic melting speed model are calculated in a similar way as the elements in the full dynamic melting speed model, except for the two elements in the interface between the small and the large elements. These elements are element L and element M , see Figure 4.6. The temperature of these interface elements are calculated using equation (4.41) and equation (4.42). So, $T(M, t + \Delta t)$ is isolated in equation (4.41), and $T(L, t + \Delta t)$ is isolated in equation (4.42).

Five experiments with, respectively, the full dynamic melting speed model, the reduced dynamic melting speed model, and the steady state model have been carried out using the simulation program. For each experiment a step in the input current, I , is applied. The shape of each input current signal is given below.

- Experiment 1: The current is changed from 100 A to 50 A at time $t = 0.02$ s.
- Experiment 2: The current is changed from 100 A to 200 A at time $t = 0.02$ s.
- Experiment 3: The current is changed from 100 A to 350 A at time $t = 0.02$ s.
- Experiment 4: The current is changed from 100 A to 200 A at time $t = 0.02$ s. Moreover, a 300 Hz sinusoidal signal with an amplitude of 10 A is added to the input current.
- Experiment 5: The current is changed from 100 A to 200 A at time $t = 0.02$ s. Moreover, a Gaussian noise signal with a mean equal to zero and a variance equal to 100 is added to the input current.

The 300 Hz sinusoidal signal in experiment 4 is applied for simulating the effect of the voltage ripple from the welding machine.

In all experiments, the values for the different constants and parameters used can be found in the Nomenclature, except for the parameters for P_a in equation (4.3). For P_a , the anode voltage, V_{an} , is set to 5.5 V, and the anode constant, c_{an} , is set to 0.5. However, to be able to adjust the steady state level of the dynamic melting models, the work function, ϕ_w , is made a function of the current, I . Thus, $\phi_w = \phi_w(I)$. Also, in all experiments a sample time $T_s = \Delta t = 0.1$ ms is used.

In Figure 4.8, the three melting speeds are shown for experiment 1. The work function $\phi_w(I)$ has been adjusted, such that, the steady state value generated by the full dynamic melting speed model equals the melting speed value generated by the steady state model. The same value for $\phi_w(I)$ is used in the reduced model.

In Figure 4.9, the three melting speeds are shown for experiment 2. Like experiment 1, the work function has been adjusted. As it can be seen, the melting speed calculated by the reduced dynamic melting speed model has a different steady state value when compared to the value from the full dynamic melting speed model.

In Figure 4.10, the three melting speeds are shown for experiment 3. Like experiment 2, the melting speed calculated by the reduced dynamic melting speed

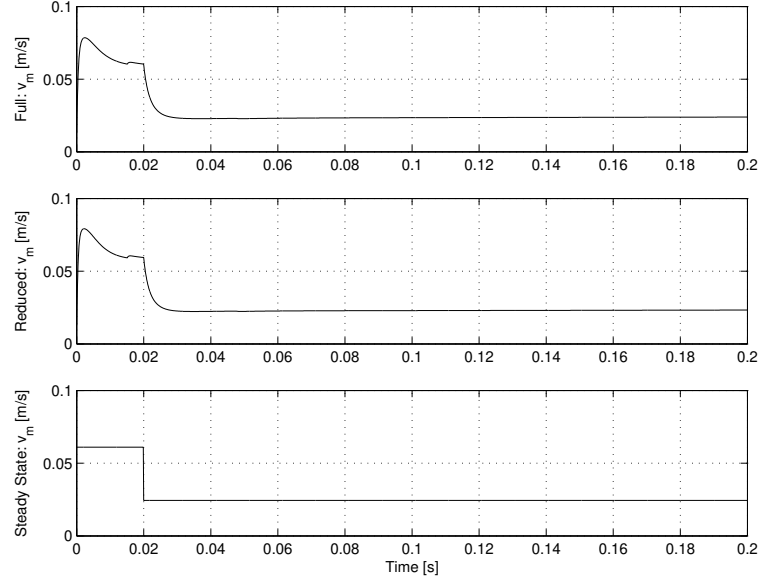


Figure 4.8: Experiment 1: The melting speed calculated by the three models given a step in welding current from 100 A to 50 A.

model has a different steady state value when compared to the value from the full dynamic melting speed model.

To investigate the transients of the melting speed models, the transient phase of experiment 3 is plotted in Figure 4.11. Here, it can be seen that the response generated by the reduced model is almost equal to the response of the full model. Both have a time constant of around 0.6 ms, corresponding to a bandwidth of around 1.7 kHz. Also, notice the jump in the melting speed around 0.0225 s which is caused by a drop detachment. The drop detachment results in a smaller drop, and less energy is needed for increasing the temperature of a small drop.

So, in the transient phase, the reduced model calculates a melting speed almost identical to the full model, but in steady state there are some differences between the melting speed calculated by the reduced model and the dynamic model. This can be explained in the following way. In the transient phase, the response is determined by a few elements close to the melting point, and close to the melting point the same type of elements are used for both the reduced model and the full

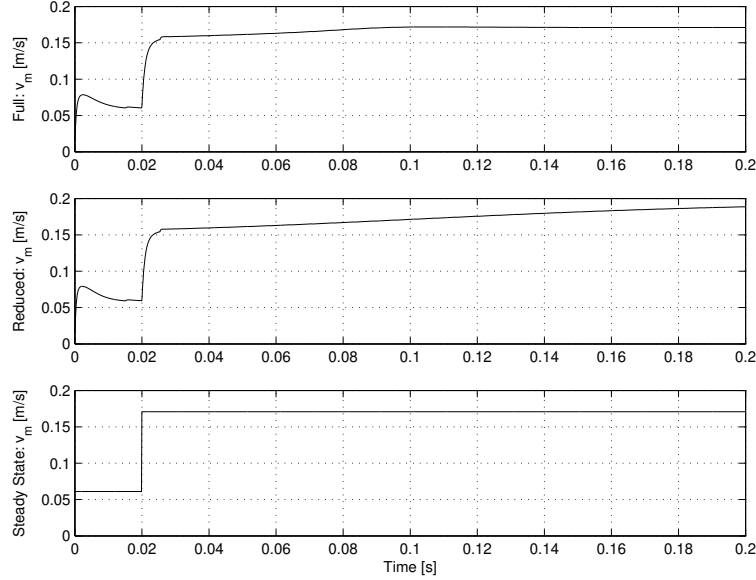


Figure 4.9: Experiment 2: The melting speed calculated by the three models given a step in welding current from 100 A to 200 A.

model. However, the same type of elements are not used for the other part of the electrode. For the full model small elements are used, but for the reduced model large elements are used. The large elements do only give a crude representation of the temperature profile, and this results in the discrepancy. However, the discrepancy between the reduced model and the full model in steady state does not mean that the reduced cannot be used. Rather, it means that the reduced model must be tuned. However, this will not be pursued further in this work.

In Figure 4.12 the input current signal used for, respectively, experiment 4 and experiment 5 are shown. For experiment 4, the melting speeds calculated by the three models are shown in Figure 4.13. In the full model and the reduced model the current signal is filtered by the dynamical system, and thus, the amplitude of the oscillations is dampened. However, no dynamics are included in the steady state melting rate model, and thus, for this model the 300 Hz signal is not dampened. For experiment 5, the melting speeds calculated by the three models are shown in Figure 4.14. Likewise, the melting speeds calculated by the full and the reduced model are dampened, and again, unfiltered noise can be observed in the

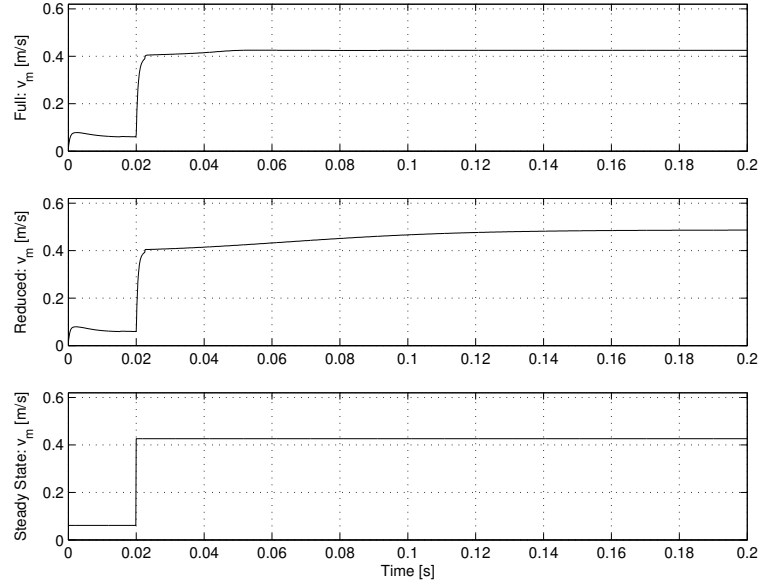


Figure 4.10: Experiment 3: The melting speed calculated by the three models given a step in welding current from 100 A to 350 A.

melting speed calculated by the steady state model.

4.5 Discussion and Conclusion

To develop a model describing the melting rate of the electrode, the electrode has been partitioned into three subsystems, which are the drop, the melting point, and the solid electrode. Moreover, the solid part of the electrode was divided into a number of small elements to describe the temperature profile of the electrode. Using this approach a melting rate model was developed, and the model was referred to as the full dynamic melting rate model. To reduce the order of the melting rate model, and thus, to reduce the number of calculations needed, the model was reduced considerably by using an alternative partition of the solid electrode. The model obtained in this way was referred to as the reduced dynamic melting rate model, which, because of the relative low model order, is better suited for control. Alternatively, both dynamic melting rate models were formulated as melting speed models.

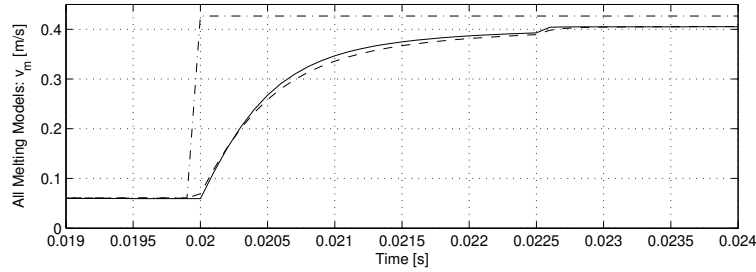


Figure 4.11: The transient phase of experiment 3.

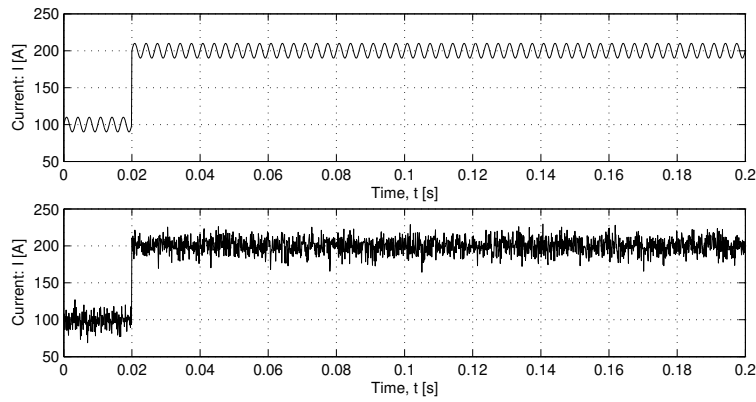


Figure 4.12: The input current signals used for, respectively, experiment 4 and 5.

Simulations showed good agreement between the full dynamic melting rate model and the reduced melting rate model in the transient phase of a step response, but in steady state a discrepancy between the two models was present. However, this was considered as a matter of tuning the reduced model, and thus, it was not considered as a problem for the reduced model. It should be mentioned that the dynamic melting rate models presented in this chapter will not be used in the rest of the thesis. Instead the steady state melting rate model will be used because of the simplicity of this model. However, using the more exact melting rate models presented in this chapter can be considered as a way to improve the methods or algorithms utilizing the simple steady state melting rate model.

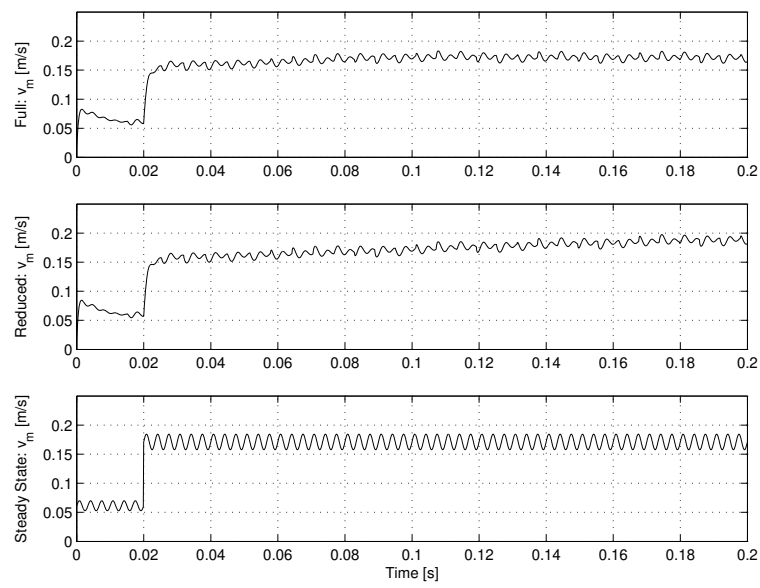


Figure 4.13: Experiment 4: The melting speed calculated by the three models. A step in the welding current from 100 A to 200 A plus a 300 Hz sinusoidal signal is applied.

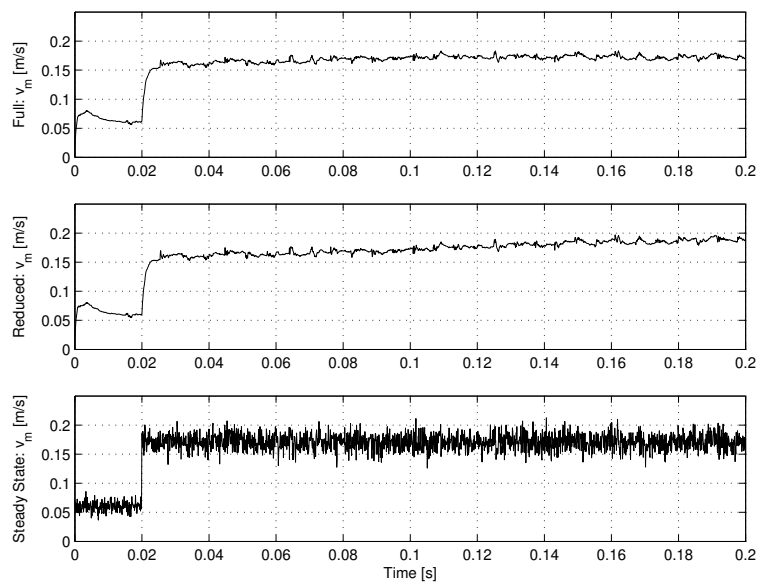


Figure 4.14: Experiment 5: The melting speed calculated by the three models. A step in the welding current from 100 A to 200 A plus a Gaussian noise signal is applied.

Part II

Controlling the Gas Metal Arc Welding Process

Objectives and Control Topology

5

In this chapter control of the GMAW process is considered. Different control configurations are discussed, and also, the different tasks which should be addressed with respect GMAW control are considered. Moreover, a number of specific objectives for the control system are presented.

5.1 Control and Objectives in GMAW

In Chapter 1, the overall objective of this thesis is stated. The overall objective is to optimize the control algorithms controlling the manual (hand-held) pulsed GMAW process, with the aim of enhancing the quality of welded joints. However, it is rather unclear what is meant by an optimization of the control algorithms, and also, is it not clear, what is meant by the quality of a weld. In this section, these unclear point will be addressed, and as a result, a number of specific objectives will be defined. Notice, that in this thesis, pulsed GMAW is considered as a special case of spray GMAW, and also, short arc GMAW is not considered.

First, let us consider quality. Normally, the quality of a weld is characterized by parameters such as penetration and grain size in the welded area. In general, quality is characterized with respect to characteristics of the welded workpiece. However, in this thesis, focus is not on the workpiece, but rather on the part of the process involving the electrical circuit, the electrode melting, and the forces acting on the drop. Therefore, instead of relating quality to workpiece characteristics, it would be preferable to find a number of derived characteristics, which could be linked to the process under consideration. To be able to arrive at some derived quality characteristics a specific welding material is considered. The selected material is stainless steel. However, in spite of the specific material considered, the derived objectives can be considered as general objectives for GMAW control.

Stainless steel is a steel alloy, that contains some alloy elements, which gives the metal some desired properties. These properties must also be present after a weld. However, during a weld, if the steel becomes too hot, it might lose the alloy properties. To prevent this loss of properties, the temperature in the melting pool must be kept low, and thus, the welding process must be performed using a relative low amount of energy. Also, a low amount of energy used, corresponds to a low heat input into the workpiece, and in general, the heat input should be as low as possible. Therefore, one objective is to minimize the energy used in the welding process. Actually, when compared with ordinary spray GMAW, pulsed GMAW is a way to obtain a process in which less energy is transferred into the weld pool. However, to minimize the energy the pulsed GMAW process must be considered with respect to energy minimization, and a way to obtain such energy minimization is to ensure a small arc length during welding.

A small arc length, or minimal arc length, is preferred for another reason. During welding the operator needs to control the path of the arc between the electrode and the workpiece, and this path is less difficult to control having a small arc length. For example, when welding along a gap between two pieces, or along two orthogonal workpieces, a long arc can be difficult to focus. A small arc is easier to focus during welding, that is, a small arc has less tendency to jump from one spot to another on the workpieces. So, to achieve the optimal condition for arc direction control, we want to minimize the arc length. However, if the arc length becomes too small, short circuits between the electrode and the workpiece will occur. In general, the number of short circuits should be minimized, as, otherwise, a poor weld might be the result.

Normally, in pulsed welding, the current pulses are used for detaching drops at the tip of the electrode, such that, one drop is detached for every one pulse. Lack of drop detachment or multiple drop detachments for each pulse will have a negative effect on the quality of the weld. Probably, the negative effect on the quality is caused by the irregular characteristics of the detaching drops, for example, an irregularly drop size and drop velocity. Therefore, one drop per pulse (ODPP) must be maintained during the pulsed welding process.

Now, based on the preceding discussion a number of specific objectives can be stated.

- The welding process must be performed using a minimal amount of energy.

- A minimal arc length must be obtained.
- Short circuits must be avoided.
- In pulsed GMAW, one drop must be detached for every pulse (ODPP).

In the following section the control system needed to control the pulsed GMAW will be considered. First, in Section 5.2, the general control system architecture is considered. Next, in Section 5.2.1, metal transfer control is considered. Metal transfer control, basically, is the mechanism which ensures drop detachment. Afterwards, in Section 5.2.2, arc length control is addressed, and, in Section 5.2.3, supervision in the control system is discussed.

5.2 Control Configurations

In this section the architecture, or configuration, of the control system is considered. First, let us consider the GMAW process, and define the inputs controlling the process, and also, the outputs from the process used for control.

The terminal voltage, U_t , can be considered as an input to the GMAW process. The terminal voltage is the voltage between the machine terminals, see Figure 3.1. The electrode is fed from the welding machine, and thus, the electrode speed can also be considered as an input to the process. However, in general, in manual welding systems the electrode speed is set to some fixed value before the start of a weld. Therefore, in this thesis the electrode speed is not considered as an input. Rather the electrode speed becomes a fixed parameter in the system. The outputs are measurements, which are also normally used in manual welding systems. The outputs are the measured terminal voltage, U_{tm} , and the measured welding current, I_{wm} . So, for control, the following inputs and outputs can be used.

- Input: The terminal voltage, U_t .
- Output: The measured terminal voltage, U_{tm} .
- Output: The measured welding current, I_{wm} .

Now, let us consider ordinary spray GMAW (not pulsed), and suppose we want to control the arc length. In fact, being able to control the arc length is probably the single most important thing in GMAW control. Using the input and the outputs, it is possible to develop a controller able to control the arc length. Such a controller could be based on a model of the GMAW process. However, for the modern type of welding machines, considered in this thesis, a terminal voltage

cannot be applied directly to the process. Instead, from the point of view of the internal controller, a signal to the inverter can be applied. This is a Pulse Width Modulation signal, u_{pwm} , or an equivalent signal, which sets the 'on-time' of the inverter switches. So, an arc length controller, directly based on the model of the process and the input and outputs, could be implemented as shown in Figure 5.1.(A). l_{ar} is the arc length reference, and the task of the controller is to move the real arc length, l_a , towards the reference. Notice, that the arc length is not measured directly in the system. Instead, it must be derived from the two outputs, that is, U_{tm} and I_{wm} .

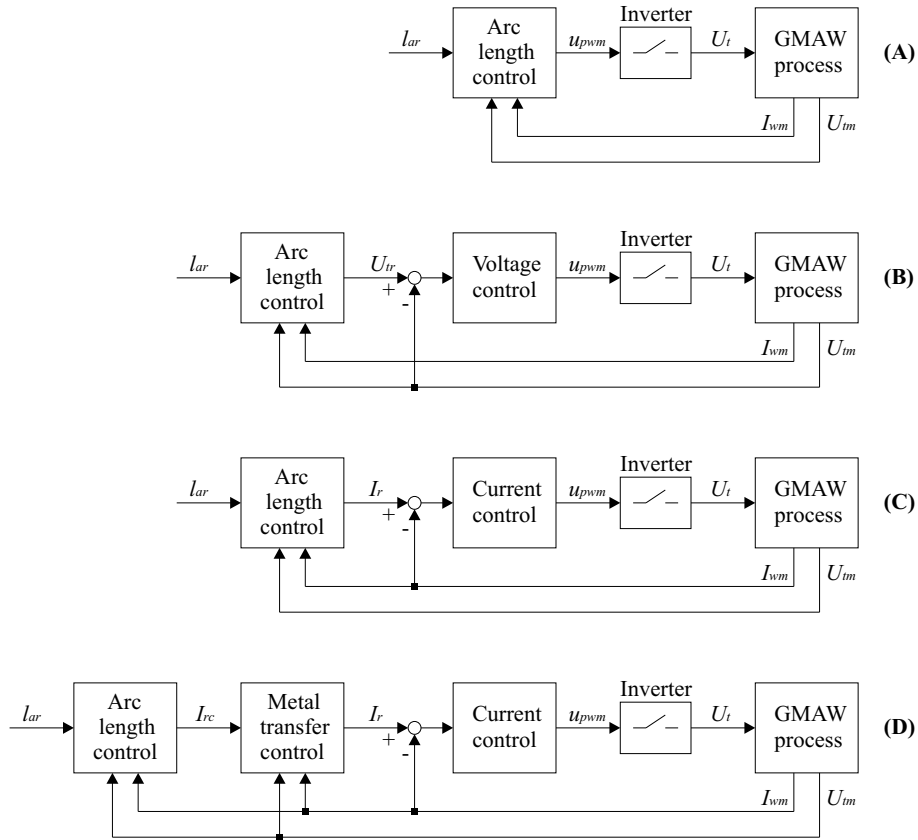


Figure 5.1: Different configurations for GMAW control.

The inverter, however, is in general not linear, and therefore, an inner voltage controller could be included in the system, such that, the arc length controller

interfaces a controlled voltage source. Thus, the controller outputs a terminal voltage reference, U_{tr} . This is shown in Figure 5.1.(B).

It is difficult, if not impossible, to avoid short circuits during welding, and when a short circuit occurs, the welding machine must be able to handle the effect of the short circuit. The effect is a rapid rise in current, which uncontrolled would ruin the weld. In old type transformer welding machines, a large coil in the welding machine limits the rate of which the current is able to rise. However, such large coil is not present in modern inverter based welding machines, as the current can be controlled by software. In the system shown in Figure 5.1.(B), the current is not controlled, but rather the voltage is controlled by the inner voltage controller. However, instead of using an inner voltage controller, an inner current controller can be used. Such system is shown in Figure 5.1.(C). Now, the arc length controller outputs a reference current, I_r , to the inner control.

Compared to the system in (B), it can be argued that the system in (C) has a number of advantages. The first advantage concerns the short circuits. A short circuit can more easily be handled, as the current can be shaped by shaping the current reference signal, I_r . The second advantage concerns robustness. In general, it is very difficult to develop a precise model describing the current dynamics in the welding process, as the current dynamics depends on the wires used. For example, in one particular welding setup, 10 meters of electrical wire could be used, and, in another welding setup, 20 meters of electrical wire. An arc length controller, for which an inner voltage controller is used, must rely on the imprecise model of the current dynamics. However, if an inner current controller is used, the arc length controller does not need to be based on the current dynamics of the process, but rather on the current dynamics of the closed loop including the current controller. The third advantage concerns metal transfer. Metal transfer refers to the process of drop detachment and transfer to the weld pool. In pulsed GMAW, it is the current pulses which cause drop detachment, and thus, it must be possible to control the current. A configuration including metal transfer control is shown in Figure 5.1.(D). Now, the arc length controller outputs some control variable I_{rc} , which is used as input to the metal transfer controller. Notice, that the control variable, I_{rc} , does not have to be a reference current, as indicated by the symbol.

The configuration in Figure 5.1.(C) can be redrawn in a more general way, as shown in Figure 5.2. In this figure, the inverter is left out, and it will not be

considered further in this thesis. Also, the sum symbols have been removed to make the system more general, and moreover, it is assumed, that arc length can be measured in the process. This means, that, an arc length estimator must be part of the process. In the same way, Figure 5.1.(D) can be redrawn as shown in Figure 5.3.

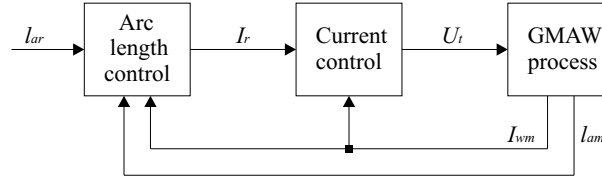


Figure 5.2: The welding current is controlled by the inner current controller. The arc length is controlled by adjusting the current reference signal, I_r .

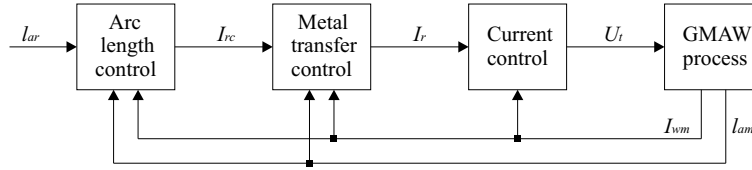


Figure 5.3: The welding current is controlled by the inner current controller. The arc length is controlled by adjusting the signal I_{rc} . The metal transfer controller handles drop detachment.

The two figures, that is, Figure 5.2 and Figure 5.3, can be regarded as general control configurations for, respectively, ordinary GMAW and pulsed GMAW, when using an inner current controller. These general control configurations will be used as frameworks when developing an arc length controller and a metal transfer controller in Chapter 6 and in Chapter 7. However, before starting developing those controllers, metal transfer control and arc length control will be discussed in the following two sections, that is, Section 5.2.1 and Section 5.2.2. Moreover, in Section 5.2.3, supervision in GMAW will be discussed.

5.2.1 Metal Transfer Control

The task for a metal transfer control algorithm is to control the drop detachment process. Basically, the metal transfer controller forces current pulses onto the

process, using either a fixed or a variable pulse frequency. The pulses generated by the metal transfer controller can have different shapes. For example, in Figure 5.4, the welding current is sketched for some chosen pulse shape. This particular pulse shape, is, in this thesis, denoted as the 'chair shape'. Using such a pulse shape, the drop is supposed to detach around the transient phase between the high current level and the low current level. Normally, to achieve this goal, the shape of the current in the pulse period is adjusted off-line. For example, the level of the high current pulse can be increased or decreased, or the time period of that pulse can be increased or decreased. The off-line adjustments must be performed for all different kinds of wire materials, wires diameters, and so on. Thus, this results in a series of welding programs to be developed.

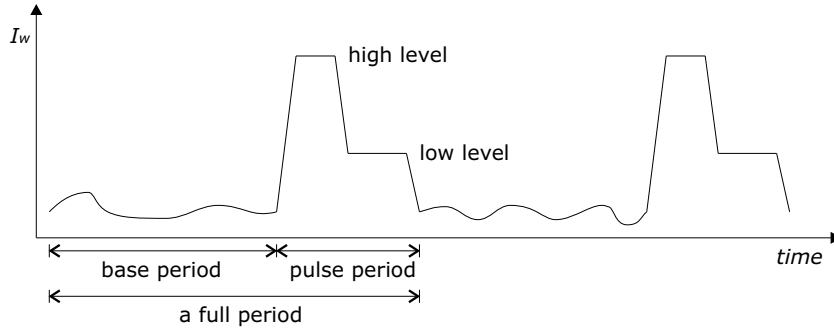


Figure 5.4: A full period is divided into a base period and a pulse period. The pulse is 'chair shaped'.

One disadvantage of using an off-line adjusted current shape in the pulse period is the handling of disturbances and perturbations. For example, a perturbation arises, when a slightly different wire material, than adjusted for, is used in the welding process. Disturbances could be variations in the length between the contact tube and the workpiece, l_c . If disturbances and perturbations are not taken into account when adjusting the pulse shape, one drop might not be detached for every pulse. To introduce robustness, and thus, to ensure drop detachment at every pulse, the pulse current needs to be increased somewhat. This means that the pulse current needs to be somewhat stronger than required for detaching the average drop (average characteristics). However, this gives another problem, as the drop might not detach at the desired location on the pulse shape.

Instead of using only an off-line adjustment approach, it might be possible to

introduce some on-line adjustment or adaptation into the metal transfer control algorithm. However, such approach will not be investigated in this thesis, as it seems to be rather difficult to derive an optimal pulse shape based on knowledge of the process. Instead, in this thesis, the effect on disturbances is dampened by ensuring a uniform drop size prior to the initiation of a pulse. This approach is described in Chapter 7.

No matter which kind of metal transfer control that is used, some overall configuration needs to be considered. The inputs and outputs need to be determined, and moreover, the scheduling of pulse periods need to be considered, or equivalently, deciding on which kind of events that initiates a pulse period. A fast inner current controller needs a current reference, I_r , as input, and thus, the output from the metal transfer control must be such a reference signal. According to Figure 5.3, the input to the metal transfer algorithm is the output from the arc length controller. However, as the arc length controller is not directly connected to the inner current controller, this signal does not necessarily have to represent a current. Instead, for example, it could be an event signal, telling the metal transfer controller when to initiate a pulse period. In this way, a varying control effort from the arc length controller gives a varying pulse frequency. Traditionally, in pulsed GMAW, a constant pulse frequency is used during the welding process. Using such approach, the input to the metal transfer controller could be a signal representing the reference current. Then, in the base period, see Figure 5.4, the metal transfer algorithm must forward the input I_{rc} to the output I_r .

5.2.2 Arc Length Control

The purpose of the arc length controller is to stabilize the process by maintaining a steady arc length. During one period the arc length changes according to drop growth and drop detachment, and therefore, more precisely, the purpose of the arc length controller is to keep a steady arc length averaged over one full period (the base period plus the pulse period).

As shown in Figure 5.2 arc length control for ordinary GMAW can be achieved by controlling the reference current, I_r , based on the available measurements. In Figure 5.3, however, the control signal, I_{rc} , is fed to the metal transfer controller. Traditionally, to ensure arc length control, the arc length control signal is forwarded to the current reference in the base period. In this way, arc length control is carried out in the base period, and drop detachment is carried out in the pulse

period. However, as explained in Chapter 7 this scheme does not have to be used for providing arc length control.

As stated in the former section, the output signal does not have to represent a reference current. However, it is advantageous to use such output signal, as for such signal, it is possible to use the same arc length controller for both pulsed GMAW and ordinary GMAW. Therefore, the arc length controller, presented in Chapter 6, uses an output signal representing the reference current.

5.2.3 Supervision Layer

In this section supervision in GMAW will be discussed. Supervision refers to a number of algorithms, which obtain measurements from both the welding process and the control algorithms. Based on the those measurements, it is possible for the supervision algorithms to interact with the control system. With respect to the software architecture of the total control system, the collection of all supervision algorithms can be grouped into a supervision layer. This layer, and the interactions with the system, are illustrated in Figure 5.5.

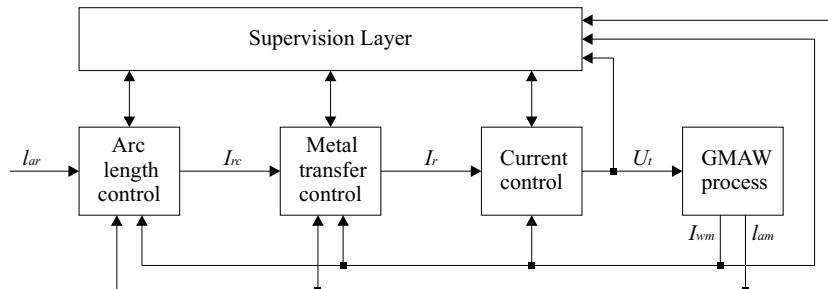


Figure 5.5: The supervision layer observes the total system by available measurements, and interacts if needed.

In general, the supervision layer could include many different tasks. However, here, only two will be discussed. These tasks are listed below.

- Short circuit detection and handling.
- Drop detachment detection.

The supervision layer needs to handle short circuits. If a short circuit occurs, the tip of the electrode must be moved away from the workpiece, and the arc must be reignited to avoid a complete stop of the welding process. This can be handled by increasing the current in a controlled way. So, first, the supervision layer must be able to recognize that a short circuit has occurred, and afterwards, the supervision layer must seize control of arc length reference signal, I_r , to remedy the effect of the short circuit. The recognition is based on the measurements obtained from the process.

Information about drop detachments can be used by the metal transfer controller, and this is why drop detachment detection is mentioned here. Without considering the exact use of information about drop detachments, one can easily be convinced that such information is useful for the metal transfer controller. For example, during welding, it can be tested whether the one drop per pulse (ODPP) objective is fulfilled, and if it is not, the pulse current can be increased. Unlike short circuit detection, it is not trivial to detect drop detachments, when only measuring the terminal voltage and the current in the process. In this thesis, however, drop detachment detection will not be investigated. Instead, it will be left for future work.

5.3 Discussion and Conclusion

In this chapter four specific objectives are derived. These concern minimal energy, minimal arc length, avoiding short circuits, and one drop per pulse (ODPP). Moreover, different control configurations are discussed. This is done under the constraint that the terminal voltage, U_t , is used as an input to the process, and moreover, the measured terminal voltage, U_{tm} , and the measured welding current, I_{wm} , are used as outputs. In particular one configuration seems to be a good choice. In this configuration the process and the inverter are controlled by an inner current controller. This configuration is desirable for several reasons. One reason is that the inner current controller is able to linearize the inverter, and also, the current dynamics become less dependent on uncertain terms in the model. Moreover, an inner current controller provides a direct interface for the metal transfer controller to adjust the current to provide drop detachment.

Metal transfer control, arc length control, and supervision are discussed. Basically, the task of the metal transfer controller is to provide drop detachments, and

in pulsed GMAW this is done by forcing current pulses into the process. However, the shape of the pulses and the pulse frequency must be determined based on the four specific objectives. The arc length controller must be able to keep a steady arc length, and again, the four objectives must be taken into account. Supervision is also considered, even though it is not a topic of this thesis. It is stated that short circuit detection and handling (remedy) is a necessary mechanism, or at least, it is a necessary mechanism in modern inverter based welding machines due to the low output inductance. Also, it is mentioned that it could be advantageous to have a drop detachment detection mechanism included in the supervision layer.

In the following chapters arc length control, metal transfer control, and arc length minimization will be considered. However, the inner current controller will be left out as it will be assumed that this is a traditional PI-controller.

Nonlinear Arc Length Control

6

In this chapter a nonlinear feedback linearization based controller is developed for controlling the arc length. Uncertainties and performance are considered, and the controller is tested in a simulation program.

6.1 Arc Length Control

In Chapter 5 it is stated that arc length control is an important part of the total control GMAW control system, and thus, arc length control will be addressed in this chapter. In Figure 5.2, the overall GMAW control configuration without the metal transfer controller is shown. This configuration will be used for the arc length controller presented in this chapter. Thus, as the metal transfer controller is not included in the configuration, pulsed GMAW will not be considered directly. In fact, the drop will not be considered as a part of the arc length process which should be controlled. So, basically, it is assumed that metal continuously is removed from the electrode during welding. The metal is removed with a melting rate which depends on the control effort, and thus, for controlling the arc length the electrode melting rate must be controlled. The melting rate constitutes a nonlinear process, and therefore, an arc length controller able to handle such nonlinearities will be developed.

Arc length control can be performed by a PI controller, which does, however, have the disadvantage that it is not able to cope with the nonlinearities. In [1] and in [20] the GMAW process is considered as a MIMO system, and nonlinearities are cancelled using an additional feedback signal for each control input. Same approach is used in [13], but in this work sliding mode control is applied for the purpose of robustness. However, in most welding machines used for manual welding only the machine output voltage can be used for controlling the process. Thus, the MIMO approach of [1], [20] and [13] is less suitable for manual weld-

ing. In [54] arc length control is also addressed in a control scheme specialized for pulsed GMAW. However, in this work linear control is used.

In general, linear control methods have the disadvantage that a number of controllers must be tuned to cover a range of operating points, and also, some sort of gain scheduling must be implemented. This is not the case for the controller developed in this chapter. In this chapter a feedback linearization based arc length controller is developed. This nonlinear control method has the advantage that linear system theory can be applied when considering stabilization and performance, as nonlinearities are compensated for. Moreover, as stated before, only one controller for all operating points needs to be designed and tuned.

In Section 6.2 a model describing the arc length process will be presented, and in Section 6.3 the model used for developing the structure of the nonlinear controller. In Section 6.4 stabilization and control will be considered, and uncertainties will be considered in Section 6.5. Performance of the closed loop system is considered in Section 6.6, and the developed controller is tested in a simulation program. In Section 6.7 the arc length reference signal is considered to account for drop detachments, and Section 6.8 is the conclusion of the chapter.

6.2 Dynamic Arc Length Model

Controlling the arc length using feedback linearization requires an arc length model. Therefore, such a model will be developed in this section. In Chapter 3, different parts of the GMAW process already have been modelled, and therefore, the model derived in this section will be based on Chapter 3.

The GMAW process constitutes an electrical circuit. This circuit is modelled in Section 3.2, and also, restated below in equation (6.1) where the function $h(I, l_a)$ is an expression for the arc voltage. The function $h(I, l_a)$ indicates, as described in Section 3.3, that some relation between the arc voltage and the arc length exists.

$$U_t = R_w I + L_w \dot{I} + R_{cc} I + l_s \rho_r I + h(I, l_a) \quad (6.1)$$

U_t is the machine terminal voltage, R_w is wire resistance, L_w is wire inductance, R_{cc} is the sum of all contact resistances, l_s is the electrode length, ρ_r is the electrode resistivity, and I is the welding current.

The arc length, l_a , changes with the electrode speed, v_e , the melting speed, v_m , and moreover, movement of the welding pistol, where the latter means the change in the contact tip to workpiece distance, l_c . However, for now, let us assume that l_c is a constant, or at least that changes in l_c are slow compared to the electrode speed and the melting speed. Using the steady state melting rate model, described in Section 3.6, an expression for the change of arc length is reached. This expression is stated below, in equation (6.3), and notice, that the melting rate is described as a melting speed. Therefore, constants k_1 and k_2 are used instead of c_1 and c_2 .

$$v_m = k_1 I + k_2 I^2 (l_c - l_a) \quad (6.2)$$

and then

$$\dot{l}_a = v_m - v_e = k_1 I + k_2 I^2 (l_c - l_a) - v_e \quad (6.3)$$

Now, we have two equations. One equation, equation (6.3), describing the arc length dynamics as a function of some parameters, the welding current, the contact tip to workpiece distance, the arc length, and the electrode speed. In this equation the current, I , and the arc length, l_a , can be regarded as variables or states, while the contact tip to workpiece distance, l_c , and the electrode speed can be regarded as parameters. The other equation, equation (6.1), describes the dynamics of the current in the process, having having a control voltage U_c as input signal, where U_c almost equals the terminal voltage U_t . Thus, the arc length might be controlled using this control signal. However, the arc length process also includes the inner current control loop, described in Chapter 5, and in fact, this inner current control loop determines the current dynamics. Therefore, another expression than equation (6.1), describing the current dynamics, must be used. The expression used in this work, is a first order transfer function approximating all current dynamics. As input to this transfer function, a current reference signal, I_r , is used as shown in Figure 5.2. Now, the following expression for the current dynamics is obtained.

$$\begin{aligned} I &= \frac{1}{s\tau_i + 1} I_r \Rightarrow \\ \dot{I} &= -\frac{1}{\tau_i} I + \frac{1}{\tau_i} I_r \end{aligned} \quad (6.4)$$

As it can be seen from the transfer function, the steady state gain is one, and the dynamics is characterized by the time constant τ_i . Now, let us use equation (6.4) and (6.3) for setting up a state space description of the arc length system. First, let us introduce the following definitions.

$$x_1 = I \quad (6.5)$$

$$x_2 = l_a \quad (6.6)$$

$$u = I_r \quad (6.7)$$

$$y = l_a \quad (6.8)$$

The nonlinear dynamic system is given by

$$\dot{x} = f(x) + g(x)u \quad (6.9)$$

$$y = h(x) \quad (6.10)$$

where

$$f(x) = \begin{bmatrix} f_1(x) \\ f_2(x) \end{bmatrix} = \begin{bmatrix} -\frac{1}{\tau_i}x_1 \\ k_1x_1 + k_2x_1^2(l_c - x_2) - v_e \end{bmatrix} \quad (6.11)$$

$$g(x) = \begin{bmatrix} g_1(x) \\ g_2(x) \end{bmatrix} = \begin{bmatrix} \frac{1}{\tau_i} \\ 0 \end{bmatrix} \quad (6.12)$$

$$h(x) = x_2 \quad (6.13)$$

Now, a nonlinear model describing the arc length dynamics has been developed. As a remark to this model, the arc length dynamics is determined by a steady state melting rate model and an approximation of the current dynamics. Building on a steady state model constitutes a problem if the bandwidth of the controlled system is as high as the bandwidth of the melting rate. Thus, when tuning the nonlinear controller, it must be required that the closed loop bandwidth is somewhat less than the melting rate bandwidth. Moreover, the first order approximation for the current dynamics might be too crude. Though, from knowledge of physical welding machines and the GMAW process in general, it is believed that a first order approximation is sufficient.

6.3 Feedback Linearization

The idea in feedback linearization is to use some transformation, $z = T(x)$, and apply some feedback control law, u , that transforms the nonlinear system into a linear system. Then, having obtained a linear system, usual linear control design methods can be applied for stabilization.

In [19, Chapter 13] one can find a definition of feedback linearizable systems. This definition is restated in the following.

A nonlinear system

$$\dot{x} = f(x) + G(x)u \quad (6.14)$$

where $f : D \rightarrow R^n$ and $G : D \rightarrow R^{n \times p}$ are sufficiently smooth on a domain $D \subset R^n$, is said to be feedback linearizable (or input-state linearizable) if there exists a diffeomorphism $T : D \rightarrow R^n$ such that $D_z = T(D)$ contains the origin and the change of variables $z = T(x)$ transforms the system, $\dot{x} = f(x) + G(x)u$, into the form

$$\dot{z} = Az + B\gamma(x)[u - \alpha(x)] \quad (6.15)$$

with (A, B) controllable and $\gamma(x)$ nonsingular for all $x \in D$.

Thus, if a nonlinear system, on the form given in equation (6.14), is feedback linearizable, it is possible to transform the original nonlinear system into a system, on a form, given in equation (6.15). Note, that the nonlinear model developed in Section 6.2 has a structure similar to the structure given in equation (6.14). The advantage of the representation in (6.15) is the ability to choose a feedback control law that cancels out the nonlinearities of the system. That is, the control law stated in the following.

$$u = \alpha(x) + \beta(x)\nu, \quad \beta(x) = \frac{1}{\gamma(x)} \quad (6.16)$$

Inserting this control law into equation (6.15) gives a linear system controlled by input ν .

$$\dot{z} = Az + B\nu \quad (6.17)$$

In general, it is not trivial, or if possible at all, to find a transform, $T(x)$, that transforms the nonlinear system into the form given in equation (6.15). However, for some nonlinear systems this transform is quite simple, and in fact, for the dynamic arc length model, developed in Section 6.2, it is possible to use a standard procedure. In the following short overview of the input-output linearization procedure, found in [28, Chapter 13], is presented.

1. The relative degree, ρ , of the system is calculated. A relative degree equal to the order of the system means that the system is fully feedback linearizable. Otherwise, only a part of the system is feedback linearizable, and part is left as internal dynamics, also referred to as the zero-dynamics.
2. The functions $\gamma(x)$ and $\alpha(x)$ are calculated.
3. A transform $z = T(x)$ is found.
4. The original system is reformulated in the, so called, normal form. In this form the linear part of the system is given in a specific form (A_c, B_c, C_c) . The matrices (A_c, B_c) are in control canonical form.

Referring to the dynamic arc length model stated in equation (6.9) and (6.10), the relative degree can be calculated. The relative degree, ρ , equals the number of derivatives of $h(x)$ before dependence on the input is obtained.

$$h(x) = x_2 \quad (6.18)$$

$$\dot{h}(x) = \dot{x}_2, \text{ Not dependent on the input.} \quad (6.19)$$

$$\ddot{h}(x) = \ddot{x}_2, \text{ Depends on } \dot{x}_1 \text{ which depends on the input.} \quad (6.20)$$

Thus, this means that the relative degree is equal to 2, and moreover, as there are two states in the system, the system is fully feedback linearizable.

Next, we need to calculate the functions $\gamma(x)$ and $\alpha(x)$. These functions are given by

$$\gamma(x) = L_g L_f^{\rho-1} h(x) \quad (6.21)$$

$$\alpha(x) = -\frac{1}{\gamma(x)} L_f^\rho h(x) \quad (6.22)$$

where ρ is the relative degree. L_f and L_g are lie derivatives with respect to $f(x)$ and $g(x)$, respectively. For example, $L_f h(x) = (\partial h(x)/\partial x)f(x)$. Thus, using $\rho = 2$ and the model developed in Section 6.2, the functions $\gamma(x)$ and $\alpha(x)$ are given by

$$\gamma(x) = (k_1 + 2k_2 x_1(l_c x_2)) \frac{1}{\tau_i} \quad (6.23)$$

$$\alpha(x) = -\frac{1}{\gamma(x)} (\gamma(x)\tau_i f_1 - k_2 x_2 f_2) \quad (6.24)$$

Next, the transformation, $z = T(x)$, is given by the output equation, $h(x)$, and its first derivative.

$$z = \begin{bmatrix} z_1 \\ z_2 \end{bmatrix} = \begin{bmatrix} T_1(x) \\ T_2(x) \end{bmatrix} = \begin{bmatrix} h(x) \\ L_f h(x) \end{bmatrix} = \begin{bmatrix} x_2 \\ f_2(x) \end{bmatrix} \quad (6.25)$$

Now, having calculated the functions $\gamma(x)$ and $\alpha(x)$, and moreover, introduced the transformation above, the transformed system is given by

$$\dot{z} = A_c z + B_c \gamma(x)[u - \alpha(x)] \quad (6.26)$$

$$y = C_c z \quad (6.27)$$

The matrices A_c , B_c and C_c are on the following form

$$A_c = \begin{bmatrix} 0 & 1 \\ 0 & 0 \end{bmatrix}, \quad B_c = \begin{bmatrix} 0 \\ 1 \end{bmatrix}, \quad C_c = [1 \quad 0] \quad (6.28)$$

So, the original nonlinear arc length model, developed in Section 6.2, has been transformed into the, so called, normal form given by equation (6.26) and equation (6.27). In this representation the first state, z_1 , constitutes the output, $h(x)$, which in this case is the arc length, l_a . The second state, z_2 , is the derivative of the output, thus, the derivative of the arc length or change in arc length with respect to time, \dot{l}_a .

6.4 Control and Tracking

In this section control and tracking are considered. The objective is to control the arc length. This means, that the arc length controller must be able to drive the arc length, $l_a = x_2$, towards some reference arc length, $l_{ar} = r$. This raises some issues concerning stabilization and performance. However, only structural properties of the controller will be addressed in this section. This means, that it will be considered how it is possible to stabilize the system, but tuning issues will not be considered. Eliminating steady state errors requires some integral control which introduces additional dynamics to the system, and therefore, as additional dynamics extends the system it will be considered in this section. Later, in Section 6.6, tuning issues will be considered.

The dynamic system to be controlled is stated by equation (6.26) and equation (6.27) where, respectively, γ and α are given by equation (6.23) and equation (6.24). Now, the idea is to develop a state feedback controller that is able to drive the two states towards some setting. The first state, z_1 , is the arc length which must be driven towards some reference, r , and, as the second state, z_2 , equals the derivative of the first state, then z_2 must be driven towards the derivative of the reference. Therefore, the error dynamics must be considered. First, let us define the error, e , and furthermore, obtaining an expression for the derivative of the error.

$$e = R - z, \quad R = \begin{bmatrix} r \\ \dot{r} \end{bmatrix} \quad (6.29)$$

$$\dot{e} = \dot{R} - \dot{z}, \quad \dot{R} = \begin{bmatrix} \dot{r} \\ \ddot{r} \end{bmatrix} \quad (6.30)$$

Now, using equation (6.26) describing the system dynamics, the error dynamics can be derived.

$$\begin{aligned} \dot{e} &= -A_c(R - e) - B_c\gamma(x)[u - \alpha(x)] + \dot{R} \\ &\Rightarrow \\ \dot{e} &= A_c e - B_c\gamma(x)[u - \alpha(x)] + B_c\ddot{r} \end{aligned} \quad (6.31)$$

The error dynamics can be feedback linearized by using a control law, as shown in equation (6.16), that cancels the nonlinear terms and leaves a linear part that can be stabilized by the state feedback $K_e e$. The control law is given by

$$u = \alpha(x) + \beta(x)[K_c e + \ddot{r}] , \quad \beta(x) = \frac{1}{\gamma(x)} \quad (6.32)$$

where

$$K_c = [k_{c1} \quad k_{c2}] \quad (6.33)$$

If the control law, equation (6.32), is inserted in the error dynamics the following result is obtained.

$$\dot{e} = (A_c - B_c K_c)e \quad (6.34)$$

So, using equation (6.32) for the control law, the error dynamics becomes linear, and moreover, is stable if the matrix $(A_c - B_c K_c)$ is stable (Hurwitz). This means, that the real part of the eigenvalues of this particular matrix must be negative, and as A_c and B_c are given, it becomes a matter of choosing a vector K_c that satisfy the stability property. In Figure 6.1 the arc length controller is shown. Both the first and the second derivative of the reference, r , are used in the control law (equation (6.32)). Such signals can be obtained from a second order transfer function, filtering an original reference signal, l_{ar} , as shown in the figure.

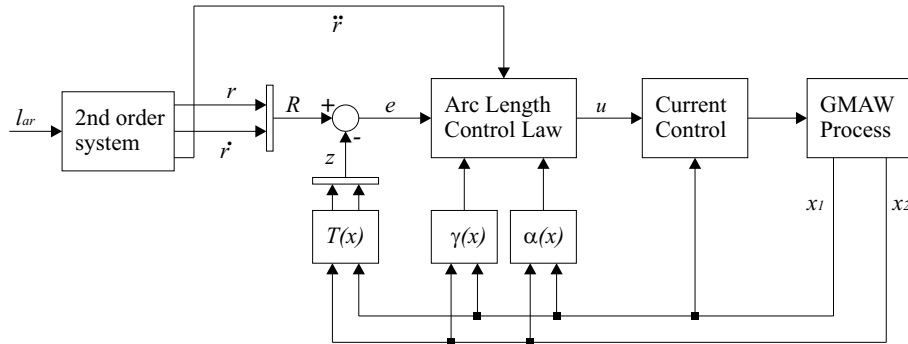


Figure 6.1: The structure of the arc length controller.

In GMAW it is important to keep the arc length at some desired set point regardless of the disturbances, the uncertainties and the noise present. Thus, it is common to include some kind of integrator in the arc length controller. Therefore,

in the following, an integrator will be added to control law presented in equation (6.32). First, let us introduce the variable σ that is the integral of the arc length error, e_1 .

$$\dot{\sigma} = e_1 \quad (6.35)$$

This dynamics can be added to the dynamics describing the arc length. Thus, an augmented system is obtained. First, let us define a new state vector, ψ .

$$\psi = \begin{bmatrix} e_1 \\ e_2 \\ \sigma \end{bmatrix} \quad (6.36)$$

Now, the augmented system is given by

$$\dot{\psi} = A_a \psi - B_a \gamma(x)[u - \alpha(x)] + B_a \ddot{r} \quad (6.37)$$

where

$$A_a = \begin{bmatrix} 0 & 1 & 0 \\ 0 & 0 & 0 \\ 1 & 0 & 0 \end{bmatrix}, \quad B_a = \begin{bmatrix} 0 \\ 1 \\ 0 \end{bmatrix}, \quad C_a = [1 \quad 0 \quad 0] \quad (6.38)$$

Again, a control law can be found which linearizes the system.

$$u = \alpha(x) + \beta(x)[K_a \psi + \ddot{r}], \quad \beta(x) = \frac{1}{\gamma(x)} \quad (6.39)$$

where

$$K_a = [k_{a1} \quad k_{a2} \quad k_{a3}] \quad (6.40)$$

The following closed loop dynamics is obtained.

$$\dot{\psi} = (A_a - B_a K_a) \psi \quad (6.41)$$

Like before, the matrix $(A_a - B_a K_a)$ must be stable for the ψ -dynamics to be stable, and this is a matter of choosing the vector K_a .

In Figure 6.2 the effect of having included integral control is illustrated. The arc length reference is set to 3 mm. In simulation, a 5% gain error is applied to the current sensor at time $t = 0.5$ s. For the control law with no integrator included, the result is an offset in the arc length. However, if the integrator is included, the arc length approach the reference arc length after the error has occurred.

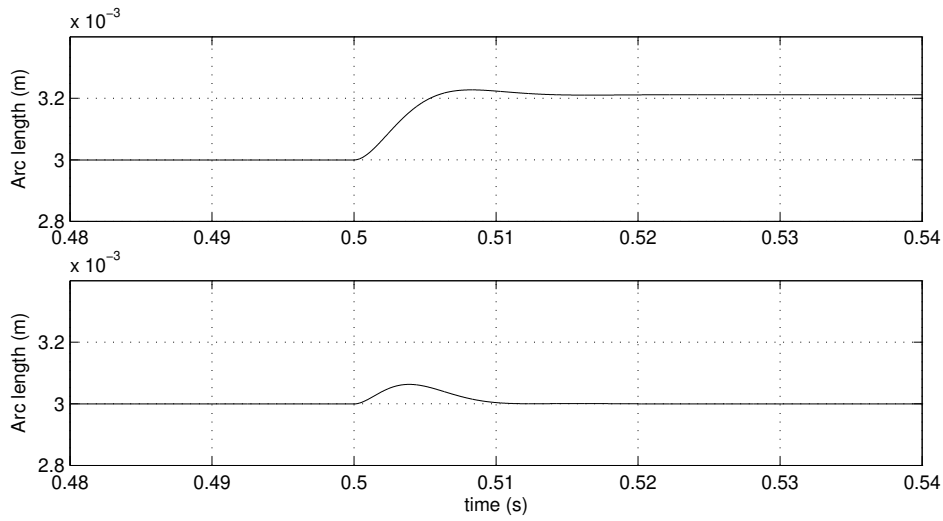


Figure 6.2: First plot: Control law with no integrator included. Second plot: Control law with integral control.

The control laws, equation (6.32) and equation (6.39), are state feedback control laws. Thus, it is assumed that both states, $z_1 = T_1(x)$ and $z_2 = T_2(x)$, in the system can be measured. Both states, z_1 and z_2 , depends on the states x_1 and x_2 , that is, the current and the arc length. The current is measured directly in the system by a current sensor (hall element), but the arc length is not measured directly. The only measurements available are the current and the voltage at the welding machine terminals (welding machine output). Again, let us denote that voltage by U_t . Instead of direct measurement, the arc length can be estimated using some arc length model, $U_a = h(I, l_a)$. Here, a linear arc length model as stated below is used.

$$U_a = U_0 + R_a I + E_a l_a \quad (6.42)$$

U_a is the arc voltage which cannot be measured in a practical welding system. Instead, the terminal voltage is measured. This voltage includes voltage drops over the wires, the contact points, the electrode, and the arc. Let us, due to the fast dynamics, ignore wire inductance and only consider the resistance in the loop, then U_t can be expressed as

$$U_t = R_1 I + U_a, \quad R_1 = R_w + R_{cc} + \rho_r l_{s0} \quad (6.43)$$

R_w is the wire resistance, R_{cc} is sum of all contact resistances, ρ_r is the resistivity of the electrode material, and the constant l_{s0} is some expected or average length of the electrode. Now, using equation (6.42) and equation (6.43), an arc length estimate can be found.

$$l_a = \frac{U_t - R_1 I - U_0 - R_a I}{E_a} \quad (6.44)$$

In Figure 6.3, the closed loop system is shown. Instead of a direct arc length measurement (requires a camera), the arc length estimator has been included.

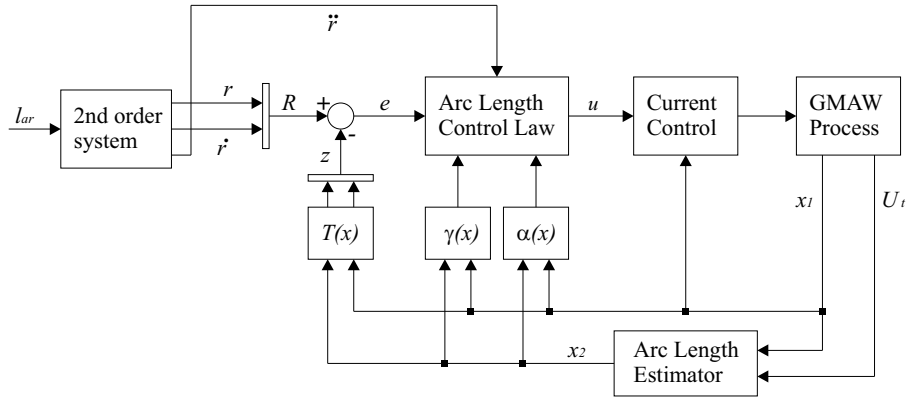


Figure 6.3: The structure of the arc length controller with an arc length estimator included.

6.5 Uncertainty Analysis

In Section 6.4 a nonlinear control law was developed. This control law was based on a model describing the arc length dynamics, and it was assumed that the model constituted a precise description of the system. However, for the welding process, like any practical systems, the model is just an approximation of the real system. The model describing the arc length dynamics can be characterized as a lumped model, describing only the most significant dynamics, and moreover, some degree of uncertainty can be identified for the variables and parameters included. For example, the melting speed parameters k_1 and k_2 are included in the model. These parameters can be found experimentally for different types of electrodes, but even then, discrepancies, probably, will exist. For example, slight differences in the electrode material will give discrepancies in k_1 and k_2 . In fact, all variables and parameters in the models have some degree of uncertainty.

As variable and parameters are uncertain, it is important to have a control law able to cope with such uncertainty. Therefore, in the following, system stabilization in the presence of uncertainty is considered.

6.5.1 Stabilization under uncertainties

Equation (6.32) and equation (6.39) are the derived control laws, controlling the arc length dynamics. The difference between these control laws are the integrator included in the second control law, equation (6.39). In this section, for simplicity, only the first control law is considered, that is, equation (6.32).

The model describing the arc length dynamics is given by equation (6.9) and equation (6.10). In Section 6.3, this model is transformed into a system on the normal form using the functions $\alpha(x)$ and $\gamma(x)$. In Section 6.4, a model describing the error dynamics is presented in equation (6.31). Also, this model is expressed by the functions $\alpha(x)$ and $\gamma(x)$. $\alpha(x)$ and $\gamma(x)$ are functions expressed by variables and parameters of the system, and as these are uncertain, the functions $\alpha(x)$ and $\gamma(x)$ also become uncertain. Also, the transformation, $T(x)$, that transforms the original model, equation (6.9) and equation (6.10), into the normal form is based on variables and parameters, and thus, $T(x)$ becomes uncertain. Now, let us assume that equation (6.31) is the correct physical model for the error dynamics, but because of uncertainty, a control law based on $\hat{\alpha}(x)$, $\hat{\gamma}(x)$ and $\hat{T}(x)$ are used. That is

$$u = \hat{\alpha} + \hat{\beta}(K_c \hat{e} + \ddot{r}) \quad (6.45)$$

Notice, that the measurement of the error is uncertain as $T(x)$ is uncertain. Thus, the measurement of the error is written as \hat{e} . To be able to analyze uncertainties in the system the error dynamics is considered. First, let us use the following definitions.

$$\Delta_e = e - \hat{e} \quad (6.46)$$

$$\Delta_\alpha = \alpha - \hat{\alpha} \quad (6.47)$$

$$\Delta_\gamma = \gamma - \hat{\gamma} \quad (6.48)$$

$$\Delta_\beta = \beta - \hat{\beta} \quad (6.49)$$

$$\hat{\beta} = \frac{1}{\hat{\gamma}} \quad (6.50)$$

To calculate the closed loop dynamics, the control law, equation (6.45), is inserted into the error dynamics, equation (6.31).

$$\begin{aligned} \dot{e} &= A_c e - B_c \gamma [\hat{\alpha} + \hat{\beta} K_c \hat{e} + \hat{\beta} \ddot{r} - \alpha - \beta \ddot{r}] \Rightarrow \\ \dot{e} &= A_c e - B_c \gamma [\hat{\alpha} - \alpha + \hat{\beta} K_c \hat{e} + \hat{\beta} \ddot{r} - \beta \ddot{r} + \hat{\beta} K_c e - \hat{\beta} K_c e + \beta K_c e - \beta K_c e] \Rightarrow \\ \dot{e} &= (A_c - B_c K_c) e - B_c \gamma [(\hat{\alpha} - \alpha) + \hat{\beta} K_c (\hat{e} - e) + (\hat{\beta} - \beta) K_c e + (\hat{\beta} - \beta) \ddot{r}] \end{aligned} \quad (6.51)$$

Using equation (6.46), (6.47), (6.48) and (6.49), the closed loop dynamics can be expressed as

$$\dot{e} = (A_c - B_c K_c) e + B_c \delta(e) \quad (6.52)$$

$$\delta(e) = \gamma (\Delta_\alpha + \hat{\beta} K_c \Delta_e + \Delta_\beta K_c e + \Delta_\beta \ddot{r}) \quad (6.53)$$

Now, having found the closed loop dynamics, stabilization can be considered. It is assumed that $\delta(e)$ can be written as

$$\delta(e) = \delta_0 + \delta_k(e) \quad (6.54)$$

δ_0 is a constant, and thus, does not contribute to instability. However, the equilibrium point will be changed. Thus, we want to investigate stability under the uncertainty $\delta_k(e)$.

The uncertainty function $\delta_k(e)$ is an unknown function, in the sense, that no model describing $\delta_k(e)$ can be identified. However, it can be assumed, that some bound on the magnitude of $\delta_k(e)$ exists. For instance, there is limit on parameter discrepancies, measurement errors and so on. Therefore, let us introduce the following limit on the magnitude of $\delta_k(e)$. $k_{\delta 1}$ and $k_{\delta 2}$ are positive constants.

$$|\delta_k(e)| \leq k_{\delta 1}|e_1| + k_{\delta 2}|e_2| \quad (6.55)$$

Now, in the following, a condition for stability based on (6.55) is derived. The stability condition will be based on the Small Gain Theorem.

Small Gain Stability Condition

In this section condition for stability based on the Small Gain Theorem [18, Chapter 9] is presented. The closed loop system stated in (6.52) can be considered as a loop consisting of the of the uncertainty function, $\delta(e)$, and some transfer function. Again, it is assumed, that the uncertainty function, $\delta(e)$, can be split into two terms as stated in (6.54). Only the second term depends on e , and thus, only this term is included in the loop. Also, it is assumed that $\delta_k(e)$ is bounded as described in (6.55).

In the following, the two systems included in the loop are described. The uncertainty function, $\delta_k(e)$, is expressed as a function of the variable ϕ , such that $\phi_1 = k_{\delta 1}e_1$ and $\phi_2 = k_{\delta 2}e_2$.

$$v_1 = \delta_k(\phi) \quad (6.56)$$

$$|\delta_k(\phi)| \leq |\phi_1| + |\phi_2| \quad (6.57)$$

The second component is a transfer function, $M(s)$, representing the closed loop error dynamics and having output ϕ . $M(s)$ is described below in state space form.

$$\dot{e} = (A_c - B_c K_c)e + B_c v_2 \quad (6.58)$$

$$\phi = Ke, \quad K = \begin{bmatrix} k_{\delta 1} & 0 \\ 0 & k_{\delta 2} \end{bmatrix} \quad (6.59)$$

$$v_2 = \delta_0 + v_1 \quad (6.60)$$

Also, in Figure 6.4 the loop consisting of the uncertainty function, $\delta_k(\phi)$, and the transfer function are illustrated. The Small Gain Theorem states that the system, in Figure 6.4, is stable if the maximum and total gain around the loop is less than one. For investigating the total gain, the maximum gain for each component included in the loop must be evaluated.

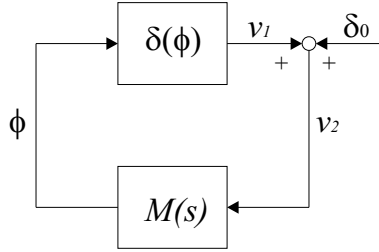


Figure 6.4: The loop describing the error dynamics when uncertainties are taken into account.

The maximum gain for the transfer function, $M(s)$, is given by

$$\|M(s)\|_{\infty} = \theta_M \quad (6.61)$$

For some fixed $|\phi|$ and from (6.57) we have that the maximal gain $|\delta_k(\phi)|$ is obtained for $\phi_1 = \phi_2$. Now, if $|\phi| = 1$ we have that

$$\begin{aligned} |\phi| &= \sqrt{\phi_1^2 + \phi_2^2} = 1 \Rightarrow \\ \phi_1 &= \phi_2 = \frac{1}{\sqrt{2}} \end{aligned} \quad (6.62)$$

So, the maximal gain $|\delta_k(\phi)|$ is given by

$$\max(|\delta_k(\phi)|)_{|\phi|=1} = \frac{1}{\sqrt{2}} + \frac{1}{\sqrt{2}} = \sqrt{2} \quad (6.63)$$

Now, according to the Small Gain Theorem the closed loop system, shown in Figure 6.4, is stable if

$$\theta_M \sqrt{2} < 1 \quad (6.64)$$

So, using this condition, stability can be evaluated for the arc length process, controlled by the arc nonlinear arc length controller, if the constants $k_{\delta 1}$ and $k_{\delta 2}$, using in (6.55), are known. Therefore, to obtain these constants, realistic uncertainties for the process are considered in the following section.

6.5.2 System Uncertainty

In this section, uncertainty in the dynamic arc length model will be analyzed. For the purpose of guaranteeing stability, a condition for stability has been derived based on the assumption, that the uncertainty function $\delta(e)$ can be expressed as a sum of some constant, not depending on the error e , and a term, $\delta_k(e)$, depending on e , that is, equation (6.54). Also, it is assumed that the magnitude $\delta_k(e)$ is bounded as described in (6.55). However, it is not known beforehand how the magnitude of the uncertainty function depends on the conditions of the system, i.e. states and parameters. Though, it can be expected that the uncertainty will be a function of the error, e , and also, be a function of the size of the signals. Therefore, the uncertainty function must be evaluated for different equilibrium points, or operating points, and also for different errors, e . An equilibrium point, being a point where $e = 0$, that is, the arc length error, e_1 , equal to zero, and the derivative of the arc length error, e_2 , equals to zero. Different operating points are obtained from different steady state arc lengths combined with different steady state currents, where different current levels correspond to different electrode speeds.

To investigate all possible perturbations, all possible equilibrium points must be evaluated with respect to uncertainty, and uncertainty must be evaluated for all possible errors with respect to each equilibrium point. Naturally, this is not a practical approach. Instead a set of equilibrium points are chosen, and for each equilibrium point a set of errors is chosen. For each equilibrium point, given by $e = 0$ and $x = \bar{x}$, we seek a function that bounds the uncertainty function $\delta_k(e)$. Using inequality (6.55), we want to formulate an upper bound on $|\delta_k(e)|$, given some equilibrium point, as stated in the following. Index \bar{x} indicates the dependence of the arc length and current steady state settings.

$$|\delta_k(e, \bar{x})| \leq k_{\delta 1 \bar{x}} |e_{1 \bar{x}}| + k_{\delta 2 \bar{x}} |e_{2 \bar{x}}| \quad (6.65)$$

Equilibrium points and error points are chosen, such that, a practical range of different settings are covered. Nine equilibrium points are chosen. These are shown in Figure 6.5.a. Thus, a low, medium and high arc length have been chosen, and for the welding current, a low, medium and high current have been chosen. In Figure 6.5.b, the melting speed, v_e , is shown instead of the current as the melting speed correspond to different set points in the transformed coordinates (z-coordinates). In the z-coordinates the arc length is the first state, z_1 , and the arc length derivative is the second state, z_2 .

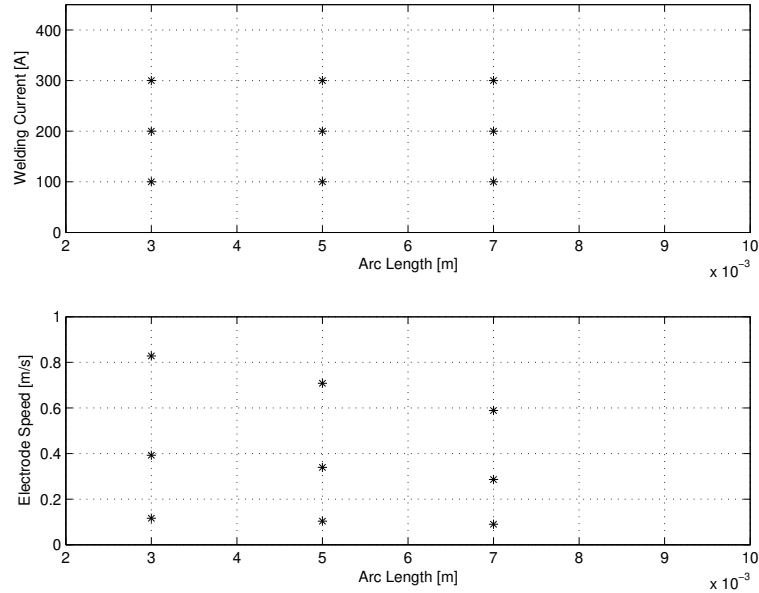


Figure 6.5: Equilibrium points.

For each of the equilibrium points shown in Figure 6.5, the worst possible uncertainty, $\delta(\hat{x})$, must be found. Moreover, for each equilibrium point, the worst possible uncertainties for different errors must be identified. Thus, first, a set of errors must be chosen. Like for the equilibrium points, all possible errors cannot be chosen. Instead a set of errors are chosen that represents different error levels. Furthermore, to identify $k_{\delta 1}$ and $k_{\delta 2}$ in inequality (6.65) let us choose errors such

that either $(e_1 = 0, e_2 \neq 0)$ or $(e_1 \neq 0, e_2 = 0)$. Now, the states, z_1 and z_2 are chosen as shown in the following, and errors can be obtained using equation (6.29).

- 1) $z_1 = z_{1,\min}$, $z_2 = \bar{z}_2 = 0$
- 2) $z_1 = \bar{z}_1 - (\bar{z}_1 - z_{1,\min})p$, $z_2 = \bar{z}_2 = 0$
- 3) $z_1 = \bar{z}_1 + (z_{1,\max} - \bar{z}_1)p$, $z_2 = \bar{z}_2 = 0$
- 4) $z_1 = z_{1,\max}$, $z_2 = \bar{z}_2 = 0$
- 5) $z_1 = \bar{z}_1$, $z_2 = z_{2,\min}$
- 6) $z_1 = \bar{z}_1$, $z_2 = \bar{z}_2 - (\bar{z}_2 - z_{2,\min})p$
- 7) $z_1 = \bar{z}_1$, $z_2 = \bar{z}_2 + (z_{2,\max} - \bar{z}_2)p$
- 8) $z_1 = \bar{z}_1$, $z_2 = z_{2,\max}$

p is some factor depending on the desired error set point between the equilibrium point and, either, the maximum or the minimum value. p is set to 30%, that is, $p = 0.3$. To further illustrate the approach, errors for equilibrium point 1 ($x_2 = 0.003$, $x_1 = 100$) and equilibrium point 5 ($x_2 = 0.005$, $x_1 = 200$) are shown in Figure 6.6.

Now, a set of equilibrium points have been chosen, and moreover, for each equilibrium point a set of errors has been chosen. For each of those 72 points the worst possible perturbation, i.e. uncertainty, for each point must be identified. The model describing the arc length dynamics is given by equation (6.9) and equation (6.10), and using this model, model uncertainty can be identified for different variables and parameters as explained in the following.

Current, x_1 : Using Migatron's Flex 4000 welding machine as an example, a number of uncertainties can be identified with respect to welding current measurements. The total measuring setup consists of an open loop hall element, an analog low pass filter, and an analog to digital converter. The open loop hall device measure the current, and then, outputs a voltage to the analog low pass filter. Afterwards, the filtered signal is sampled by the analog to digital converter. The open loop hall element has a possible gain error on $\pm 1\%$. The analog filter has a possible gain error on $\pm 0.2\%$, and moreover, a possible offset error on ± 1 A. The analog to digital converter has a 12 bit resolution, and uses an interval of 0-1000 A. This equals a resolution on 0.25 A. Thus,

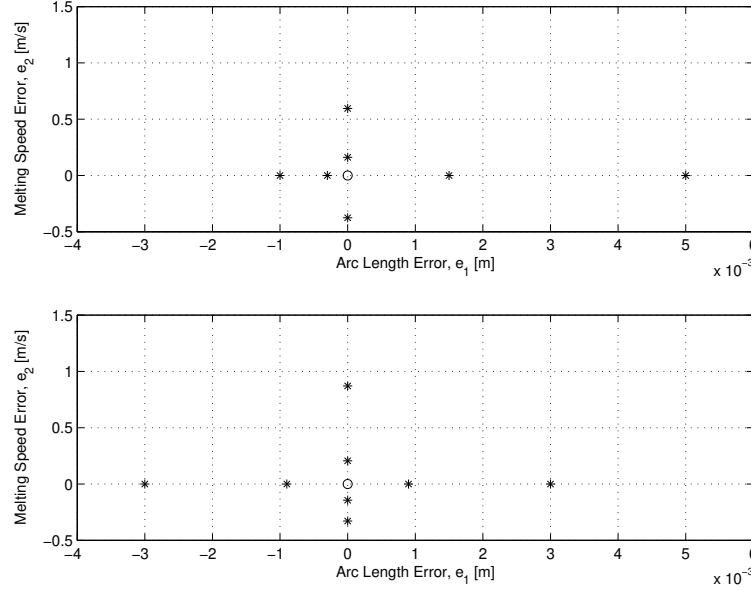


Figure 6.6: a) Errors for equilibrium point one, $x_2 = 0.003$, $x_1 = 100$. b) Errors for equilibrium point five, $x_2 = 0.005$, $x_1 = 200$.

the worst possible positive and negative perturbation can be expressed as

$$\text{positive : } \hat{x}_1 = 1.01 \cdot 1.002 \cdot x_1 + 1 + 0.25 \quad (6.66)$$

$$\text{negative : } \hat{x}_1 = 0.99 \cdot 0.998 \cdot x_1 - 1 - 0.25 \quad (6.67)$$

Arc Length, x_2 : The arc length cannot be measured directly, but only indirectly using current and voltage measurements and an arc length model. The model used is the linear model stated in equation (6.44). Uncertainty can be identified for both the parameters and variables, and also, for the structure of the model. However, let us assume, that all uncertainty can be modelled by a factor $(1 \pm a_{x_2})$, equivalent to some gain error. A 5% gain error is assumed, thus, $a_{x_2} = 0.05$. Positive and negative perturbations are given below.

$$\text{positive : } \hat{x}_2 = (1 + a_{x_2})x_2 \quad (6.68)$$

$$\text{negative : } \hat{x}_2 = (1 - a_{x_2})x_2 \quad (6.69)$$

Contact tip to workpiece distance, l_c : In hand held welding the contact tip to workpiece distance, l_c , is unknown. However, it can be assumed that the

actual distance lies between some boundaries. Say, 15% of the expected value, l_c , then, $a_{lc} = 0.15$. Positive and negative perturbations are given below.

$$\text{positive : } \hat{l}_c = (1 + a_{lc})l_c \quad (6.70)$$

$$\text{negative : } \hat{l}_c = (1 - a_{lc})l_c \quad (6.71)$$

Electrode speed, v_e : Again, let us use Migatron's Flex 4000 welding machine as an example. In this system the resolution in the measuring system results in an uncertainty of around 0.5%. In addition, the quality of the encoder contribute to the uncertainty of the measured electrode speed. So, let us assume a total uncertainty of 1%. Thus, $a_{ve} = 0.01$. Positive and negative perturbations are given below.

$$\text{positive : } \hat{v}_e = (1 + a_{ve})v_e \quad (6.72)$$

$$\text{negative : } \hat{v}_e = (1 - a_{ve})v_e \quad (6.73)$$

Current dynamics, τ_i : It is assumed that all current dynamics can be modelled as a first order low pass filter having a time constant, τ_i . This is only an approximation, and therefore, let us expect some uncertainty on the break point frequency. Say, an uncertainty of 5%, thus, $a_{\tau_i} = 0.05$. Positive and negative perturbations are given below.

$$\text{positive : } \hat{\tau}_i = (1 + a_{\tau_i})\tau_i \quad (6.74)$$

$$\text{negative : } \hat{\tau}_i = (1 - a_{\tau_i})\tau_i \quad (6.75)$$

Melting speed constants, k_1 and k_2 : The melting speed constants can be identified through experiments. However, these constants will vary with electrode discrepancies. For example, uncertainty as a result of electrode contamination. Moreover, k_1 and k_2 and parameters in a steady state melting speed model, and as the melting speed, in fact, is a dynamic process, some uncertainty is introduced. Let us assume an uncertainty of 5%, and thus, $a_{k1} = 0.05$ and $a_{k2} = 0.05$. Positive and negative perturbations are given below.

$$\text{positive : } \hat{k}_1 = (1 + a_{k1})k_1 \quad (6.76)$$

$$\text{positive : } \hat{k}_2 = (1 + a_{k2})k_2 \quad (6.77)$$

$$\text{negative : } \hat{k}_1 = (1 - a_{k1})k_1 \quad (6.78)$$

$$\text{negative : } \hat{k}_2 = (1 - a_{k2})k_2 \quad (6.79)$$

Now, having defined worst case uncertainties, it is possible to calculate the worst case $\delta(e)$, equation (6.53), for all of the 72 different settings. The worst case $\delta(e)$ for each setting is found for all possible combinations of worst case uncertainties for all variables and parameters, that is, x_1 , x_2 , l_c , v_e , τ_i , k_1 and k_2 . Worst case uncertainties for variation in arc length, only, are shown in Figure 6.7. The values are obtained using the parameter settings found in the and Nomenclature, and moreover, controller gains, $k_{c1} = 252650$ and $k_{c2} = 871$ (see equation (6.33)). These state feedback control gains are obtained for a closed loop system having a break point a 80 Hz, see Section 6.6.

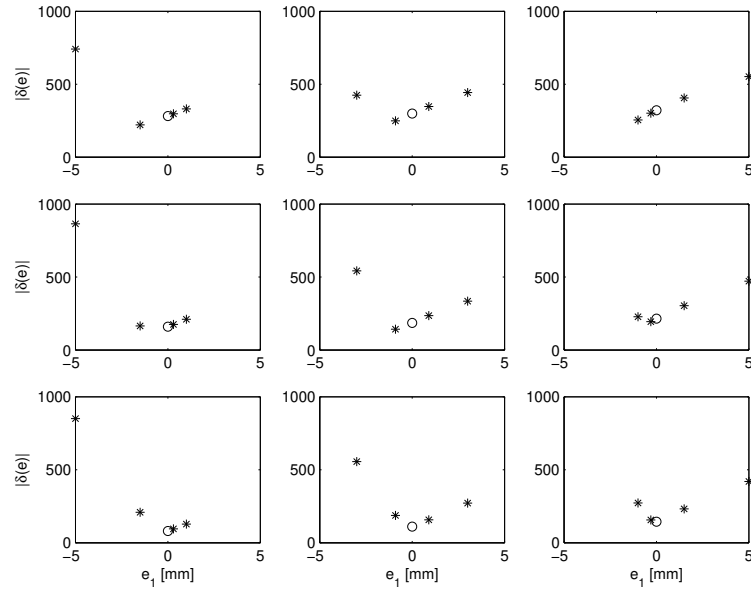


Figure 6.7: Worst case uncertainties for variation in the arc length.

Likewise, worst case uncertainties for variation in e_2 , the derivative of the arc length error, have been calculated. These uncertainties are shown in Figure 6.8.

Looking at the uncertainties shown in Figure 6.7 and in Figure 6.8, it is possible to identify an upper bound, ε , on $\delta(e)$ for each equilibrium points, and also, it is possible to calculate the constants $k_{\delta 1}$ and $k_{\delta 2}$ for each equilibrium point. Estimates, for each equilibrium point, of $k_{\delta 1}$ and $k_{\delta 2}$ are calculated as stated in the following.

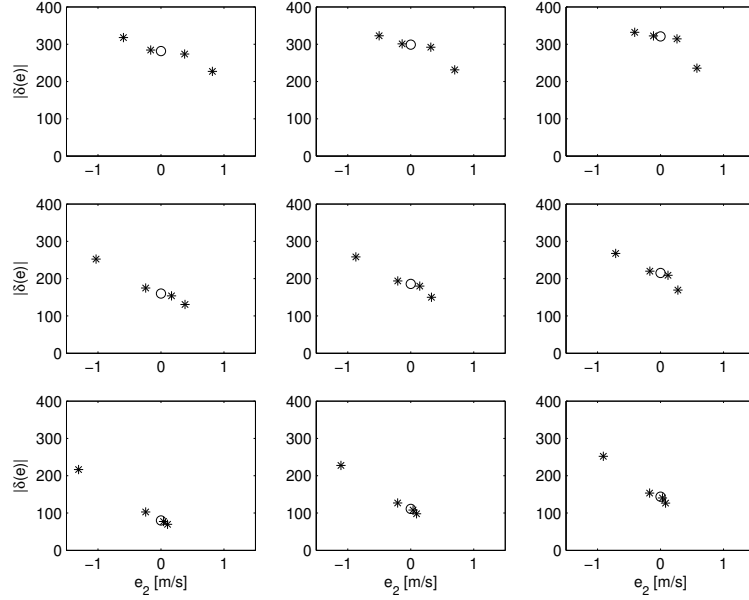


Figure 6.8: Worst case uncertainties for variation in the arc length derivative.

$$k_{\delta 1} = \max \left(\frac{|\max(|\delta(e_1)|) - \varepsilon|}{|e_1|} \right) \quad (6.80)$$

$$k_{\delta 2} = \max \left(\frac{|\max(|\delta(e_2)|) - \varepsilon|}{|e_2|} \right) \quad (6.81)$$

Using these expressions it is assumed that the valid estimates for $k_{\delta 1}$ and $k_{\delta 2}$ can be derived from the maximum value of the uncertainty function $\delta(e)$ for different equilibrium points and different errors. However, this might not be the case as larger values for $k_{\delta 1}$ and $k_{\delta 2}$ might be obtained for less uncertainty. In spite of this (6.80) and (6.81) are used for estimating the constants.

Now, stability is evaluated using the condition stated in (6.64), and below $\theta_M \sqrt{2}$ is calculated for each equilibrium point. As it can be seen, all of the nine values are less than one, and thus, the controlled arc length process is stable under the stated uncertainties. A conclusion that can be drawn only if the qualitative approach used for investigating uncertainties is valid for the system, and also, if the maximal

values for the uncertainties can be used for deriving the worst case slopes $k_{\delta 1}$ and $k_{\delta 2}$.

Data : Loop gains for each equilibrium point:

```
0.5150
0.3136
0.3732
0.7887
0.6632
0.3938
0.8631
0.8296
0.7185
```

If the uncertainties are larger than specified the maximal loop gain increases, and similar, if the uncertainties are less than defined the maximal loop gain decreases. Thus, if the uncertainties become too large the loop gain will be larger than one, which means that the stability cannot be guaranteed. However, it does not mean that the system is unstable. In fact, simulations suggest that the controlled arc length process is stable for large uncertainties. In Figure 6.9 the states x_1 and x_2 for an arc length reference step from 3 mm to 4 mm are shown for both the nominal arc length model, and also, for an arc length model having a large perturbation on the arc length estimator.

In the perturbed system, a 50% error has been added to the arc length estimator, such that, the arc length estimation is 50% too high. As it can be seen, the system is stable under such uncertainty, but as expected, the steady state values are changed, and also, the transients are changed to some extent.

Also, in Figure 6.10 the states x_1 and x_2 for an arc length reference step from 3 mm to 4 mm are shown for the nominal arc length model and an arc length model in which uncertainty is included. Here, a 100% error has been added to both melting speed constants, such that, both melting speed constants are 100% too high. Again, the system is stable, and also, the steady state values and, to some extent, the transients are changed.

From this analysis, presented in this section, it can be concluded that stability of the arc length process controlled by the feedback linearization based controller can be guaranteed for the given assumptions and for a set of realistic uncertainties. Also, simulations suggest that the nonlinear controller is able to cope with large uncertainties with respect to stability. Note, that integral control is not included in

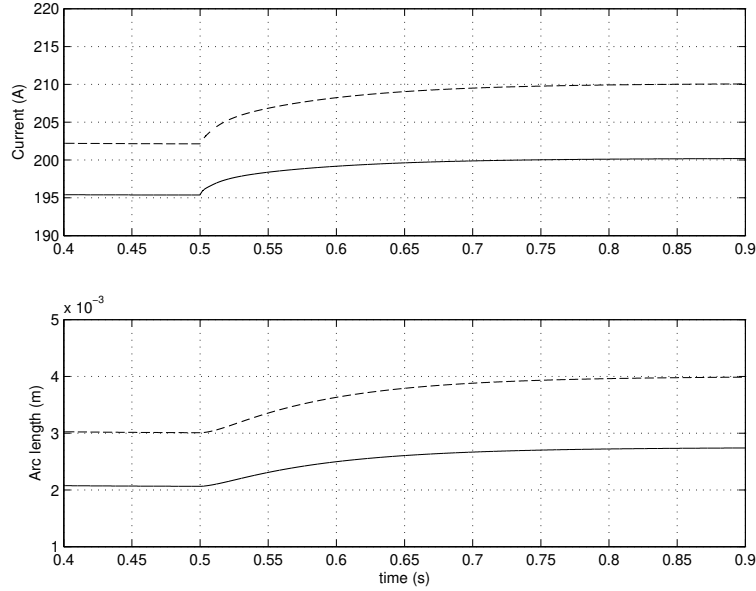


Figure 6.9: Step responses. The estimated arc length is 50% too high.

the controller analyzed in this section, and thus, when including such control, the steady state error on the arc length as a result parameter perturbations not related to the arc length estimate will be removed. Now, having considered stability, performance is considered in the following section.

6.6 Performance

In the former section stability for system uncertainties was considered, and naturally, stability of the closed loop system must be fulfilled. However, the real objective of control is to improve performance. Basically, the feedback controller must be designed, such that, a set of defined performance criteria are fulfilled. Normally, in the time domain, performance criteria are stated by characteristics, such as, rise time, settling time, overshoot, decay ratio, and steady state offset. The first two of these criteria refer to the speed of the response, whereas the last three refer to the quality of the response. Alternatively, it is possible to state performance criteria in the frequency domain. In this case characteristics such as bandwidth, phase margin (PM), and gain margin (GM) are considered. The band-

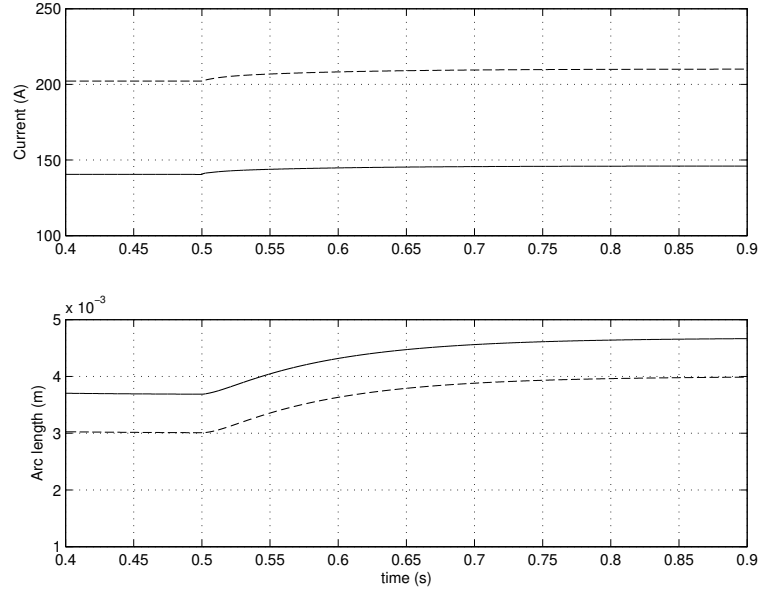


Figure 6.10: Step responses. The melting speed constants are both 100% larger than specified for the nominal system.

width can be seen as the frequency range $[\omega_1, \omega_2]$ in which the control is effective, or alternatively, the bandwidth can refer to the closed loop breakpoint. The latter characteristics, PM and GM, relate to stability and robustness. Moreover, when designing the controller, it is normally not enough to specify the performance criteria, also, the structure of the controller and the control parameters must be found.

Now, let us consider the arc length process. For this system a number of objectives or criteria regarding performance can be identified.

Disturbance rejection : The controller must ensure a constant arc length in spite of disturbances. In particular, disturbances in the contact tip to workpiece distance, l_c , should be considered. In hand held welding, the operator might introduce disturbances by moving the welding pistol. The maximal frequency range for these disturbances is considered to be around 20 Hz, and thus, the controller must be effective in that frequency range, that is, the closed loop system must have a bandwidth of, at least, 20 Hz.

Noise : A considerable amount of noise is present in the system. The control

voltage applied to the GMAW process, and supplied from the welding machine, is a switched signal due to the inverter technology used. Normally, the switch frequency is rather high (50 kHz in Migatron's Flex 4000 machine), and therefore, it will not affect the arc length controller. However, noise is also generated from the power supply net. In Denmark, the welding machine is supplied with three phase 230 Volt at 50 Hz. The three phases are rectified and low pass filtered, and in spite of the low pass filter, the resulting DC supply voltage will be not be a "pure" DC signal, but rather a rippled signal having a frequency of 300 Hz (6×50 Hz). To avoid effects of this kind of noise let us require a closed loop bandwidth somewhat less than 300 Hz.

Steady state error : It is important that the controller is able to keep the arc length constant, but also, it is important that this constant is the reference arc length. Thus, the steady state errors, e_1 and e_2 , must be zero. e_1 being the arc length error, and e_2 being the arc length error derivative, i.e. the error velocity. The reason why zero steady state errors is important is the following. A non-zero equilibrium point arise in the presence of persisting disturbances and uncertainties. These factors are not known beforehand and probably change in time, and therefore, different equilibrium points could be obtain. For example, an equilibrium point having an arc length close to the workpiece causes many short circuits, and thus, such equilibrium point must be avoided.

Command tracking : As stated before it must be possible to control the arc length, such that some desired arc length setting or reference is achieved. However, it has not been considered how fast the arc length reference should be reached (speed of response), and also, how the shape of the response should look like (quality of the response). For ordinary GMAW machines the electrode speed and a welding voltage set point is adjusted on the welding machine display prior to the start of the process. Actually, the voltage setting corresponds to the arc length reference, and thus, the arc length reference is set prior to the start of the process. Anyway, reference changes might prove useful in an advanced control strategy, and therefore, command tracking should be possible, but for now, no particular requirements are defined. However, small or no overshoot seems to be preferable, in fact, both with respect to command tracking and, in particular, with respect to disturbances. For example, if the electrode passes an edge, the result is a step in l_c . In this case a large overshoot might cause a short circuit to occur.

Before designing the controller let us look at the arc length process, that is, equa-

tion (6.9) and equation (6.10). In Figure 6.11, bode plots for 6 different current settings are shown. Current settings of 50 A, 100 A, 150 A, 200 A, 250 A, and 300 A are used. For 50 A, the system has a breakpoint (-3 dB) of around 2 rad/s or 0.3 Hz, and for 300 A, the system has a breakpoint (-3 dB) of around 60 rad/s or 10 Hz.

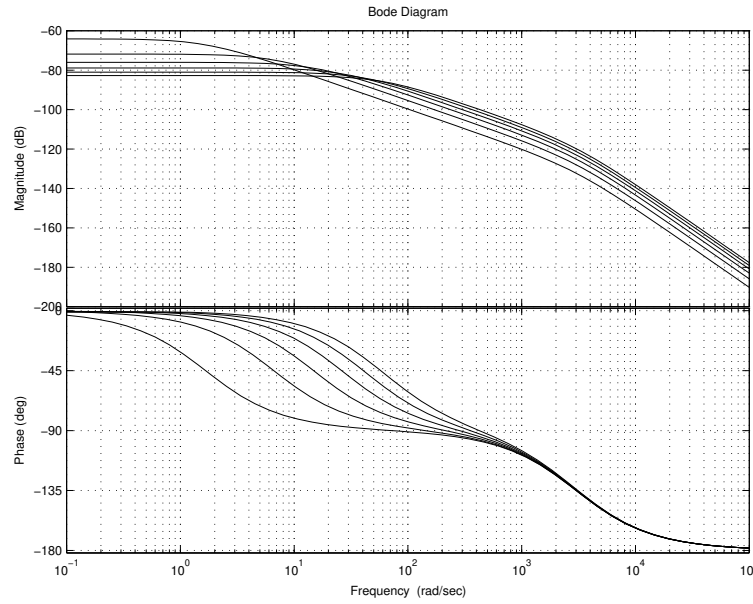


Figure 6.11: Bode plots for six different current settings.

Now, how should the control problem be approached? A classical method is loop shaping where the open loop system $G(s)K(s)$ is shaped. $G(s)$ is the process, and $K(s)$ is the controller. Thus, $K(s)$ is shaped to fulfill the control objectives. Typical this approach is used when the process, $G(s)$, and the controller, $K(s)$, has an input-output structure. However, as stated in Section 6.4 the controller is a state feedback controller. Using such control method, it is, in principle, possible to place the closed loop poles as desired. Though, in expense of large control signals if the closed loop dynamics should be considerable different from the process dynamics, however, this is not the case for the arc length process. The pole placement design method [12, Chapter 7] will be used in this work, as it fits nicely with the state feedback control approached described in Section 6.4.

Before deciding on the closed loop dynamics, i.e. the poles, the process must be considered, and let us define that the real control problem is disturbance rejection. Thus, a satisfying closed loop behavior in the presence of disturbances must be reached, and as stated in the control objectives above, disturbances in the tip to workpiece distance, l_c , is of concern. From equation (6.23) and equation (6.24) it can be seen that both $\gamma(x)$ and $\alpha(x)$ depends on l_c . Thus, disturbances in l_c results in some perturbation, δ , see equation (6.52) and equation (6.53). Hence, we have the following system, where the arc length error, e_1 , is the output.

$$\dot{e} = (A_c - B_c K_c)e + B_c \delta \quad (6.82)$$

$$y = C_c e \quad (6.83)$$

In this system no integral control is included as explained in Section 6.4, and thus, a non-zero steady state error, e_1 , can be expected. However, first, let us consider a controller having no integral control. According to the previously stated control objectives, the closed loop bandwidth must be higher than 20 Hz, but below 300 Hz. Therefore, for instance, let us choose a closed loop bandwidth of 80 Hz or 500 rad/s. Having decided on a closed loop bandwidth, the corresponding closed loop poles must be identified. These pole locations depends on how "sharp" the filter should be. Here, the requirement is small or no overshoot. The actual poles are chosen from a prototype design, and a Bessel filter seems to fulfil the requirement of, at least, small overshoot. Using a Bessel filter having a breakpoint at 80 Hz the poles are given by $(-435.30 \pm 251.33i)$. Now, the control gain vector, K_c , can be obtained using some pole placement algorithm. In Matlab, the algorithms 'acker' or 'place' can be used to obtain the result, and that is, $K_c = [k_{c1} \ k_{c2}]$ where $k_{c1} = 252651$ and $k_{c2} = 871$. In Figure 6.12 the closed loop for this control is illustrated by a bode plot.

In Figure 6.12 it can be seen that the breakpoint lies approximately as specified. Also, it can be seen, that in steady state the error is different from zero. In Figure 6.13 the step response of the system, that is, equation (6.82) and equation (6.82) is shown. It can be seen that practically no overshoot appears for a step.

A zero steady state arc length error can be achieved by including integral control. How such control is included in the control structure is explained in Section 6.4, but first, let us calculate the effect of not having integral control, and also, having integral in the system. Let us assume that some perturbation $\delta = \bar{\delta}$ is present,

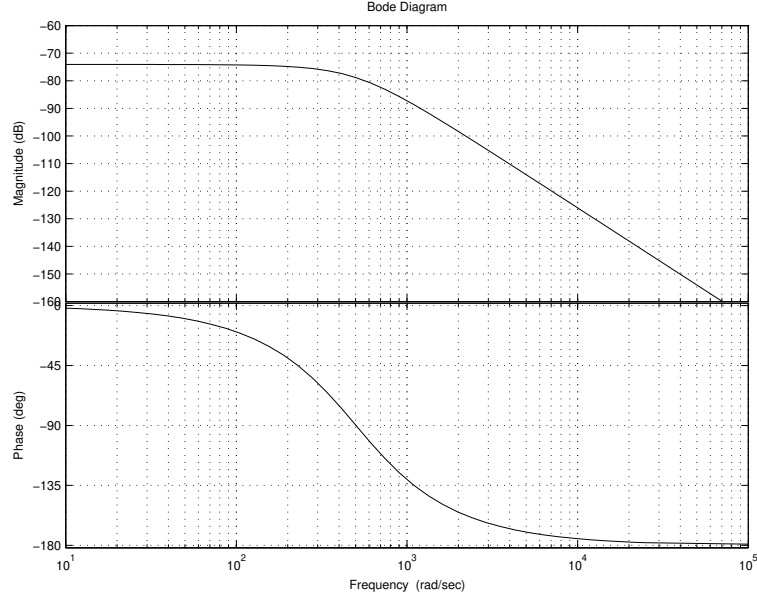


Figure 6.12: Bode plot of the closed loop system without integral control.

then, from equation (6.82) the steady state error can be calculated. Notice, that in steady state $\dot{e} = 0$.

$$\dot{e}_1 = 0 = e_2 \quad (6.84)$$

$$\dot{e}_2 = 0 = -k_{c1}e_1 - k_{c2}e_2 + \bar{\delta} \quad (6.85)$$

\Rightarrow

$$e_1 = \frac{1}{k_{c1}}\bar{\delta} \quad (6.86)$$

Now, if an integrator is used in the closed loop dynamics, see equation (6.41), the following is obtained. notice, that in steady state $\dot{e} = 0$ and $\dot{\sigma} = 0$.

$$\dot{e}_1 = 0 = e_2 \quad (6.87)$$

$$\dot{e}_2 = 0 = -k_{a1}e_1 - k_{a2}e_2 - k_{a3}\rho + \bar{\delta} \quad (6.88)$$

$$\dot{\sigma} = 0 = e_1 \quad (6.89)$$

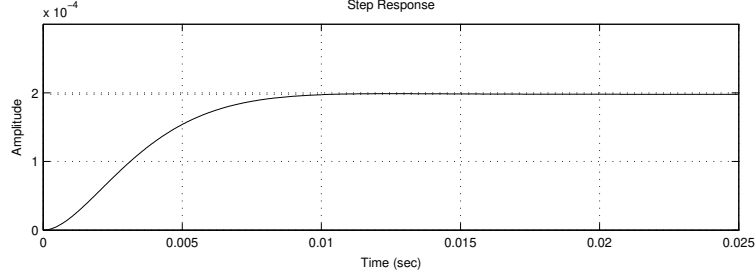


Figure 6.13: Step response for the closed loop system without integral control.

$$\Rightarrow \sigma = \frac{1}{k_{a3}} \bar{\delta} \quad (6.90)$$

Thus, in steady state, using integral control, the integrator state, σ , becomes non-zero, in the presence of a perturbation, but, both e_1 and e_2 are zero. When integral control is included the system given below is considered.

$$\dot{\psi} = (A_a - B_a K_a) \psi + B_a \delta \quad (6.91)$$

$$y = C_a \psi \quad (6.92)$$

Like before, the pole placement approach is used, and also, let us use a Bessel filter prototype, and again, let us choose a closed loop bandwidth of 80 Hz or 500 rad/s. This approach gives the poles $(-473.50, -374.73 + 357.49i, -374.73 - 357.49i)$, and the gain vector $K_a = [k_{a1} \ k_{a2} \ k_{a3}]$, where $k_{a1} = 6.23 \cdot 10^5$, $k_{a2} = 1.22 \cdot 10^3$, and $k_{a3} = 1.27 \cdot 10^8$. In Figure 6.14 a bode plot of the closed loop system is shown. It can be seen that the breakpoint is located at 80 Hz, and also, at low frequencies the error e_1 vanishes. Of course, at high frequencies the error also disappears, but for another reason. Here, the closed loop dynamics are too slow to react on inputs of those frequencies.

In Figure 6.15 the step response of the closed loop error dynamics is shown. As it can be seen the system reacts fast on inputs, but also, the integrator forces the error towards zero.

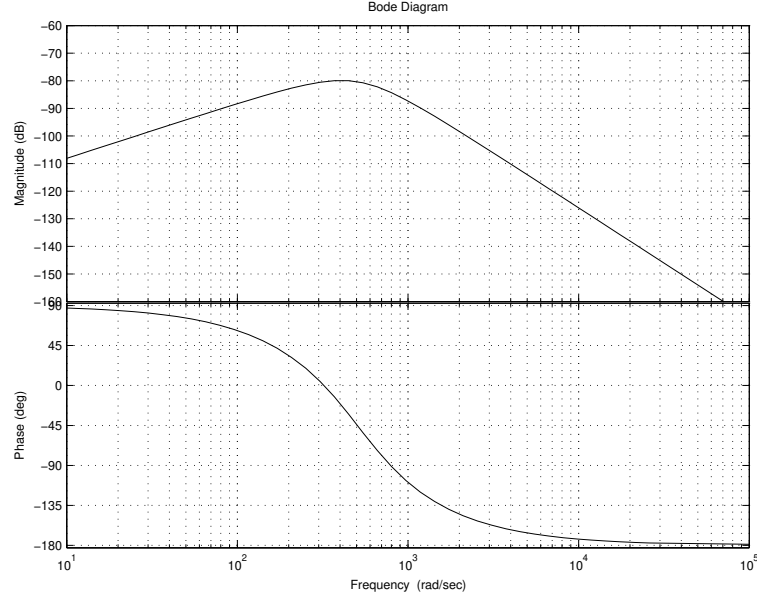


Figure 6.14: Bode plot of the closed loop system including integral control.

Now, the closed loop has been designed, such that, noise does not affect the system, and also, such that disturbances in l_c are rejected. However, command tracking also need to be considered. From equation 6.41 the complementary sensitivity function can be derived, that is, the transfer function from the reference, r , to the output, $y = z_1$.

$$\begin{bmatrix} \dot{z}_1 \\ \dot{z}_2 \\ \dot{\sigma} \end{bmatrix} = \begin{bmatrix} 0 & 1 & 0 \\ -k_{a1} & -k_{a2} & k_{a3} \\ -1 & 0 & 0 \end{bmatrix} \begin{bmatrix} z_1 \\ z_2 \\ \sigma \end{bmatrix} + \begin{bmatrix} 0 & 0 & 0 \\ k_{a1} & k_{a2} & 1 \\ 1 & 0 & 0 \end{bmatrix} \begin{bmatrix} r \\ \dot{r} \\ \ddot{r} \end{bmatrix} \quad (6.93)$$

$$y = C_a \psi \quad (6.94)$$

r is the reference signal, \dot{r} is the derivative, and \ddot{r} is the double derivative of the reference signal. These signals all act as inputs to the system. In Figure 6.16, in Figure 6.17, and in Figure 6.18 the complementary sensitivity functions (transfer function from reference to output) are shown. All plots have a similar break point frequency, and moreover, for low frequencies the effect of the derivatives (\dot{r} and \ddot{r}) vanishes. Thus, according to Figure 6.16, the output (the arc length) equals the

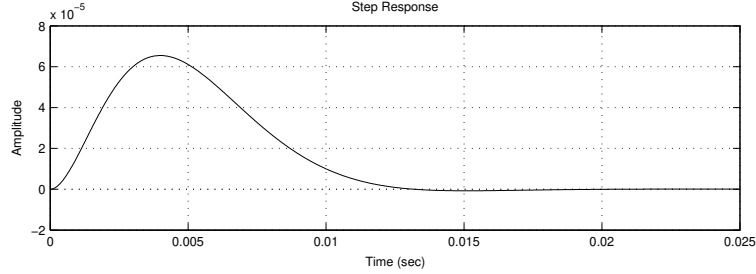


Figure 6.15: Step response for the closed loop system including integral control.

input r for low frequencies.

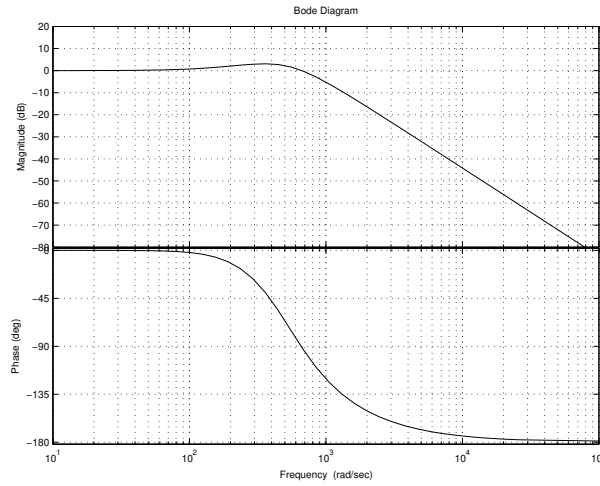


Figure 6.16: Bode plot of the first complementary sensitivity function. Plot for input r and output $y = z_1$.

In Figure 6.19 the sensitivity function, $S(s)$, for r is shown. If the complementary sensitivity function is for r given by $T(s)$, then $S(s) = T(s) - 1$. The sensitivity function is the transfer function from a disturbance at the output, y , to the output, and thus, the sensitivity function shows the ability of the controller to handle disturbances directly at the output. In this case the arc length, z_1 . As it can be seen, the controller dampens disturbances at frequencies below the breakpoint, but on the other hand, at frequencies above the breakpoint the controller has no effect. Similar conclusions can be obtained for the sensitivity functions for \dot{r} and

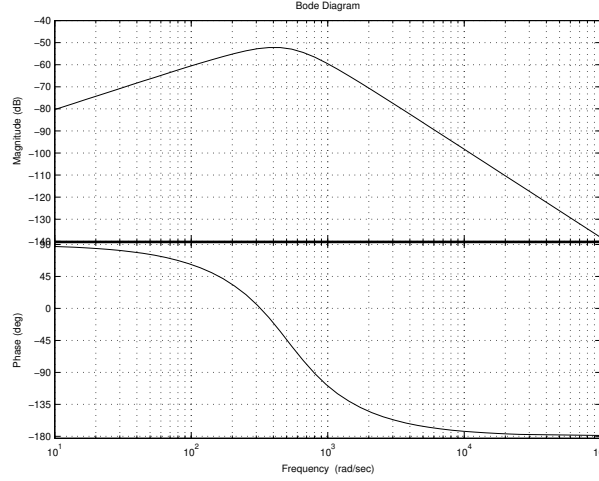


Figure 6.17: Bode plot of the second complementary sensitivity function. Plot for input \dot{r} and output $y = z_1$.

\ddot{r} , though, this will not shown here.

It should be noted that, if different command tracking dynamics is preferred, the reference signal can be filtered to obtain the desired response, typically, faster or slower response. Filtering the reference signal in this way is in [49, Chapter 2] referred to as a 'two degree of freedom control configuration'. However, here, the reference is filtered for another reason. In the control law of equation (6.39) both \dot{r} and \ddot{r} are needed as continuous signals. This can be provided by a second order reference filter expressed in the state space form as shown in the following.

$$\dot{\xi}_1 = \xi_2 \quad (6.95)$$

$$\dot{\xi}_2 = -a_1\xi_1 - a_2\xi_2 + a_1r \quad (6.96)$$

$$r_f = \xi_1 \quad (6.97)$$

$$\dot{r}_f = \xi_2 \quad (6.98)$$

$$\ddot{r}_f = -a_1\xi_1 - a_2\xi_2 + a_1r \quad (6.99)$$

a_1 and a_2 are constants, and r_f , \dot{r}_f , and \ddot{r}_f are used instead of, respectively, r , \dot{r} , and \ddot{r} in equation (6.39).

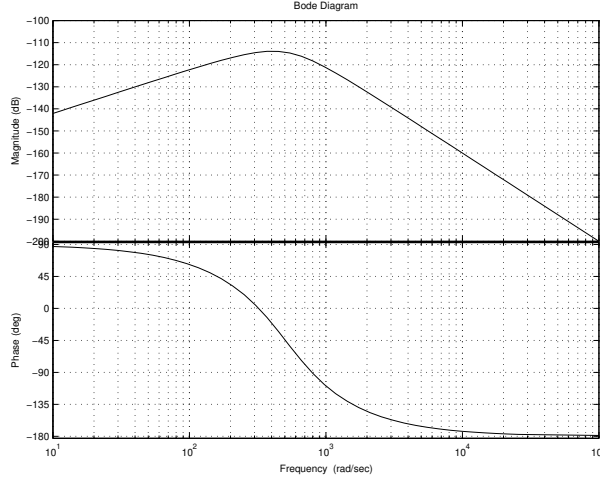


Figure 6.18: Bode plot of the third complementary sensitivity function. Plot for input \ddot{r} and output $y = z_1$.

6.6.1 Simulations

The control structure shown in Figure 6.1 has been implemented in Simulink. Using this implementation, it is possible to simulate the controlled arc length process, and thus, a number of simulations, under different conditions, has been carried out to test the system. Six experiments have been carried out using the implementation in Simulink. These experiments are explained and commented in the following.

Experiment 1: In this experiment integral control is not included, and thus, the control vector K_c is used for the linear control part. The arc length reference, l_{ar} , is set to 0.003 m, the electrode speed, v_e , is set to 16 m/min, and at time $t = 0.5$ s, the contact tip to workpiece distance, l_c , is changed from 0.015 m to 0.010 m. Three states are shown in Figure 6.20, that is, the current I , the arc length l_a , and the contact tip to workpiece distance l_c . As is can be seen, when no integral control is included, a persistent change in l_c from the nominal value gives a steady state arc length different from the reference arc length, which is 0.003 m.

Experiment 2: In this experiment integral control has been included, and now, the control vector K_a is used for the linear control part. Again, the arc length reference, l_{ar} , is set to 0.003 m, the electrode speed, v_e , is set to 16 m/min, and at time $t = 0.5$ s, the contact tip to workpiece distance, l_c , is changed from 0.015 m

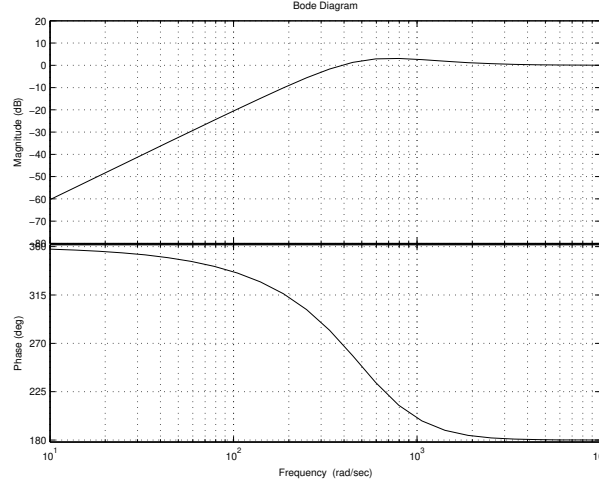


Figure 6.19: Bode plot of the first sensitivity function. Plot for input r and output $y = z_1$.

to 0.010 m. The three states I , l_a , and l_c are shown in Figure 6.21. Here, because of the integrator, the steady state arc length equals the arc length reference.

Experiment 3: This experiment is similar to experiment 2 except for the noise added in experiment 3. Bandlimited Gaussian noise having a mean equal to zero, and a variance equal to 0.002^2 is added to the contact tip to workpiece distance, l_c . The Gaussian noise is bandlimited at 20 Hz to simulate disturbances from manual movement of the welding pistol. The three states I , l_a , and l_c are shown in Figure 6.22. As it can be seen, the controller is able to keep the arc length close to the reference in spite of significant disturbances.

Experiment 4: This experiment is similar to experiment 3 except for the following. No step in l_c is applied, but instead, the arc length reference, l_{ar} , is changed from 0.003 m to 0.004 m at time $t = 0.5$ s. The three states I , l_a , and l_c are shown in Figure 6.23. As it can be seen, the controller tracks the arc length reference signal. The reason for the long transient phase, compared to the transient phase for changes in l_c , is reference filter which only allows for relative slow arc length reference changes. In fact, l_{ar} has a shape, except for the noise, similar to the arc length, l_a , shown in Figure 6.23.

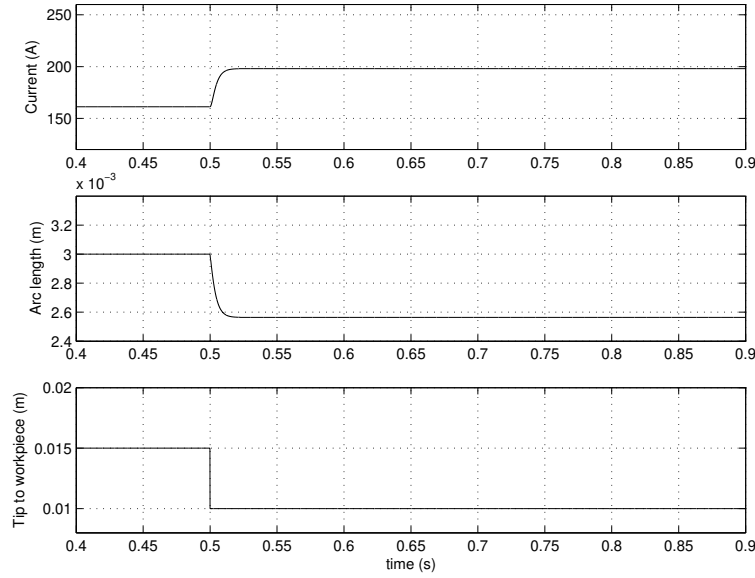
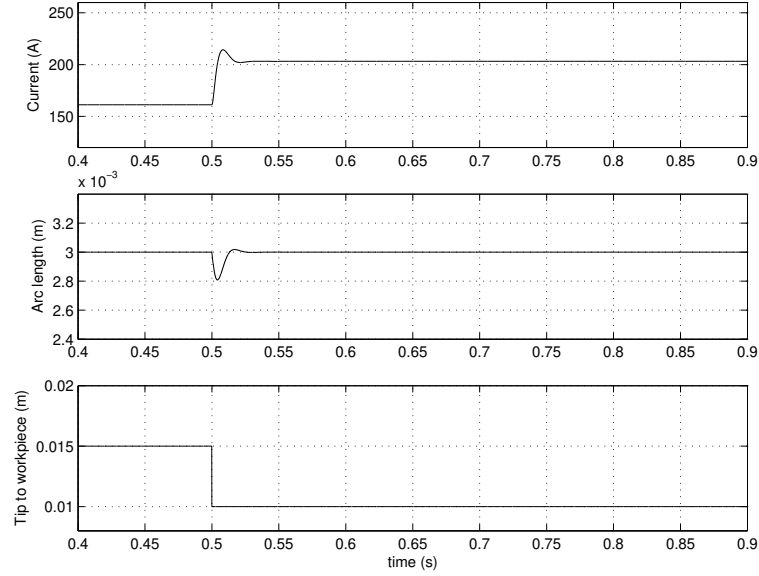


Figure 6.20: Test 1: Step in l_c , and no integral control included.

Experiment 5: This experiment is similar to experiment 4 except for the noise. A 300 Hz sinusoidal signal having an amplitude of 0.0001 is added to the measured arc length, that is, the measured x_2 , see Figure 6.1. This sinusoidal signal is applied to simulate the effect of the three phase supply voltage which is rectified and filtered in the welding machine. Rectification and filtering gives a 300 Hz ripple on the DC supply voltage to the inverter, and as the arc length mainly is measured as a function of the terminal voltage, the effect of the 300 Hz ripple can be simulated by applying a 300 Hz signal at the arc length measurement. The three states I , l_a , and l_c are shown in Figure 6.24.

Experiment 6: In this experiment integral control is included, as in experiment 2 to 5. The electrode speed, v_e , is set to 16 m/min, and at time $t = 0.45$ s, the arc length reference, l_{ar} , is changed from 0.003 m to 0.004 m, and also at time $t = 0.55$ s, the contact tip to workpiece distance, l_c , is changed from 0.015 m to 0.010 m. Bandlimited noise as in experiment 3 is applied, and supply noise as in experiment 5 is also applied. The three states I , l_a , and l_c are shown in Figure 6.25. As it can be seen, the controller maintains the arc length at the arc length reference in spite of the noise and disturbances.

Figure 6.21: Test 2: Step in l_c , and integral control is included.

6.7 Arc Length Reference

In this chapter, drop detachment has not been considered. In fact, drop detachments has not been included in the model describing the arc length process. Thus, it is assumed that electrode material continuously are removed from the electrode during welding. However, in practical welding this is not so. As explained in Chapter 3, melted electrode material forms a drop at the tip at the solid electrode, and at some point the drop detaches from the electrode, and then, a new drop starts forming. For an uncontrolled process (constant voltage), the drop growth and detachment results in an arc length which becomes smaller during the growth period, and then, at drop detachment, jumps to a larger value. Thus, the arc length has a saw-toothed shape. When an arc length controller is applied, such a controller tries to compensate for the changing arc length caused by the drop growth and detachment. However, we want to control the arc length process as if no drop was present, and thus, the arc length controller can be improved by making the arc length reference signal, l_{ar} , saw-tooth shaped. This is shown in Figure 6.26. The reference is high just after expected drop detachments, but low before expected detachments. The difference between the low and the high reference value must be equal to the difference between the length of a drop just before detachment and

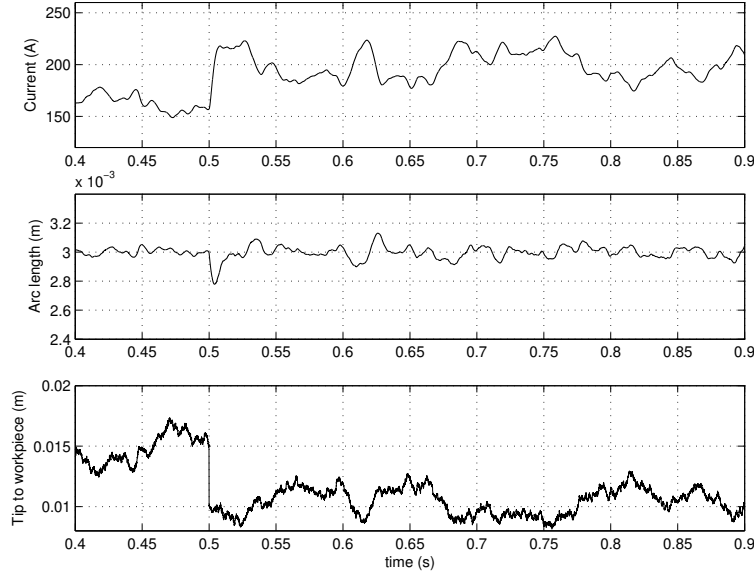


Figure 6.22: Test 3: Step and bandlimited Gaussian noise applied to l_c .

the length of a drop just after detachment.

6.8 Discussion and Conclusion

In this chapter a nonlinear arc length controller has been developed. The nonlinear controller is based on a nonlinear model of the part of the GMAW process which is relevant for arc length control. This model included an approximation of the current dynamics taken the inner current controller into account. Based on the model, the nonlinear system is transformed, into normal form using feedback linearization, in which the functions $\alpha(x)$, $\gamma(x)$, and $T(x)$ are used.

Stabilization and tracking are considered. A reference vector is introduced, and using state feedback control, a condition for stability of the error dynamics is derived. Integral control is included by augmenting the original system with an additional equation, and also, a condition for stability of the system excluding integral control is derived. The nonlinear controller uses feedback measurements of the current and the arc length. The current can be measured directly in the

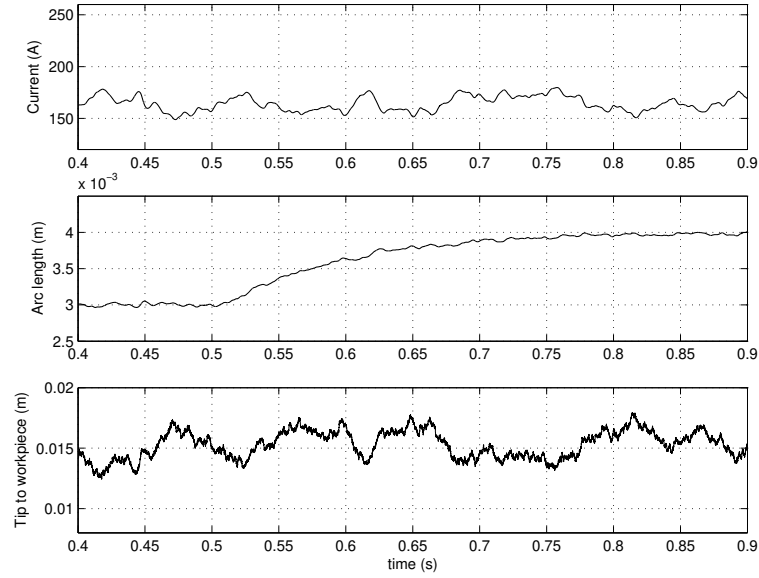


Figure 6.23: Test 4: Reference step, and Gaussian noise applied to l_c .

welding system, but this is not the case for the arc length. The arc length is estimated based on the current and the terminal voltage.

Uncertainty is considered, and based on a general description of uncertainties, the control system dynamics is reformulated with respect to uncertainties. Afterwards, a set of realistic uncertainties are introduced, and stability is proven for a controller with no integral control included.

A number of performance criteria are presented, and based on these criteria, and using a prototype design approach, a set of controller constants are found. The performance criteria used includes disturbance rejection, noise, steady state errors, and command tracking. Especially, disturbance rejection is taken into account, and thus, to avoid disturbances with respect to manual movement of the welding pistol a closed loop bandwidth of 20 Hz is chosen.

To test the arc length controller a simulation program has been developed, and using the program six experiments were carried out. From the experiments it can be derived that integral control is needed to remove the effect of a persistent disturbance or perturbation in the system when compared to the model. Also, it

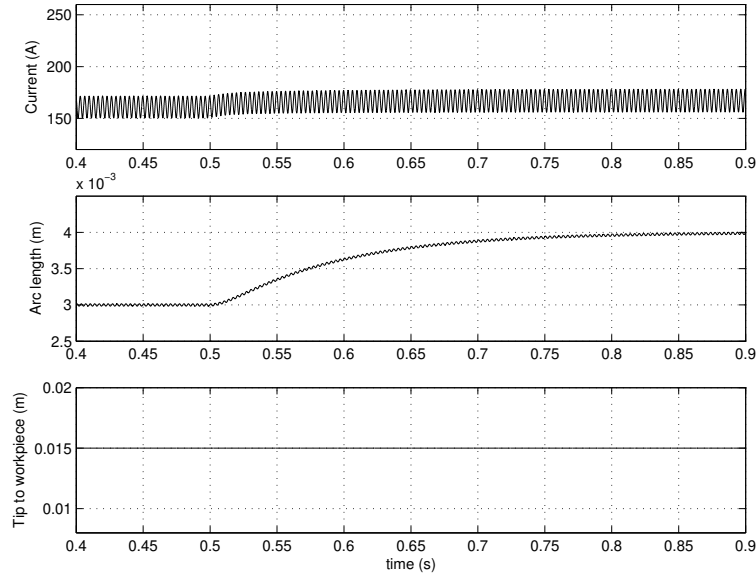


Figure 6.24: Test 5: Reference step, and a 300 Hz sinusoidal signal applied to the measured arc length.

can be seen that the controller is able to handle disturbances and noise which can be expected in practical welding, and moreover, the controller is able to handle command tracking.

The main conclusions of this chapter is stated in the following.

- The arc length process is nonlinear, and to account for this nonlinearity, a non-linear controller has been developed.
- No operation points for the controller need to be selected, and therefore, only one linear controller need to be tuned for all possible arc lengths and current (or electrode speed) settings.
- It has been shown how stability can be analyzed given a set of uncertainties.
- Based on a set of performance criteria it has been shown how to tune the arc length controller.

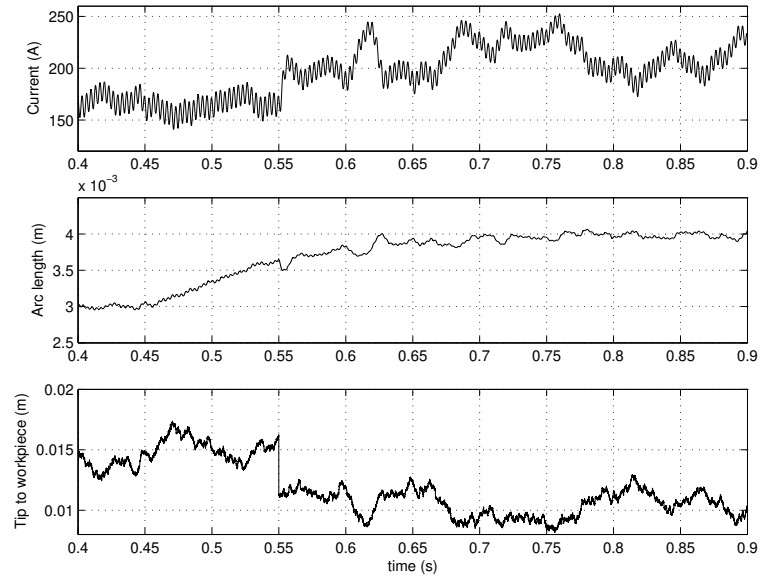


Figure 6.25: Test 6: A step in reference, a step in l_c , bandlimited noise, and supply noise are included.

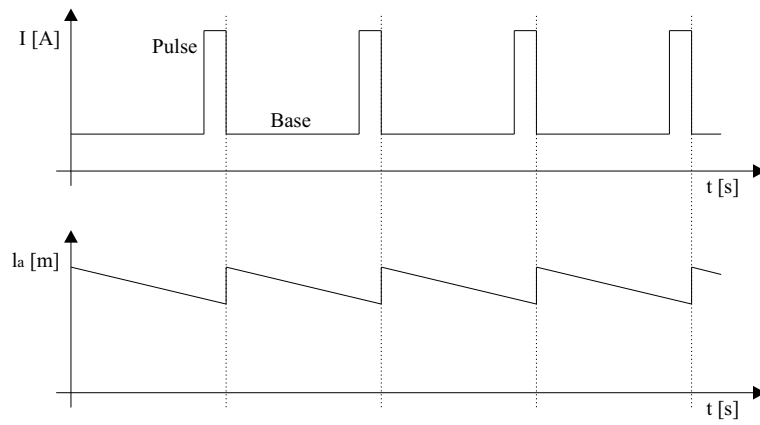


Figure 6.26: saw-tooth shaped reference signal to compensate for drop detachments.

Model Based Metal Transfer Control

7

In this chapter metal transfer control for pulsed GMAW is considered. Two methods for metal transfer control are presented. Both methods are based on obtaining a uniform drop size prior to pulse initiation.

7.1 Objectives and Strategies in Pulsed GMAW

In Chapter 5 it is explained that, basically, two tasks must be taken into account when developing a control system for pulsed GMAW. These tasks are arc length control and metal transfer control. In Chapter 6 an arc length controller for the GMAW process was developed, and in this chapter metal transfer control is addressed. In Chapter 5, configuration of the GMAW control system was discussed, and the arc length controller and the metal transfer controller were put into a cascade coupled structure. This structure is shown in Figure 7.1.

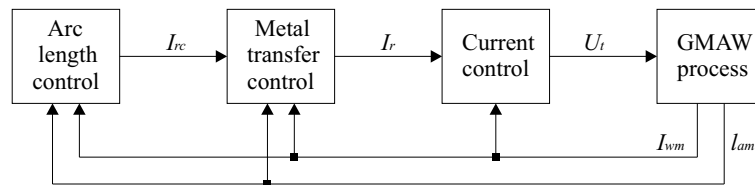


Figure 7.1: The pulsed GMAW control structure.

In pulsed GMAW, current pulses are used for detaching drops at the tip of electrode. As stated in Chapter 5, one pulse should detach one drop, that is, the ODPP (One Drop Per Pulse) objective. To detach a drop for every pulse, the pulse must be strong enough to detach a drop, but on the other hand, not so strong that more than one drop is detached. Moreover, as stated and explained in Chapter 5, the drops should be detached using a minimal amount of energy.

The ability of a pulse to detach a drop depends on the shape of the pulse, and as stated in Chapter 5, a pulse does not necessarily need to have a rectangular shape. Though, this shape was originally used in pulsed GMAW, the rectangular shape is in general not used in modern advanced pulsed GMAW. Rather, in modern advanced pulsed GMAW, the chair shape shown in Figure 7.2 is typically used. Pulse shapes are discussed in Section 7.1.2.

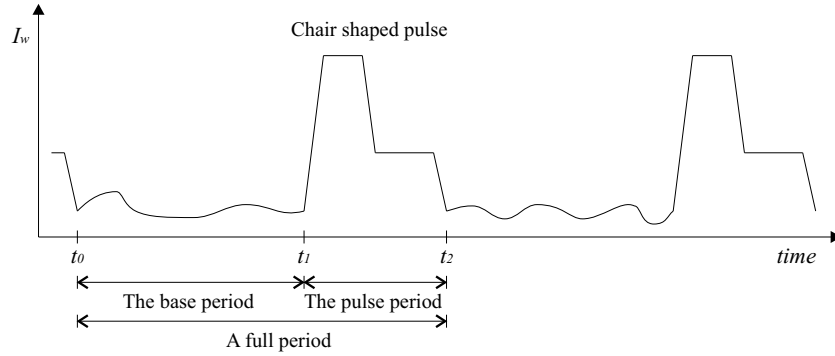


Figure 7.2: The current during pulsed GMAW. A period is divided into a base period and a pulse period. Here, a chair shaped pulse is used.

In Section 3.5, a number of criteria for drop detachment are presented. Three models are presented for drop detachment. These are a static force balance model (SFBM), a dynamic force balance model (DFBM), and a model based on the pinch instability theory (PIT). In both the SFBM and the DFBM, drop detachment depends on the total force, F_T , which, in this thesis is described by the gravitational force, F_g , the electromagnetic force, F_{em} , the drag force, F_d , and the momentum force, F_m . Of these forces the electromagnetic force is far most significant, and F_{em} depends on the size of the drop (drop radius), see equation (3.17). In DFBM, the drop detachment criterium also depends on the acceleration of the drop, and a large acceleration is caused by large changes in the total force, F_T . At strong currents, that is, in the pulse interval, the electromagnetic force dominates in the total force, and thus, as F_{em} also depends on the magnitude of the current, the DFBM becomes dependent of the change in current, that is, dI_w/dt . However, the acceleration does not only depend on the change of force, but also, again, on the size of the drop, as small drops, for some applied force, obtain a higher acceleration than large drops. In the detachment model based on the PIT, the criterium

for detachment depends on the drop radius, r_d , on the position of the drop, x_d , and on the magnitude of the current. The position x_d both depends on the magnitude of the total force, and also, it depends on the change in the total force (or change in current), as a sudden change in force gives rise to drop oscillations, and thus, change in x_d . The conclusion is that, no matter which drop detachment criteria is considered, drop detachment depends on the drop size.

Let us assume that the pulses are given by some fixed shape, such that, all pulses are identical, or at least, all pulses have an identical sequence of control signals, I_r . Also, suppose that the size of the drop, or radius, immediately before initiation of the pulse period differ from period to period. Then, conservative pulse shapes must be used for the pulses to ensure drop detachment for all possible drop sizes. For example, if the drop is relatively small, then, some given pulse shape might not be able to detach the drop. Therefore, to ensure drop detachment, also for the small drop, the pulse height or duration must be increased. However, now, for a large drop, the given pulse shape might be over-sized, in the sense, that the drop is detached in the beginning of the pulse, and thus, the rest of the pulse just contributes to excess melting and a large heat input into the workpiece. Thus, the objective of minimal energy used for drop detachment is not fulfilled.

One approach to ensure drop detachment using a minimal amount of energy is to adjust each pulse to the state of the drop, especially the drop size, immediately before the pulse period initiation. On the other hand, drop detachment with a minimal amount of energy, but using some fixed pulse shape, can be achieved if the drop size is the same immediately before initiation of every pulse period. In practice, it is difficult to derive the shape of a pulse based on the drop detachment models, as these models are not precise. Thus, the specific pulse measures must be determined based on practical experiments. Therefore, a fixed pulse shape is preferred, where it must be ensured that the drop radius (size) is constant before detachment. From a practical point of view, the latter approach seems to be the best solution, and therefore, this 'uniform drop size approach' is chosen. So, the uniform drop size approach becomes the basic idea in the metal transfer algorithm presented in this chapter.

In the following section, arc length control in pulsed GMAW is addressed, and in this context, the drop size is also addressed. Afterwards, the shapes of the pulses are discussed.

7.1.1 Arc Length Control in Pulsed GMAW

In the following, arc length control for pulsed GMAW is considered. Four methods of arc length control for pulsed GMAW will be discussed. The first two methods (method 1 and method 2) are used in the industry today, and especially, the first method. The last two methods (method 3 and method 4), are modifications of the first two methods, but the uniform drop size objective is taken into account. The latter two methods are novel with respect to pulsed GMAW.

Method 1 (Fixed Frequency Method): Traditionally, in pulsed GMAW, a fixed pulse frequency is used, and during the base period, see Figure 7.3, the arc length controller is active, and thus, the arc length is adjusted during the base period. So, no arc length control is carried out in the pulse period, and thus, this lack of arc length control results in a decrease in performance (the ability to react on arc length changes). However, in general, the average current, or alternatively, the average melting rate, is much higher during the pulse period. This means, that the arc length control performance is decreased for an increasing arc length, but on the other hand, the performance is maintained for a decreasing arc length. From a practical point of view, it is important to maintain the performance for a decreasing arc length arc, as short circuits must be avoided, but a decrease in performance for an increasing arc length is in most applications of less concern. However, if one wants to minimize the energy developed in the arc during one period, E_p (see below), the arc length (corresponding to the arc voltage, U_a) must be low, but a small arc length might be difficult to maintain if the performance for an increasing arc length is decreased.

$$E_p = \int_{t_0}^{t_2} U_a(t) I_w(t) dt \quad (7.1)$$

As stated before, the arc length controller is active during the base period. Thus, during this period, the arc length controller outputs a control signal, the reference current I_{rc} . This results in some electrode melting in the base period. The piece of melted electrode material is expressed in the following. x_{mb} [m] is the piece of melted electrode in the base period. Time t_0 and t_1 are shown in Figure 7.3.

$$x_{mb} = \int_{t_0}^{t_1} v_m(I_{rc}, l_s) dt \quad (7.2)$$

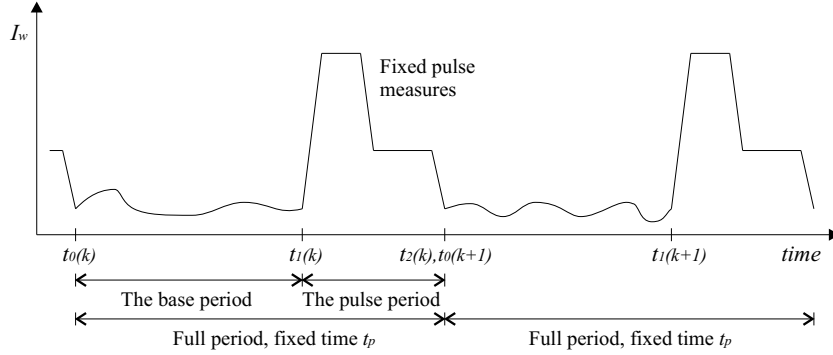


Figure 7.3: The fixed frequency method. Arc length control is carried out by direct adjustment of the current reference during the base period.

There is no guarantee that x_{mb} does not vary from period to period due to the control effort for arc length control, and therefore, using this fixed frequency method, a uniform drop size at detachment cannot be obtained.

Method 2 (Pulse-by-pulse Method): Instead of using a fixed frequency (fixed period), a variable period can also be used in pulsed GMAW. Here, the length of the base period is used for controlling the arc length, and therefore, a fixed base current is used. The control is carried out on a pulse-by-pulse basis, such that, the base period length is calculated based on the information from the former period, that is, the average arc length and the average melting effort. This is illustrated in Figure 7.4.

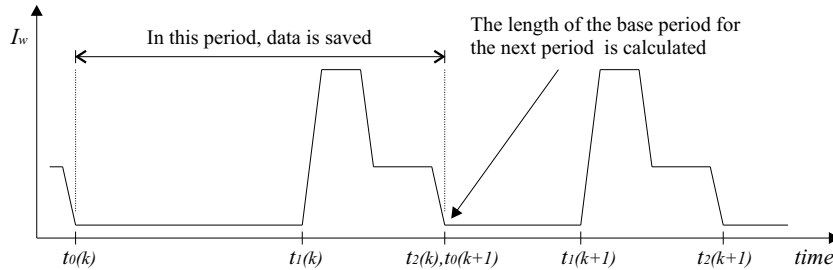


Figure 7.4: During every period welding measurements are obtained and saved. Just before initiation of a new period, the length of the base period is calculated based on the saved measurements.

A large base period equals a small control effort, and on the other hand, a small base period equals a large control effort. Such approach is used in a number of advanced and modern welding machines. It seems, that the reason for using such control approach, is the ability to control the arc length also for low arc length references. The average energy developed in the process becomes a function of the time period between the pulses and not, as for the fixed frequency method, the base current level. The base current can only be lowered to some point, as the arc must be maintained, but for the variable frequency method, the base current is fixed, and thus, the arc can be maintained for a low arc length reference.

Like the fixed frequency method, the varying pulse period method also has a decreased performance with respect to arc length control. This decrease in performance is caused by the pulse-by-pulse control approach, as a time delay is introduced into the control system. Such time delay has a great influence at low pulse frequencies. For example, in some welding applications, the average pulse frequency can be as low as 5 Hz, and thus, the time between each update is rather long.

Method 3 (Compensation Control Method): In the third method, like the second method, a variable base period is used, and also, the fixed base current approach is used. However, the pulse-by-pulse approach is avoided. Now, the arc length controller, in the base period, controls the process as if no metal transfer controller was present (see Figure 7.1), but instead of applying the arc length control signal, the fixed base current is applied to the process. In the end of every base period, additional electrode material is added to the drop to obtain a uniform drop size prior to detachment. In Section 7.2 this is described in greater detail.

Method 4 (Direct Control Method): In the first method, the arc length is controlled by adjusting the current during the base period, and in the second method, the arc length is controlled by adjusting the base period time given some fixed base current. However, in this method, both principles are used at the same time, that is, both base period current control and base period time control. Now, instead of defining the current settings during a whole period, and prior to the period, the current is adjusted during the base period, as in the first method. However, the frequency is not fixed, as in the first method, as a pulse is initiated when a certain length of a electrode has been melted. This means, that a uniform drop size prior to the pulse period is obtained. Like method 3, this method is described and

analyzed in greater detail in Section 7.2.

7.1.2 Pulse Shapes

In this section, different pulse shapes are discussed. In the pulsed GMAW process, current pulses are used for drop detachment. Basically, strong current helps drop detachment because of the strong downward acting force, and moreover, because of the pinch effect. A strong current results in a strong electromagnetic force, F_{em} , see equation (3.17), and if this force exceeds the surface tension force, drop detachment occurs. Also, a strong force pinches the neck of the drop, and thus, helps drop detachment, see Appendix C. However, drop detachment does not only depend on the level of the current. Some important characteristics are stated in the list below, where static characteristics are left out, as, for example, the surface tension constant, γ_{st} .

- The size of the drop.
- The magnitude of the pulse current.
- The current derivative, dI_w/dt .

The effect of these characteristics have already been discussed in some detail, except for the current derivative, which has only been shortly discussed. So, with respect to the current derivative, a sudden change in current causes a sudden change in the electromagnetic force acting the drop, and thus, the drop starts to oscillate. The drop, attached to the tip of the electrode, either moves towards or away from the electrode. When the drop is close to the tip of the electrode, drop detachment is difficult, but on the other hand, when the drop is stretched out, drop detachment becomes easier. This is included in the PIT drop detachment model, see equation (3.30), by the drop position, x_d .

The ability of strong currents to provide drop detachments, suggest that a rectangular pulse should be used for drop detachments in the welding process. However, in industry and in the literature, other pulse shapes are also used or suggested. Such shapes are illustrated in Figure 7.5 and discussed in the following.

Four different pulse shapes are shown in Figure 7.5. The first pulse shape, in Figure (A), is the rectangular pulse. Such pulse shape was traditionally used in pulsed GMAW, but today, modern welding machines rather use the pulse shapes

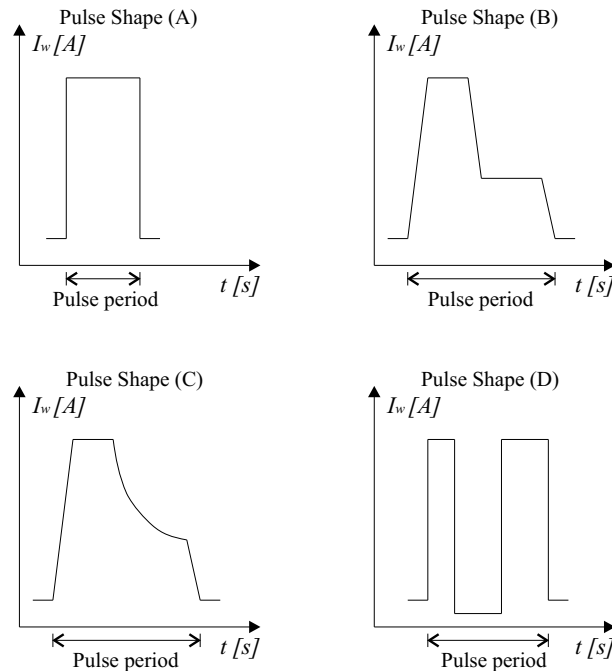


Figure 7.5: The figures shows welding current during the pulse period. (A) A rectangular pulse shape. (B) A chair formed pulse shape. (C). A chair form with exponential current decrease. (D) A double pulse.

illustrated in Figure (B) and (C). The chair shape of Figure (B) starts by an increase of current up to the top pulse current level. By using some slope, which can be provided by the welding machine, rather than an instantaneous increase in current, which cannot be provided, the real current slope becomes independent of uncertainties and discrepancies in the welding machine and the process. This is important, as the pulse shape is not tuned for every machine and every process.

Clearly, the purpose of the top pulse is drop detachment, but in Figure (B) and (C), the current slopes down toward some lower current level. In practice, the pulse shapes in Figure (B) and (C) provides good results, but present knowledge of the welding process does not seem to give a precise answer. This is probably because of the complexity of the drop detachment process. However, if considering the electromagnetic force one can speculate on the reasons. Experimentally, it has be

observed that, for good weld quality, drops should be detached just after the top pulse. However, it is difficult to ensure that drops always detach on the downward slope from the top pulse. Thus, this suggests a lower level current followed by top pulse. Moreover, as stated before, if the change of current is high, the drop starts oscillating. Such oscillation, or drop movement, either helps or dampens the drop detachment process, and thus, for robustness, it might be best to avoid a rapid fall in current, as illustrated in Figure (C).

In the last figure, Figure (D), two pulses are shown. Such pulse shape is proposed in [52] and in [56], but has, to my knowledge, not yet been adopted by welding machine producers. The idea by having two pulses is the following. The first pulse should not detach the drop, but rather, the first pulse should provide drop excitation, that is, drop oscillations. Next, the second pulse should be applied when the drop moves downward, and thus, for drop detachment, take advantage of the drop momentum. Potentially, such approach could provide drop detachment at the expense of less energy when compared to other pulse shapes.

7.2 Uniform Drop Size

In this section, the third and the fourth method mentioned in Section 7.1.1 will be described in greater detail. In both methods, the aim is to ensure a fixed drop size prior to the pulse period. In Figure 7.2, the base period and the pulse period are shown, and using time t_0 , t_1 , and t_2 from the figure, the total melting of electrode during the whole period is given below. The total melting x_{mt} is expressed as length of electrode.

$$x_{mt} = \int_{t_0}^{t_2} v_m(I_w, l_s) dt = \int_{t_0}^{t_1} v_m(I_w, l_s) dt + \int_{t_1}^{t_2} v_m(I_w, l_s) dt \quad (7.3)$$

where v_m could be expressed by

$$v_m(I_w, l_s) = k_1 I_w + k_2 I_w^2 l_s \quad (7.4)$$

k_1 and k_2 are constants, I_w is the welding current, and l_s is the electrode stick-out.

Now, as stated above, the aim in both methods is to ensure a uniform or fixed drop size immediately prior to the pulse period. If one drop is detached for every

pulse, it can be expected that the drop detaches during the pulse period, and given a uniform drop size at the beginning of the pulse period, it can also be assumed that the drops detaches approximately at the same point in time during the pulse period. Thus, considering that the melting speed, v_m , mainly depends on the current, which is fixed to some shape during the pulse interval, the melting prior to detachment can be expected to be constant. Therefore, to ensure a uniform drop size prior to detachment, only the base period melting length, x_{mb} , need to be considered. In the base period, the length of melted electrode, x_{mb} , can be expressed as in the following.

$$x_{mb} = \int_{t_0}^{t_1} v_m(I_w, l_s) dt \quad (7.5)$$

In general, for some fixed pulse frequency, the melting length x_{mb} will not be uniform, as this variable depends on the control effort during the base period to maintain the arc length reference. For a large control effort, that is, a large average I_{rc} during the base period, the melting length x_{mb} will be large, but on the other hand, for a small control effort, the melting length x_{mb} will be small. Thus, x_{mb} is not uniform. However, a uniform melting length can be obtained by adjusting the length of the base pulse period during welding. This is explained in the two proposed methods in the following. The first method, that is, Method 3 in Section 7.1.1, is called the 'compensation control method'. The second method, that is, method 4 in Section 7.1.1, is called the 'direct control method'.

7.2.1 Compensation Control Method

In this method, the arc length is controlled by adjusting the length of the base period, as the current, in this period, is fixed at some base current level, I_{rb} . Also, the shape of the pulse in the pulse period is fixed. The length of the base period depends on the control effort from the arc length controller, and thus, the total length of melted electrode during the base period is not uniform. Therefore, to obtain a uniform drop size, additional melting is done by the end of the base period to compensate for the drop size. Electrode material are added to the drop, and thus, only small drops can be compensated to obtain the desired drop size. Already melted material cannot be removed. However, as a rather low current is used during the base period, the drop size will normally be too small.

As stated above, arc length control is carried out by adjusting the length of the

base period. To make such adjustments, any arc length controller, with the current reference as the control signal, I_{rc} , can be used. No special controller needs to be designed for arc length control in pulsed GMAW, see Figure 7.1. The length of the base period is determined from the control effort as stated below. The control effort can be expressed as a melting speed control signal, $v_m(I_{rc}, l_s)$, which is integrated to give the melting length. The melting speed v_m is given by equation (7.4), and for simplicity, l_s is assumed to be constant. Now, when the integral exceeds some constant, x_{cond} (melting length condition), a pulse is initiated.

$$\text{Pulse if : } \int_{t_0}^{t_1} v_m(I_{rc}, l_s) dt \geq x_{cond} \quad (7.6)$$

During the base period, the current reference, I_r , see Figure 7.1, is not given by the arc length control signal I_{rc} , but rather, the current reference is given by some fixed base current I_{rb} . The length of melted electrode in the base period is given by the welding current, which depends on the reference I_{rb} , and the stick-out during this period. Thus, we have

$$x_{mb} = \int_{t_0}^{t_1} v_m(I_w, l_s) dt \quad (7.7)$$

If x_{mbr} is the desired base period melting length, that is, the reference melting length, a melting length error, e_{mb} , can be defined.

$$e_{mb} = x_{mbr} - x_{mb} \quad (7.8)$$

The melting length x_{mb} depends on x_{cond} , as the base period length depends on this constant. Therefore, x_{cond} should not be too large, as a large x_{cond} might result in a negative e_{mb} , which means that the drop is too large. In general, as a low base current, I_{rb} , is used, the control signal, I_{rc} , will be larger than the welding current, and therefore, to ensure some drop compensation, the melting length condition, x_{cond} , is chosen such that

$$x_{cond} = x_{mbr} \quad (7.9)$$

Now, the melting length error, e_{mb} , must be compensated for. This is done during a short compensation interval, see Figure 7.6. In a time interval Δt_c , the current I_{wc} is applied to the process to compensate for e_{mb} .

$$e_{mb} = v_m(I_{wc})\Delta t_c \Rightarrow \Delta t_c = \frac{e_{mb}}{v_m(I_{wc})} \quad (7.10)$$

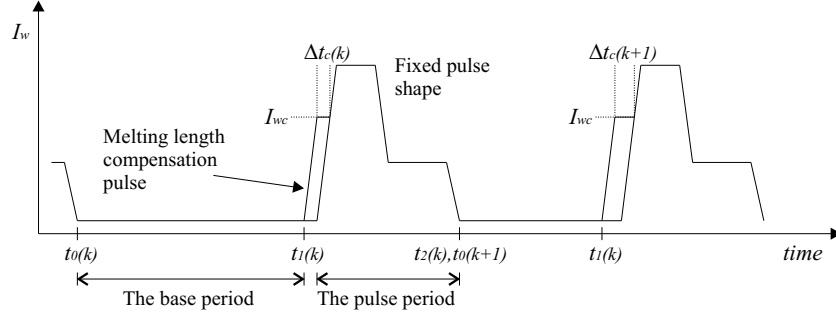


Figure 7.6: The compensation control method. Immediately after the base period, additional melting is done to obtain a uniform drop size prior to the pulse period.

7.2.2 Direct Control Method

In the direct control method, that is, Method 4 in Section 7.1.1, the length of the base period is adjusted like in the compensation control method. However, during the base period the arc length is controlled directly by the arc length controller. Thus, no compensation like in Method 3 is required. Like for the compensation control method, a pulse is initiated when some specified length of electrode has been melted. As no compensation is included, the specified length of electrode must be the reference melting length, x_{mbr} . So, the following condition is obtained.

$$\text{Pulse if : } \int_{t_0}^{t_1} v_m(I_w, l_s) dt \geq x_{mbr} \quad (7.11)$$

Notice, that the measured welding current is used instead of the control signal, as used in condition (7.6). This is possible as I_w and I_r are almost equal (I_w is controlled by the fast inner current controller, see Figure 7.1), and moreover, as in the base period, $I_r = I_{rc}$. In Figure 7.7 the direct control method is illustrated.

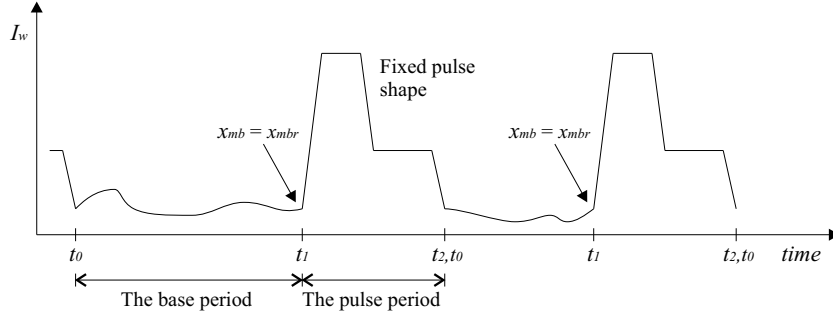


Figure 7.7: The direct control method. During the base period the arc length controller, directly, controls the arc length. A pulse is initiated, at $t = t_1$, for $x_{mb} = x_{mbr}$.

7.3 Simulations

In this section, the two methods described in the previous section are implemented and tested in a simulation program developed in Simulink. Also, the two methods are compared to Method 1 in Section 7.1.1, that is, the fixed frequency method. Method 2 is not implemented and compared to the other methods, as this method requires a different arc length controller, and thus, the value of such comparison is limited. In Figure 7.8, the developed simulation program is illustrated, and in the following, five different experiments are carried out using the simulation program. The results from these experiments are presented below, but first, the simulation program and the settings are explained.

In Figure 7.8, the simulation program is illustrated. The arc length reference is filtered by the second order filter and the states r , \dot{r} , and \ddot{r} are provided to the arc length controller, see Chapter 6. Also, the measured current, that is I_{wm} , the estimated arc length, l_{am} , and the electrode speed, v_e , are fed to the arc length controller. The arc length controller outputs the reference control current, I_{rc} , which is fed to the metal transfer controller. In this controller, either the fixed frequency method, the compensation control method, or the direct control method is implemented, but for all methods the chair pulse shape, shown in Figure 7.5.(B), is used. The output from the metal transfer controller is the reference current, which becomes the input to the inner current controller and the GMAW process. The model of the GMAW process includes the melting rate model, and the equations describing the drop dynamics. The model based on the pinch effect theory

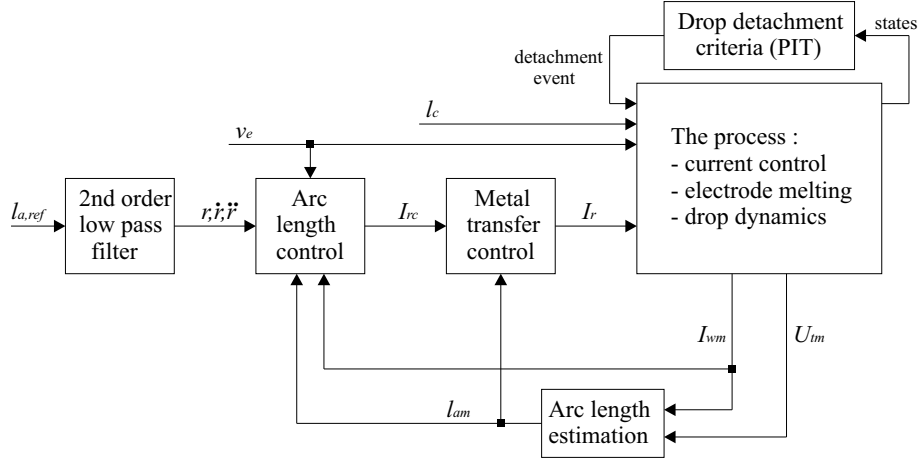


Figure 7.8: An illustration of the simulation program developed in Simulink.

(PIT) is used for evaluating when drop detachments occurs, as the PIT model is well suited for describing drop detachment for strong currents. An electrode speed $v_e = 6$ m/min is used for all experiments presented in the following, and if not stated otherwise, an arc length reference of 0.003 m is used. Other parameters can be found in the Nomenclature.

Experiment 1: In this experiment no disturbances or noise are included, and also, nominal parameters and settings are used. During the pulse period the top pulse level is set to 340 A. In Figure 7.9 the welding current from time $t = 0.1$ s to $t = 0.5$ s are shown for, respectively, the fixed pulse method (M1), the compensation control method (M3), and the direct control method (M4). The stars in the upper part of the plots shows the drop detachment locations during the time interval. For the fixed frequency method, drop detachment does not occur for all pulses, which means, that the ODPP objective is not reached. However, for both the compensation control method (M3) and the direct control method (M4), drop detachments occur for all pulses. This indicates that the ability of M3 and M4 to adjust the base period, to obtain the some preferred drop size, has a positive effect with respect to drop detachment and the ODPP objective. A zoom on Figure 7.9 is shown in Figure 7.10. In this figure, the welding current during the pulse periods and the base periods can be seen. For M1 and M4, in the start of the base period, the welding current is very low, as the control output, I_r , saturates to some spec-

ified lower limit. This is because a drop has just been detached, and thus, the arc length has become too long. Later during the base period, the arc length reaches the reference arc length, and more power must be put into the process to keep the arc length at the reference. Notice, that the saw-tooth shaped arc length reference proposed in Section 6.7 has not been implemented in the simulation program. If it was, the base current in M1 and M4 would rather have a shape like, for example, in Figure 7.7.

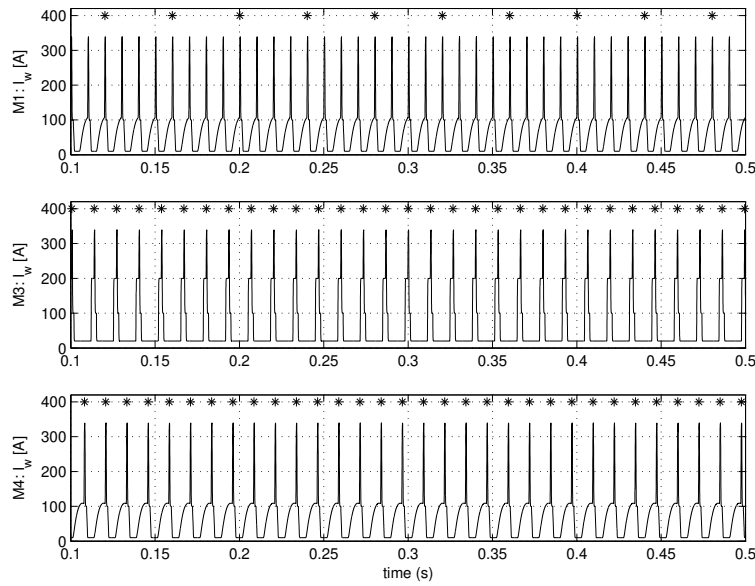


Figure 7.9: Experiment 1. The welding current for the three methods, M1, M3, and M4. The stars on the plots shows the drop detachment locations.

Experiment 2: This experiment is similar to experiment 1 except for one parameter. In experiment 2 a pulse top current of 380 A is used. The result is shown in Figure 7.11 for M1, only. Now, as it can be seen, drop detachment occurs also for M1. So, by increasing the top current level, and thus, the energy generated by the pulses, the ODPP objective is reached for M1, but on the other hand, the drops are not detached using a minimal effort (energy), as less energy was used for drop detachment for M3 and M4 in experiment 1. This can be seen by comparing Figure 7.11 with M3 and M4 in Figure 7.9. Compared to M3 and M4 in Figure 7.11, M1 in Figure 7.11 has more and stronger pulses, and thus, more energy is used.

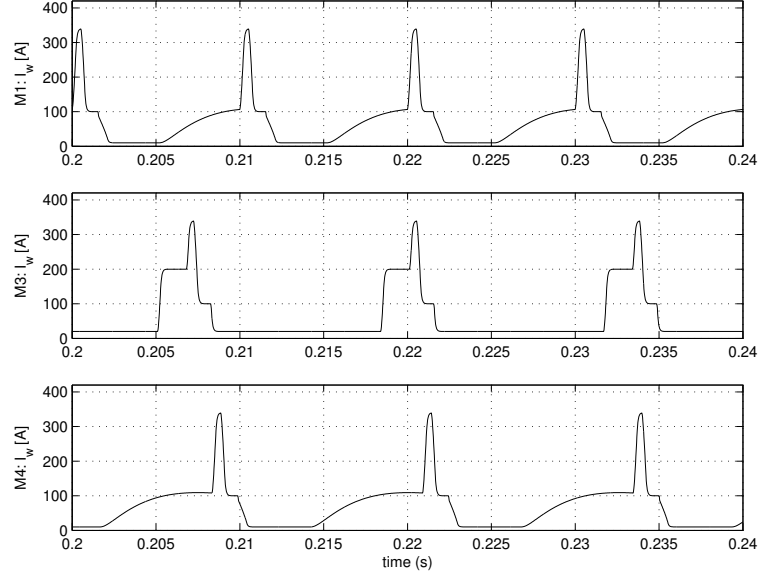


Figure 7.10: Experiment 1. A short time interval. The welding current for the three methods, M1, M3, and M4 are shown.

So, experiment 1 and 2 suggests that, using the two proposed methods, that is, the compensation control method (M3) and the direct control (M4), less detachment effort is required.

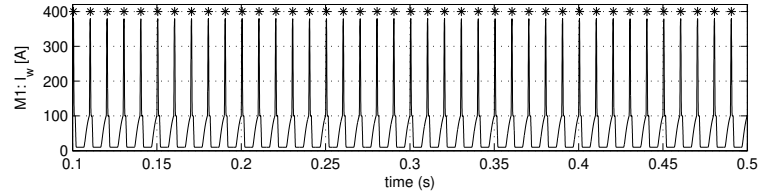


Figure 7.11: Experiment 2. The welding current for the fixed frequency method, M1. The stars on the plot shows the drop detachment locations.

Experiment 3: This experiment is similar to experiment 1 except for the following. The contact tip to workpiece distance, l_c , is changed during simulation, such that $l_c = 0.015 + 0.003 \sin(10\pi t)$. Thus, l_c is moved in a 5 Hz sinusoid around the nominal value. In Figure 7.12, the current for the three methods are shown.

As is can be seen for M3 and M4 , the frequency is affected by the sinusoidal disturbance, and also, the ODPP objective is maintained in spite of the disturbances. This is not the case for M1.

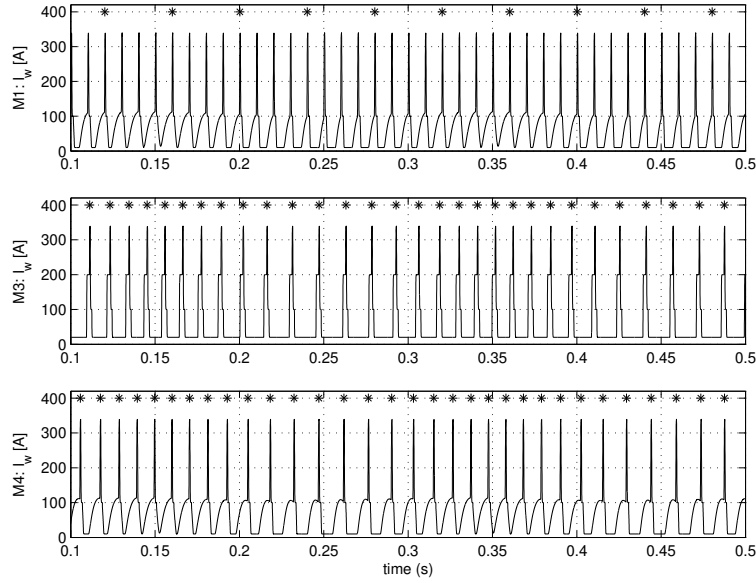


Figure 7.12: Experiment 3. The welding current for the three methods, M1, M3, and M4. The stars on the plots shows the drop detachment locations.

In Figure 7.13, the length of melted electrode is shown for the three methods. For the fixed frequency method, which does not provide detachment for every pulse, the drop grows rather large and detaches after a number of pulses. For the other methods, it can be seen, that the sinusoidal disturbance results in different drop sizes both at detachment and prior to the detachment pulse. Thus, a uniform drop size prior to the pulse period is not obtained. The reason for this is the disturbance in l_c , as the melting speed estimate (equation (6.2)) is based on the parameter l_c . However, in spite of the changing l_c , drop detachment still occurs, and apparently the two methods, M3 and M4, have some robustness. In Figure 7.14, it can be seen, for M3, how the drop oscillates during a short period of time. x_d is the drop position, using a downward pointing axis. So, each peak corresponds to a point where a large force is applied to the drop, and that is, in the pulse period.

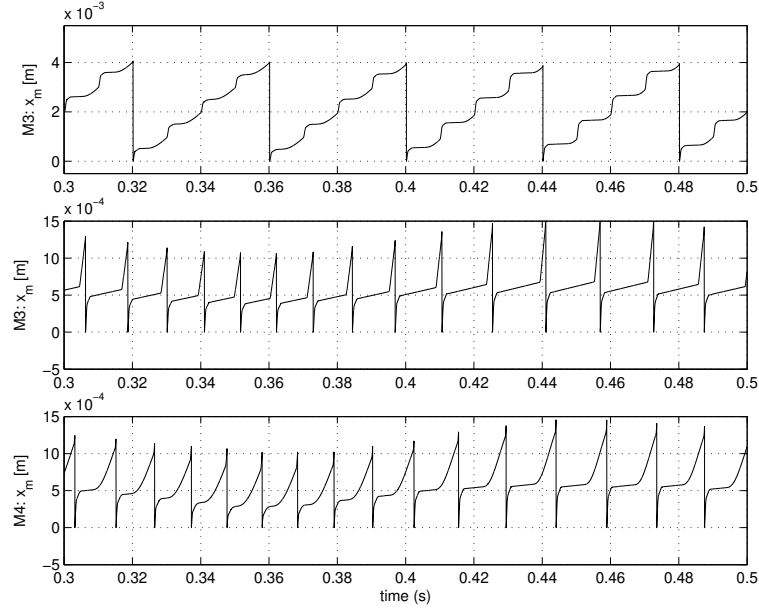


Figure 7.13: Experiment 3. The length of melted electrode between drop detachments for the methods M1, M3, and M4.

Experiment 4: This experiment is similar to experiment 1 except for the following. At $t = 0.25$ s the contact tip to workpiece distance, l_c , is changed from the nominal value 0.015 m to 0.012 m, and also, bandlimited noise is applied to l_c . The noise has a mean equal to 0, a variance equal to 0.002^2 , and is bandlimited at 20 Hz, such that, the energy in the signal is maintained. Under such disturbance, currents and detachments are shown for the fixed frequency method (M1), the compensation control method (M3), and the direct control method (M4) in Figure 7.15. Now, as it can be seen, the ODPP objective is not reached for both M1 and M4. So, it appears that M4 is less robust when compared to M3. However, with respect to the ODPP objective this could be expected, as for M3, the compensation pulse helps detachment. On the other hand, M3 has a disadvantage, compared to M4, which has not yet been mentioned. During the base period the direct control method is able to react instantaneous on arc length errors, but this is not the case for M3, as the base current is fixed. Thus, M3 is less suited to react on short circuits or near short circuits (very low arc voltage) with the workpiece.

Experiment 5: This experiment is similar to experiment 4 except for the follow-

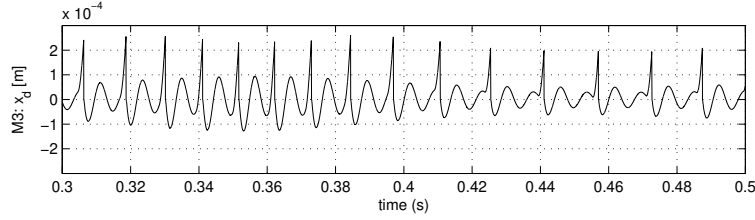


Figure 7.14: Experiment 3. The position of the drop during welding for the third method, M3.

ing. No step in l_c occurs, but instead, the arc length reference is changed from 0.003 m to the 0.005 m at $t = 0.25$ s. Notice, that as the reference is filtered by a low pass filter, the actual arc length reference signal changes from 0.003 m to 0.005 m during some time interval. The arc length for M3 is shown in Figure 7.16. This experiment indicates that, in spite of the metal transfer controller inserted between the arc length controller and the current controller (see Figure 7.1), the arc length can still be controlled.

7.4 Discussion and Conclusion

In this chapter metal transfer algorithms are presented. The first of these methods is the fixed frequency pulse scheme, which can be considered as the traditional scheme used in pulsed GMAW. In this method arc length control is performed between the pulses. In the second method a variable frequency is used, but opposite the first method, arc length control is not performed between the pulses. Rather, the arc length control action is performed for each period, that is, the base period plus the pulse period. Such method is used in Migatron's Flex 4000 welding machine. Both the third method and the forth method are based on obtaining a uniform drop size prior to pulse initiation. The goal of such approach is to enhance robustness and be able to lower the pulse energy. The third method is also called the compensation control method, referring to the melting length compensation performed before pulse initiation. The forth method is also called the direct control method, referring to the direct control of the arc length during the base period.

Different pulse shapes are discussed, and four shapes are identified and discussed.

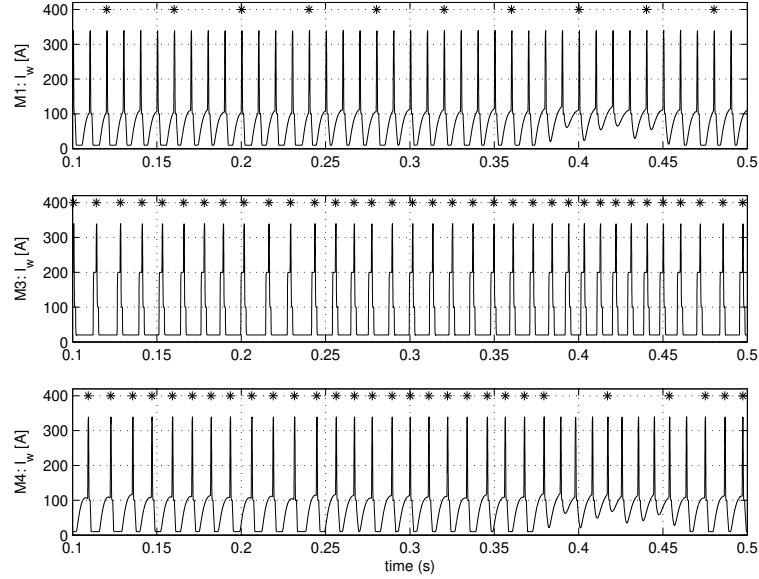


Figure 7.15: Experiment 4. The welding current for the three methods, M1, M3, and M4. The stars on the plots show the drop detachment locations.

These include the rectangular shape, the chair form, the chair form with exponential decrease, and the double pulse shape. Of these shapes the chair shape is used in the simulations.

To test the metal transfer methods a simulation program has been developed, and using the program five experiments were carried out. Basically, the experiments suggest that drop detachments can be performed in spite of disturbances and reference changes, without introducing robustness by increasing the pulse energy. Also, it appears that with respect to drop detachment, the compensation control method is superior when compared to the direct control method. However, the direct control method is able to react directly on arc length disturbances in the base period, and thus, with respect to short circuits this method seems to be the preferred choice.

The main conclusions of this chapter is stated in the following.

- A novel metal transfer control method referred to as the compensation control

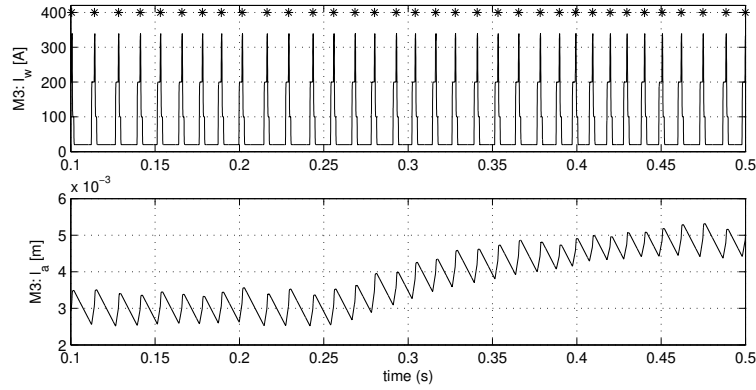


Figure 7.16: Experiment 5. The arc length reference is changed from 0.003 m to 0.005 m during welding using M3, the compensation control method. Detachments also occur during the change of reference.

method has been proposed. The method is based on obtaining a uniform drop size prior to pulse initiation.

- A novel metal transfer control method referred to as the direct control method has been proposed. Like the compensation method, the method is based on obtaining a uniform drop size prior to pulse initiation.
- Simulations shows that drop detachments can be performed in spite of disturbances and reference changes. Also, robustness is introduced without increasing the pulse energy.

Arc Length Minimization

8

In this chapter an arc length minimization algorithm is presented. Arc length minimization is carried out to minimize the heat input and improve the focus ability.

8.1 Optimization by Arc Length Minimization

In Chapter 5, a number of objectives for control of the GMAW process are stated. One objective is to use a minimal amount of the energy in the process, as low energy results in a low heat input into the workpiece. Another objective is to have a minimal arc length during welding.

The average energy developed in the process, basically, depends on the welding current and the arc voltage. In pulsed GMAW, in the base period, the current depends on the control effort from the arc length controller, and, in the pulse period, the current depends on pulse shape. Thus, it is not possible to adjust the current directly to minimize the energy developed in the process. However, the arc voltage, and thereby the energy, can be decreased by decreasing the arc length in the process. Moreover, as described in Chapter 5, a small arc length has another advantage, that is, a small arc is easier to focus during welding. So, to ensure a minimal amount of energy developed in the process, and also, to enhance the ability to focus the arc, a small arc length is needed. However, if the arc length becomes too small, short circuits can be expected. In general, short circuits must be avoided in the process. This is also stated as an objective in Chapter 5.

In Section 8.2 an arc length minimization method, or algorithm, is proposed. In this method the arc length is minimized during welding, towards some lower limit, by adjusting the arc length reference, l_{ar} , to the arc length controller. The lower limit of the arc length depends on the number of short circuits. In general, short

circuits should be avoided, but actually, a few short circuits per time unit are acceptable during welding. Short circuits are detected by the supervision layer in the welding machine, see Chapter 5, by evaluating the terminal voltage, U_t . If this voltage is below some threshold, the supervisory layer draws the conclusion that a short circuit has occurred, and activates some kind of anti short circuit mechanism. For example, the current is increased until the short circuit is no longer present.

8.2 Method for Arc Length Minimization

In this section the arc length minimization method is explained. The aim is to minimize the arc length reference, l_{ar} , fed to the arc length controller, towards some lower limit. We will accept some short circuits per time unit during welding, and thus, the lower limit on the arc length reference will depend on this accepted number of short circuits per time unit.

The number of short circuit per time corresponds to some specified (reference) average time interval between short circuits. Let us denote this reference time interval as T_{scR} . As stated in the former section, the supervisory layer in the welding machine detects and handles short circuits that occurs during welding. Thus, from the supervisory layer the short circuit events can be obtained, and the time between such events can be measured. Let us denote the time between short circuits as T_{sc} .

Now, we want to develop a mechanism which adjust the time between short circuits, T_{sc} , towards the time between short circuits reference, T_{scR} . To solve this problem a PI-controller can be used, see Figure 8.1. The two time intervals T_{scR} and T_{sc} are subtracted, and the error in time, e_{sc} , between the short circuits is obtained. Then this error is fed to the controller which outputs the reference arc length, l_{ar} . The PI-controller contains a proportional term to allow for instant control based on the error, but most importantly, the controller has an integral term. The integral term is important, as it is this term which is able to adjust the arc length towards the lower limit. If no short circuits occur in the process, e_{sc} will be negative, and the integrator will integrate the negative error, and so, continue lowering the arc length until the right number of short circuits per time unit occurs.

The controller is driven by some fixed sample time, T_s . However, the time be-

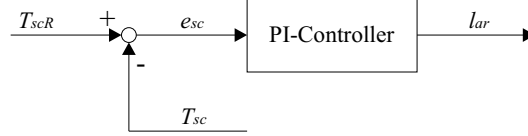


Figure 8.1: The actual time between short circuits and the reference time are compared, and the error is fed to the controller. Output is the arc length reference.

tween the T_{sc} measurements are variable, as T_{sc} , in principle, is updated for each short circuit, and the time between short circuits must be expected to be rather irregular. Therefore, the T_{sc} measurement must be considered.

Instead of using the last obtained time between short circuits, T_{sc} , we rather want to use some kind of average T_{sc} . To obtain such value, T_{sc} is filtered, using the discrete filter stated below. The filtered T_{sc} is denoted y_{sc} .

$$x_{sc}(k+1) = a_{sc}x_{sc}(k) + b_{sc}T_{sc} \quad (8.1)$$

$$y_{sc}(k) = x_{sc}(k) \quad (8.2)$$

In steady state, that means, when T_{sc} is fixed and $y_{sc}(k) = y_{sc}(k+1)$, then T_{sc} must be equal to $y_{sc}(k)$. Otherwise, y_{sc} would not be an average. So, the relationship between the constants must be $a_{sc} = 1 - b_{sc}$. The input to the filter is the time T_{sc} , which is generated for every short circuit event, and let us denote a short circuit event by E_{sc} . So, T_{sc} can be expressed as below. t_{sc} is the 'running' time variable which is reset at every short circuit.

$$\text{if } E_{sc}, \text{ then update with } T_{sc} = t_{sc} \quad (8.3)$$

Thus, the filter is updated for every short circuit. However, suppose that no short circuit occurs, then the filter is never updated. So, for example, if $y_{sc}(k)$ is less than $T_{scR}(k)$, but afterwards, no short circuits occurs. Then, the integral term of the PI-controller will continue integrating a negative error ($e_{sc} = y_{sc}(k) - T_{scR}$), in spite of the fact that t_{sc} (the 'running' time variable) could be much higher than $y_{sc}(k)$. To avoid such situation, the filter is updated at some frequency f_k when t_{sc} exceeds the reference T_{scR} . Thus, in addition to (8.3), the filter is updated as stated below. In Figure 8.2, configuration of the arc length minimization algorithm

is shown together with the process and the control systems. Note, that based on terminal voltage measurements, and current measurements, the supervisory layer generates the short circuit events used in the algorithm.

$$\text{if } t_{sc} > T_{sc}, \text{ then update } T_{sc} \text{ with frequency } f_k : T_{sc} = t_{sc} \quad (8.4)$$

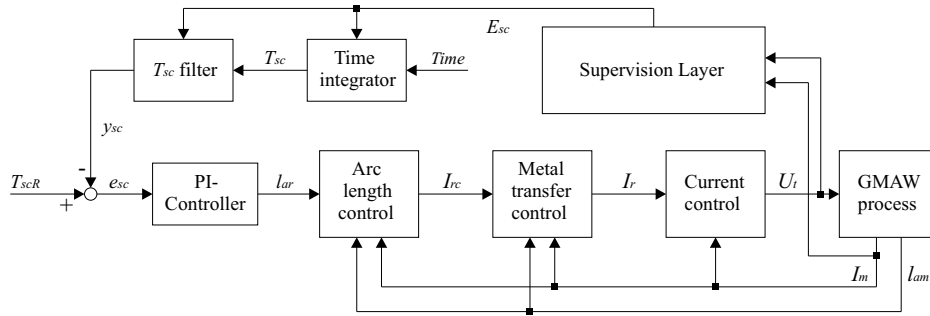


Figure 8.2: The GMAW control system including arc length minimization.

Notice, that to limit the number of short circuits in the process, a large value for T_{scR} should be chosen, but on the other hand, T_{scR} should not be chosen too large, as this would limit the performance of the arc minimization algorithm. Another approach is to set T_{scR} equal to time between the pulses. In this way, a short circuit would occur for every pulse, and probably at drop detachment. Such short circuits do not have any significant negative effect on the weld quality, because the time between the start of the short circuit to the end of the short circuit is rather small.

8.3 Simulations

The arc length minimization algorithm described in the former section has been implemented and tested in a simulation program developed in Simulink. The algorithm has been implemented as illustrated in Figure 8.2. In this section, a number of plots are presented, illustrating the behavior of the arc length minimization algorithm.

The developed simulation program does not include a model describing the behavior of a short circuit, but such model is not necessary for testing the arc length minimization algorithm. In the simulation program, to test the behavior of the algorithm, negative (artificial) pulses added to the arc length measurements, which is low pass filtered to remove the ripple because of drop oscillations. Afterwards the result is forwarded to the supervision layer instead of U_t , see Figure 8.2. In the supervision layer, a short circuit event is generated if the signal, that is, the arc length measurement plus the pulses, is less than some lower boundary. Two pulse trains are used, both fixed in amplitude and frequency. See Figure 8.3.

- The lower boundary (short circuit boundary): 0.002 m.
- Pulse train A data: Period = 0.4 s, Amplitude = -0.0008, Pulse width = 5%, Phase delay = 0.3 s, Bias = 0.
- Pulse train B data: Period = 0.6 s, Amplitude = -0.0004, Pulse width = 5%, Phase delay = 0.5 s, Bias = 0.

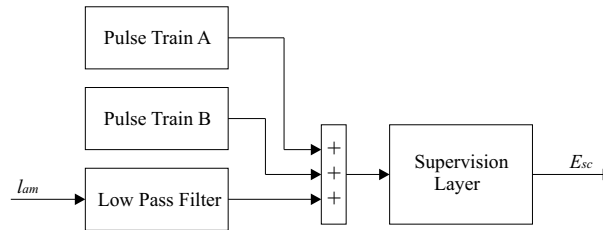


Figure 8.3: Generation of short circuit events for the simulation program.

Initially, the arc length reference, l_{ar} , is set to 0.003 m, and moreover, T_{scR} , the time between short circuits reference, is set to 0.5 s. Using the pulses stated above, it can be expected that the arc length reference, l_{ar} , is adjusted by the arc length minimization algorithm towards some value between 0.0024 m and 0.0028 m.

In the first plot of Figure 8.4, the internal 'running' time variable t_{sc} in the time integrator block is shown, see Figure 8.2. At each short circuit, the time between short circuit measurement, T_{sc} , is updated and the time variable t_{sc} is reset to zero. Also, in Figure 8.4, the filtered time variable y_{sc} is shown. As illustrated in Figure 8.2, this value is subtracted from the reference T_{scR} , and the result is input to the controller. The filter, generating y_{sc} , is updated for every short circuit, but also, by some frequency f_k , if t_{sc} becomes greater than T_{scR} . In Figure 8.4, this can be

seen at the second plot. For example, from around 1.1 s to 2.3 s, no short circuit takes place, but at $t_{sc} = 0.5$ s, and until t_{sc} is reset, the filter becomes updated at some frequency. In the simulation program the frequency f_k is chosen to 5 Hz.

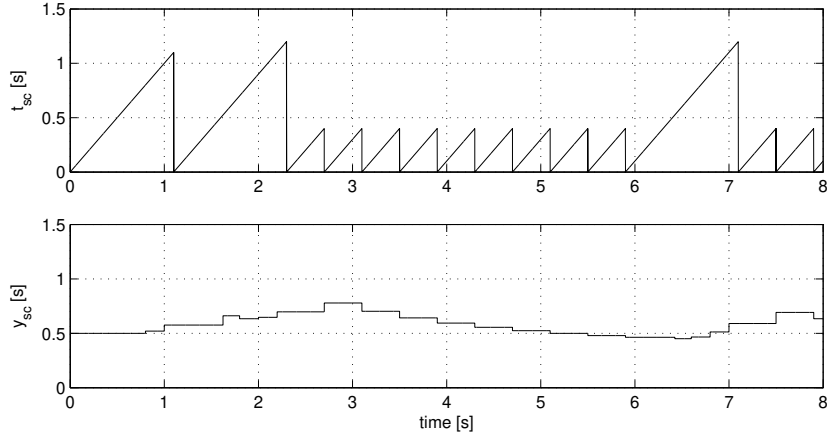


Figure 8.4: First plot: The internal time variable t_{sc} in the time integrator. Second plot: the filtered time between short circuits.

In the first plot of Figure 8.5, the short circuit events are shown, and in the second plot all events are shown. This means, the short circuit events and the events generated when t_{sc} becomes greater than T_{scR} , to ensure that the filter is updated.

In Figure 8.6, the arc length reference, l_{ar} , which is calculated by the PI-controller is shown. The initial arc length reference is 0.003 m, but no short circuit happens at that value. The controller reacts by decreasing the arc length until short circuits starts to appear. From the y_{sc} plot in Figure 8.4, it can be seen that the filtered, or average, time between short circuits approach the reference $T_{scR} = 0.5$ s. As predicted, using the pulses as explained before, the arc length minimization algorithm adjust the arc length reference, l_{ar} , to some value between 0.0024 m and 0.0028 m. The arc length reference should lie between these values, as the short circuit is set to 0.002 m, and amplitude of the two pulse trains are 0.0004 m and 0.0008 m, respectively.

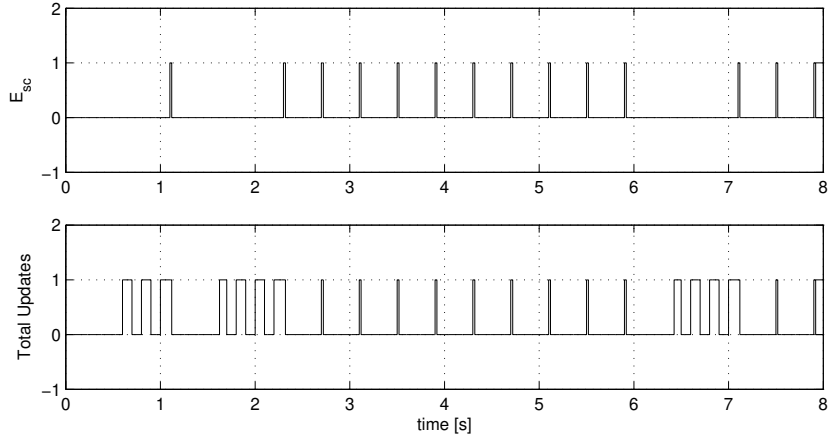


Figure 8.5: First plot: The short circuit events. Second plot: The filter is updated at the rising edges.

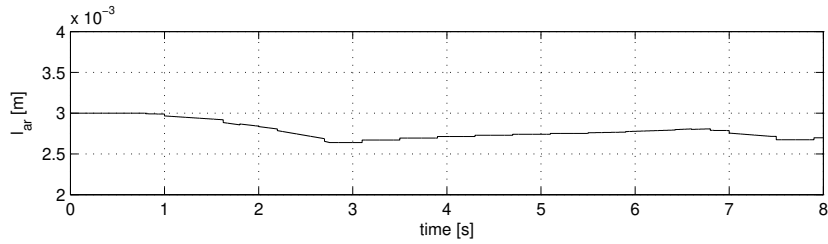


Figure 8.6: The arc length reference which is forwarded to the arc length controller.

8.4 Discussion and Conclusion

In this chapter a method for arc length minimization is proposed. In this method a given number of short circuits per time unit are accepted. This number, which is expressed as a time between short circuits, becomes a reference input to the arc length minimization algorithm. The reference input and the measured time between short circuits are subtracted, and a PI-controller adjusts the arc length reference which is input to the arc length controller.

To test the arc length minimization algorithm a simulation program was developed. Results from simulation suggested that the arc length minimization algorithm was able to minimize the arc length as desired.

Part III

Conclusion

Conclusions and Future Work

9

In this chapter the final conclusions of the thesis are presented, and moreover, possible future work are considered.

9.1 Conclusion

In this thesis control of the gas metal arc welding (GMAW) process is addressed. The GMAW process is explained in Chapter 2, and in Chapter 3 a model of the GMAW process is presented. Based on the model, presented in Chapter 3, a number of simulation programs have been developed for testing and illustrating the algorithms developed in this thesis. Simulations play a significant role in the thesis, as a real experimental welding facility has not been available during the work. Thus, tests and validations have to rely on simulations.

In Chapter 3 a steady state model of the electrode melting rate is presented and included in the overall model. However, such steady state model does not take the transient phase for melting rate changes into account, and therefore, to obtain a better melting rate model, a dynamic melting rate model is developed in Chapter 4. In fact, two models are developed. In the first model, referred to as the full dynamic melting rate model, the electrode is partitioned into many small elements to describe the temperature of the electrode. This approach results in a system having a rather high order, that is, a large number of differential equations. To reduce the number of calculations needed to calculate a value for the melting rate, the order of the full dynamic melting rate model is reduced. This results in the second dynamic melting rate model, referred to as the reduced dynamic melting rate model. Especially, in the transient phase of a step response, simulations showed good agreement between the full dynamic melting rate model and the reduced melting rate model.

In Chapter 1 the overall objective of the thesis is to optimize the control algorithms for the manual pulsed GMAW welding process, with the aim of enhancing the quality of welded joints. To approach this problem four specific objectives are derived in Chapter 5, and also, different configurations for controlling the GMAW process are considered. The specific objectives concerns minimal energy, minimal arc length, avoiding short circuits, and obtaining one drop per pulse (ODPP). The control structure, or control topology, which is chosen is a cascade coupled system. In this cascade coupled system an inner current controller controls the current dynamic of the process. The reference input to the inner current controller is a reference current from a metal transfer controller, which structurally is driven by an input from an arc length controller.

In Chapter 6 a nonlinear arc length controller is derived. Arc length control is considered as it is important to be able to keep a steady arc length in spite of disturbances. In manual welding a potentially significant disturbance arises from the operator which moves the welding pistol along the welding path. The nonlinear controller is a feedback linearization based controller, and for development of the controller the inner current controller is considered as a part of the arc length process. Also, equations relating to the drop dynamics, which is described in Chapter 3, is left out as such equations are not relevant for arc length control. Stabilization, tracking, uncertainties, and performance are considered for the arc length controller, and also, to test the controller a number of experiments are carried out using a developed simulation program. The experiments show that the controller is able to control the arc length in spite of a set of disturbances which can be expected in a real welding application. With respect to the specific objectives, presented in Chapter 5, the nonlinear arc length controller does not directly addresses any of those objectives. However, to avoid too many short circuits a good performing arc length controller must be preferred, and moreover, arc length control must be considered as a fundamental part of any GMAW controller.

In Chapter 7 metal transfer control is considered, and a novel approach is presented. The approach is based on obtaining a uniform drop size prior to pulse initiation. The goal of this approach is to enhance robustness and be able to lower the pulse energy. Two methods using this approach are presented. One of these methods is called the compensation control method, referring to the melting length compensation performed before pulse initiation. The other method is called the direct control method, referring to the direct control of the arc length during the

base period. Simulations suggested that drop detachments could be performed in spite of disturbances and reference changes, and without introducing robustness by increasing the pulse energy. Two of the objectives referred to in Chapter 5 are considered, and these are the minimal energy objective and the one drop per pulse objective. Minimal energy is obtained as robustness is obtained through the uniform drop size, and not through a high pulse energy. Moreover, as the energy is minimal for drop detachment, several drop detachment per pulse is unlikely. Thus, the one drop per pulse objective is fulfilled.

In Chapter 8 a method for arc length minimization is proposed. Thus, this method addresses the specific objective stated in Chapter 5 about having a minimal arc length. In arc length minimization method a PI-controller outputs an arc length reference which is used as input to the arc length controller. Basically, the minimal arc length is found by lowering the arc length reference until a desired number of short circuits per time unit are present. Thus, in spite of the specific objective about avoiding short circuits, a given number of short circuits are allowed in this approach. Simulation suggested that the arc length minimization algorithm was able to minimize the arc length as desired.

In the following the main conclusions and contributions of this thesis are stated.

- A GMAW model is presented which can be used for simulation and development of control algorithms.
- An expression for the electromagnetic force can be found in the literature. The calculations leading to this expression are included in the thesis.
- A dynamic melting rate model suited for simulation has been developed. The model is referred to as the full dynamic melting rate model.
- A dynamic melting rate model suited for control has been developed. The model is referred to as the reduced dynamic melting rate model.
- A general GMAW control system is presented in the thesis. The control system is structured as a cascade coupled system having inner current controller, followed by an outer metal transfer controller, and afterwards, an outer arc length controller.
- A nonlinear controller has been developed. For this controller no operation point needs to be selected, and also, the controller is able to handle the nonlinearities of the process.
- It is shown how stability of the arc length controller can be analyzed given a set of uncertainties.

- It is shown how the arc length controller can be tuned given a set of performance criteria.
- A novel metal transfer method referred to as the compensation control method has been proposed. The method is based on obtaining a uniform drop size prior to pulse initiation.
- A novel metal transfer method referred to as the direct control method has been proposed. Like the compensation method, the method is based on obtaining a uniform drop size prior to pulse initiation.
- A method for arc length minimization has been proposed.

9.2 Future Work

In this thesis arc length control, metal transfer control, and arc length minimization has been considered. Also, two dynamic melting rate models have been proposed. However, the work has only been tested in simulation programs. The mathematical model presented in this thesis of the GMAW process is not precise, and thus, the simulation programs are not precise as these are based on the model. Therefore, implementation and validation in a real welding test system is needed, and such test system must include a high speed camera to be able to observe behavior of the drop during welding. If such test system is available the following could be investigated.

- Data from the GMAW model could be compared with data obtained from a real welding process. In this way it is possible to investigate model uncertainty.
- The melting rate calculated by the full dynamic melting rate model should be compared with the measured melting rate in a real welding system. This means that transients in the real application must be measured, which is possible with a camera. Comparison of the real melting rate and the calculated melting rate makes validation of the full dynamic melting rate model possible. Afterwards, the reduced model can be tuned to give a similar output as the full dynamic melting rate model.
- The nonlinear arc length controller should be implemented and tested in a real welding system. For example performance of the GMAW process controlled by the controller could be investigated.
- Both metal transfer control methods should be implemented and tested in a real welding system. It must be verified in practice that a uniform drop size provides robustness with respect to drop detachment.

- The arc length minimization algorithm should be implemented and tested in a real welding system. It must be investigated if the proposed approach is feasible in practice. Also, the method might be improved by a categorization of the short circuits. Short circuits which have a relative small duration are tolerable, but long duration short circuits must be completely avoided.
- Several of the control algorithms developed in this thesis rely on an arc voltage model. However, the model used in this thesis is not accurate. For example, for low currents the arc voltage increases, and this is not accounted for in the model. Thus, the effect of having an inaccurate model should be investigated in greater detail, and also, a more accurate model could be developed.

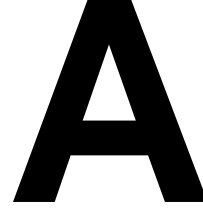
On a longer perspective a lot could be done with respect to GMAW control. Today, to achieve a high quality weld, the machine settings have to be adjusted by an experienced operator, and also, the task of performing the weld is very difficult. The adjustment of the machine could be performed by the machine itself if more "intelligence" are included on the machine. Also, more machine "intelligence" could improve the quality and ease the task of performing a weld. Such improved "intelligence" much be based on further research, and especially, the author believes that a model based approach to the problem is useful. In general, this is also the approach used in this thesis. Below some further research topics or suggestions are mentioned.

- Drop detachment detection using current measurements and terminal voltage measurements. Drop detachments can be detected if an voltage close the arc is measured. Otherwise, it is difficult. However, if it is possible the metal transfer control algorithms can be improved, as it the melting length can measure from the actual drop detachment event.
- Automatic tuning or estimation of parameters. For example, the melting rate parameters can be estimated during welding. A melting rate model is used for both arc length control and for metal transfer control, and thus, these algorithms can be improved.
- The general control structure used in this thesis should be extended if the electrode speed is considered as a controllable input to the process. An obvious choice would be to extend the cascade coupled structure with another outer controller. The electrode speed corresponds to the average current, and thus, the energy or heat input into the workpiece can be controlled.

Part IV

Appendices

Maxwell Stresses



In [28, Chapter 3], the electromagnetic force (or Maxwell stress) acting on a volume element in the drop is expressed as

$$\mathbf{F}_{em} = \mathbf{J} \times \mathbf{B} = \frac{1}{\mu} (\nabla \times \mathbf{B}) \times \mathbf{B} \Rightarrow \quad (\text{A.1})$$

$$\mathbf{F}_{em} = -\frac{1}{2\mu} \nabla(B^2) + \frac{1}{\mu} (\mathbf{B} \bullet \nabla) \mathbf{B} \quad (\text{A.2})$$

Equation (A.2) contains two terms. The first term is given by the

$$Q_1 = -\frac{1}{2\mu} \nabla(B^2) \quad (\text{A.3})$$

The second term is given by

$$Q_2 = \frac{1}{\mu} (\mathbf{B} \bullet \nabla) \mathbf{B} \quad (\text{A.4})$$

For a current parallel to the electrode the first term generates an inward acting force, while the second term generates a rotational force within the drop. For a converging or a diverging current the first term also contains a axial component, however, this is not the case for the second term. This will be illustrated in the following.

A downward current induces a magnetic field (B-field) around the path of the current. In any point within the drop, at any given time, the B-field can be described by a B-vector, \mathbf{B} . The normal, \mathbf{I}_n , to the current path, the B-vector in a small element, and the position of the small element are shown in Figure A.1.

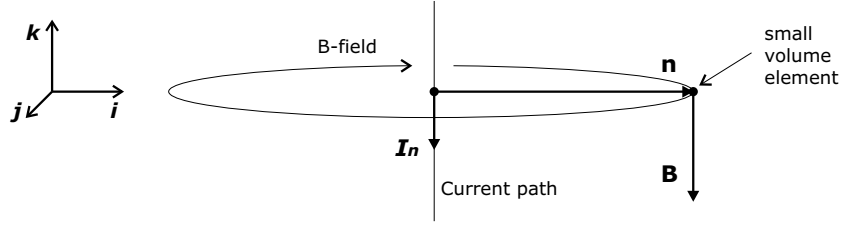


Figure A.1: The current normal and the B-field vector for a small element within the drop.

The location of the small element is given by \mathbf{h} , and the following definitions and formulas are used

$$B = \frac{\mu I}{2\pi r} \quad (\text{A.5})$$

$$\mathbf{B} = \frac{\mu I}{2\pi r} (\mathbf{I}_n \times \mathbf{h}) \quad (\text{A.6})$$

$$A = \frac{\mu I}{2\pi} \quad (\text{A.7})$$

$$\mathbf{I} = \mathbf{I}_n I \quad (\text{A.8})$$

$$r^2 = x^2 + y^2 \mathbf{I}_n = (1, 0, 0) \quad (\text{A.9})$$

$$\mathbf{h} = (0, 0, -1) \quad (\text{A.10})$$

$$(\text{A.11})$$

Now, let us look at the second term, Q_2 .

$$Q_2 = \frac{1}{\mu} (\mathbf{B} \cdot \nabla) \mathbf{B} \quad (\text{A.12})$$

$$= \frac{1}{\mu} ((0\mathbf{i} - A\frac{1}{r}\mathbf{j} + 0\mathbf{k}) \cdot (\frac{\partial}{\partial x}\mathbf{i} + \frac{\partial}{\partial y}\mathbf{j} + \frac{\partial}{\partial z}\mathbf{k})) (0\mathbf{i} - A\frac{1}{r}\mathbf{j} + 0\mathbf{k}) \quad (\text{A.13})$$

$$= \frac{1}{\mu} A \frac{1}{r} \frac{\partial}{\partial y} (-A\frac{1}{r}\mathbf{j}) \quad (\text{A.14})$$

$$= \frac{1}{\mu} A^2 \frac{1}{r} \frac{\partial}{\partial y} (\frac{1}{r}) \mathbf{j} \quad (\text{A.15})$$

This force acts parallel to the B-field. One can see that a diverging or converging current path will not change the orientation of the vector. Thus, it will still be rotational, even though it will change in magnitude along the z-axis.

Now, let us look at the first term, Q_1 , still using the formulas and definitions above.

$$\mathbf{Q}_1 = -\frac{1}{2\mu} \nabla(B^2) \quad (\text{A.16})$$

$$= -\frac{1}{2\mu} A^2 \nabla \frac{1}{r^2} \quad (\text{A.17})$$

$$= -\frac{1}{2\mu} A^2 \left(\frac{-2x}{r^4} \mathbf{i} + \frac{-2y}{r^4} \mathbf{j} \right) \quad (\text{A.18})$$

This vector points inward, thus, being an inward component to the force acting on the element. However, for a diverging or a converging current path the B-field will also be dependent of the z-direction, thus, causing an axial force.

The Electromagnetic Force

B

In [5], in [28, Chapter 3], and in [27] a function expressing the total electromagnetic force acting on a drop in GMAW was presented. In [5] and in [27] this function was rewritten, given a number of assumptions, into a much simpler form. A form that can be used for direct calculation of the electromagnetic force. The derivations in the following can viewed as a supplement to the derivations found in [5] and in [27].

The expression for the total electromagnetic force vector, presented in [28, Chapter 3], is a surface integral of all Maxwell stresses acting on the drop.

$$\mathbf{F}_{m,\text{total}} = \int_{V_d} \mathbf{f}_m dv = \int_{S_d} \frac{B^2}{2\mu} (-\mathbf{n} ds) \quad (\text{B.1})$$

\mathbf{f}_m is the electromagnetic stress vector (or Maxwell stress vector), V_d represents the volume of the drop, S_d represents the surface of the drop, B is the magnitude of the B-field, and \mathbf{n} is the normal vector to the surface.

As current flows through the drop a magnetic field is established. The intensity \mathbf{H} of this field can be expressed by Ampere's Law.

$$\mathbf{H} = \frac{I(r, z)}{2\pi r} \mathbf{u}_\phi \quad (\text{B.2})$$

where $I(r, z)$ is the current bounded by a hoop which passes through the point (r, z) . \mathbf{u}_ϕ is a unit vector on the hoop, and r is the radius.

Let us define the vector $\boldsymbol{\tau}$ from equation (B.1). In [27] this vector is referred to as a traction vector. The traction vector and the magnitude of the traction vector is given by

$$\boldsymbol{\tau} = \frac{1}{2} \frac{B^2}{\mu} = \frac{1}{2} \mu H^2 (-\mathbf{n}) \quad (\text{B.3})$$

$$\tau = |\boldsymbol{\tau}| = \frac{B^2}{2\mu} = \frac{\mu H^2}{2} \quad (\text{B.4})$$

Using equation (B.2) the magnitude of the traction vector can be written as

$$\tau = \frac{\mu}{8\pi^2} \frac{I(r, z)^2}{r^2} \quad (\text{B.5})$$

The z-directed component of traction vector, τ , must be integrated on the drop surface to obtain an expression for the total electromagnetic force in the z-direction, denoted f_z .

$$f_z = \int_Q \tau_z da + \int_P \tau_z da \quad (\text{B.6})$$

The z-direction and the surfaces Q and P , from equation (B.6), are all shown in Figure B.1.

The z-directed component of the traction vector for the surface Q is given by the expression below. Also, see Figure B.2.

$$\tau_z = -\frac{dr}{du} \tau \quad (\text{B.7})$$

The differential element da can be expressed as a circle that has a thickness of du and a radius of $r(u)$.

$$da = 2\pi r(u) du \quad (\text{B.8})$$

The z-directed component of the traction vector for the surface P is given by the expression below. Also, see Figure B.2.

$$\tau_z = \frac{dr}{ds} \tau \quad (\text{B.9})$$

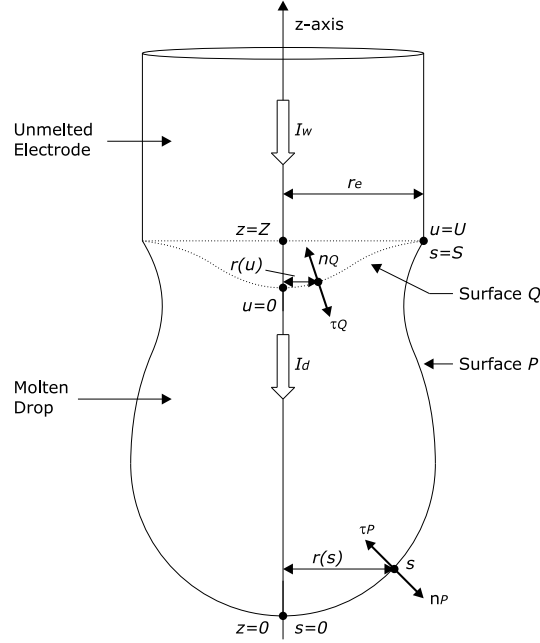


Figure B.1: A typical drop in GMAW. Variables and vectors used in the derivations are shown.

The differential element da can be expressed as a circle that has a thickness of ds and a radius of $r(s)$.

$$da = 2\pi r(s)ds \quad (\text{B.10})$$

Figure B.1 suggest two different currents. A current flowing in the solid electrode and a current flowing through the drop. If some current flows directly from the solid electrode, then $I_w > I_d$. Otherwise, the two currents will be equal. In the following it is assumed that $I_w = I_d = I$. Now, f_z can be written as

$$f_z = \int_Q \tau_z da + \int_P \tau_z da \quad (\text{B.11})$$

$$f_z = \int_0^U \left(-\frac{dr}{du}\tau\right)(2\pi r(u)du) + \int_0^S \left(\frac{dr}{ds}\tau\right)(2\pi r(s)ds) \quad (\text{B.12})$$

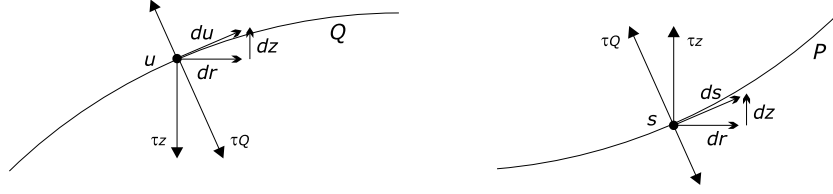


Figure B.2: The figure shows the traction vectors for surface Q and P , respectively. Moreover the z -directed components are shown.

$$f_z = \int_0^U \left(-\frac{dr}{du} \frac{\mu}{8\pi^2} \frac{I(u)^2}{r(u)^2} \right) (2\pi r(u) du) + \int_0^S \left(\frac{dr}{ds} \frac{\mu}{8\pi^2} \frac{I(s)^2}{r(s)^2} \right) (2\pi r(s) ds) \quad (\text{B.13})$$

$$f_z = -\pi\mu \int_0^U \left(\frac{I(u)}{2\pi} \right)^2 \frac{dr}{du} \frac{du}{r(u)} + \pi\mu \int_0^S \left(\frac{I(s)}{2\pi} \right)^2 \frac{dr}{ds} \frac{ds}{r(s)} \quad (\text{B.14})$$

Above, the (r, z) dependence has been substituted by dependence of u and s , respectively. Moreover U and S denote the end points of the curves representing the cross section shape of, respectively, the Q -surface and the P -surface. See Figure B.1.

The currents $I(u)$ and $I(s)$ can be expressed as stated below where $j(\cdot)$ denotes the density of the current.

$$I(u) = \int_{\text{Area}(u)} j(a) da = \int_0^u j(u') 2\pi r(u') du' \quad (\text{B.15})$$

$$I(s) = \int_{\text{Area}(s)} j(a) da = \int_0^s j(s') 2\pi r(s') ds' \quad (\text{B.16})$$

Using these expressions we have the following equation for the total electromagnetic force in the z -direction.

$$f_z = -\pi\mu \int_0^U \left(\int_0^u j(u') r(u') du' \right)^2 \frac{dr}{du} \frac{du}{r(u)} + \pi\mu \int_0^S \left(\int_0^s j(s') r(s') ds' \right)^2 \frac{dr}{ds} \frac{ds}{r(s)} \quad (\text{B.17})$$

B.1 The drop and solid electrode surface

It is assumed that the liquid drop has a form as illustrated in Figure B.1. We observe that the upper surface, Q , is almost cone shaped, and therefore, the surface is modelled as such. Moreover, in the following, it is assumed that the current density is uniform, such that $j(u) = j$.

Let us make the following definitions

$$r(u) = \cos(\phi_{\text{cone}})u = ku \quad (\text{B.18})$$

$$\frac{dr(u)}{du} = k \quad (\text{B.19})$$

From this it is possible to express the total current, I_c , through the cone by

$$I = jA_{\text{cone}} = j\pi r(U)U = j\frac{\pi r^2(U)}{k} \quad (\text{B.20})$$

Now, an expression for the Q-component of the electromagnetic force f_z can be derived.

$$\begin{aligned} f_{z,Q} &= -\pi\mu \int_0^U \left(\int_0^u j(u')r(u')du' \right)^2 \frac{dr(u)}{du} \frac{du}{r(u)} \Rightarrow \\ f_{z,Q} &= -\pi\mu \int_0^U \left(\int_0^u jku'du' \right)^2 k \frac{du}{ku} \Rightarrow \\ f_{z,Q} &= -\pi\mu \int_0^U j^2 k^2 \left(\frac{1}{2} [(u')^2]_0^u \right)^2 k \frac{du}{ku} \Rightarrow \\ f_{z,Q} &= -\pi\mu \int_0^U j^2 k^2 \frac{1}{4} u^4 k \frac{du}{ku} \Rightarrow \\ f_{z,Q} &= -\pi\mu \int_0^U j^2 k^2 \frac{1}{4} u^3 du \Rightarrow \\ f_{z,Q} &= -\pi\mu j^2 k^2 \frac{1}{4} \left[\frac{1}{4} u^4 \right]_0^U \Rightarrow \\ f_{z,Q} &= -\pi\mu j^2 k^2 \frac{1}{16} U^4 \Rightarrow \\ f_{z,Q} &= -\pi\mu j^2 k^2 \frac{1}{16} \frac{r(U)^4}{k^4} \Rightarrow \end{aligned}$$

$$f_{z,Q} = -\frac{\mu I^2}{16\pi} \quad (\text{B.21})$$

B.2 The drop and gas surface

Now, let us look at the surface P . Suppose $j(s)$ is defined over the interval $[0, S]$ such that $j(s) = 0$ for $s_1 \leq s \leq s_2$ and is arbitrary elsewhere. Moreover, s_1, s_2 are such that $0 \leq s_1 < s_2 \leq S$, but otherwise arbitrary, then the contribution to the electromagnetic force from the outer surface is given by

$$\begin{aligned} f_{z,P} = & \pi\mu \int_0^{s_1} \left(\int_0^s j(s')r(s')ds' \right)^2 \frac{dr}{ds} \frac{ds}{r(s)} \\ & + \pi\mu \int_{s_1}^{s_2} \left(\int_0^{s_1} j(s')r(s')ds' + \int_{s_1}^s j(s')r(s')ds' \right)^2 \frac{dr}{ds} \frac{ds}{r(s)} \\ & + \pi\mu \int_{s_2}^S \left(\int_0^{s_1} j(s')r(s')ds' + \int_{s_1}^{s_2} j(s')r(s')ds' \right. \\ & \quad \left. + \int_{s_2}^s j(s')r(s')ds' \right)^2 \frac{dr}{ds} \frac{ds}{r(s)} \end{aligned} \quad (\text{B.22})$$

$$(\text{B.23})$$

As defined, $j = 0$ in $[s_1, s_2]$, and therefore, the terms originating from this interval vanishes in the above expression. Thus, the electromagnetic force is independent of the surface profile of the region where the surface current density equals zero. This is also stated in [5].

$$\begin{aligned} f_{z,P} = & \pi\mu \int_0^{s_1} \left(\int_0^s j(s')r(s')ds' \right)^2 \frac{dr}{ds} \frac{ds}{r(s)} \\ & + \pi\mu \int_{s_1}^{s_2} \left(\int_0^{s_1} j(s')r(s')ds' \right)^2 \frac{dr}{ds} \frac{ds}{r(s)} \\ & + \pi\mu \int_{s_2}^S \left(\int_0^{s_1} j(s')r(s')ds' + \int_{s_2}^s j(s')r(s')ds' \right)^2 \frac{dr}{ds} \frac{ds}{r(s)} \end{aligned} \quad (\text{B.24})$$

The second term (the non-conducting part) can be written as

$$f_{z,P,\text{non-conducting}} = \pi\mu \int_{s_1}^{s_2} \left(\int_0^{s_1} j(s')r(s')ds' \right)^2 \frac{dr}{ds} \frac{ds}{r(s)}$$

$$\begin{aligned}
&= \pi\mu \left(\int_0^{s_1} j(s')r(s')ds' \right)^2 \int_{s_1}^{s_2} \frac{dr}{ds} \frac{ds}{r(s)} \\
&= \pi\mu \left(\frac{1}{2\pi} I_{s1} \right)^2 \int_{s_1}^{s_2} \frac{dr}{ds} \frac{ds}{r(s)} \\
&= \frac{\mu}{4\pi} I_{s1}^2 \int_{r(s_1)}^{r(s_2)} \frac{1}{t} dt \quad , \quad \text{where } t = r(s) \text{ and } \frac{dr(s)}{ds} = \frac{dt}{ds} \\
&= \frac{\mu}{4\pi} I_{s1}^2 [\ln |t|]_{r(s_1)}^{r(s_2)} \\
&= \frac{\mu}{4\pi} I_{s1}^2 \ln \left| \frac{r(s_2)}{r(s_1)} \right| \tag{B.25}
\end{aligned}$$

where

$$I_{s1} = \int_{\text{Area}(s1)} j(a)da = \int_0^{s_1} j(s')2\pi r(s')ds' \tag{B.26}$$

Now, assume that the outer surface P can be divided into, only, two parts. A conducting lower part and a non-conducting upper part. At the lower part the current density is different from zero while it equals zero for the upper part. This gives a lower force $f_{z,P1}$ and an upper force $f_{z,P2}$.

The upper part is given by

$$f_{z,P2} = \frac{\mu}{4\pi} I_{s1}^2 \ln \left| \frac{r_e}{a \sin(\Phi)} \right| \tag{B.27}$$

where r_e is the radius of the electrode and Φ is the angle describing the size of the conducting area. See Figure B.3.

Next, the lower part can be calculated. First, from Figure B.3, we see that

$$r(s) = a \sin(\phi) \quad , \quad s = a\phi \tag{B.28}$$

$$\frac{dr(s)}{ds} = a \frac{d\phi}{ds} \frac{d \sin(\phi)}{d\phi} = \cos(\phi) \tag{B.29}$$

and we see that

$$I = jA_{\text{truncated-sphere}} = jA_S$$

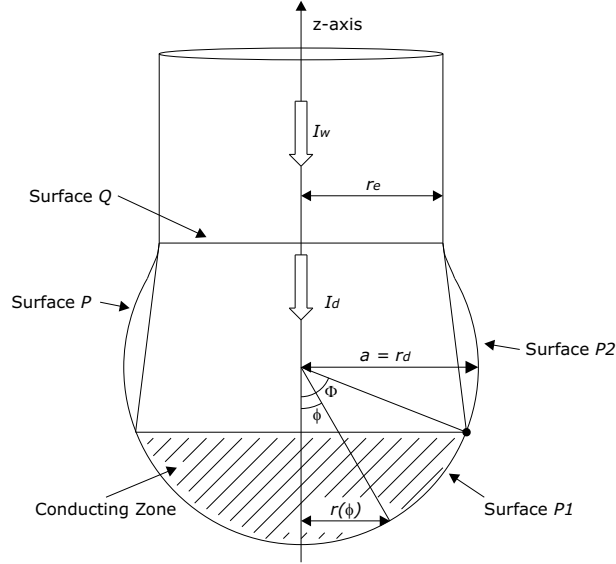


Figure B.3: Surfaces and the conducting area.

$$\begin{aligned}
 &= j \int_0^S 2\pi r(s) ds = j \int_0^S 2\pi a \sin\left(\frac{s}{a}\right) ds \\
 &= j2\pi a \left[-a \cos\left(\frac{s}{a}\right) \right]_0^S = j2\pi a^2 \left(1 - \cos\frac{S}{a}\right) \quad (\text{B.30})
 \end{aligned}$$

Now, we have

$$\begin{aligned}
 f_{z,P1} &= \pi\mu \int_0^{S_1} \left(\int_0^s j(s')r(s')ds' \right)^2 \frac{dr(s)}{ds} \frac{ds}{r(s)} \Rightarrow \\
 f_{z,P1} &= \pi\mu \int_0^{S_1} \left(\int_0^s \frac{I}{2\pi a^2(1 - \cos(\frac{s}{a}))} r(s')ds' \right)^2 \frac{dr(s)}{ds} \frac{ds}{r(s)} \Rightarrow \\
 f_{z,P1} &= \pi\mu \int_0^{S_1} \left(\int_0^s \frac{I}{2\pi a^2(1 - \cos(\frac{s}{a}))} a \sin(\frac{s'}{a}) ds' \right)^2 \cos(\frac{s}{a}) \frac{1}{a \sin(\frac{s}{a})} ds \Rightarrow \\
 f_{z,P1} &= \pi\mu \int_0^\Phi \left(\int_0^\phi \frac{I}{2\pi a^2(1 - \cos(\Phi))} a^2 \sin(\phi') d\phi' \right)^2 \frac{\cos(\phi)}{\sin(\phi)} d\phi \Rightarrow \\
 f_{z,P1} &= K \int_0^\Phi \left(\int_0^\phi \sin(\phi') d\phi' \right)^2 \frac{\cos(\phi)}{\sin(\phi)} d\phi \Rightarrow
 \end{aligned}$$

$$\begin{aligned}
 f_{z,P1} &= K \int_0^\Phi \left([-\cos(\phi')]_0^\phi \right)^2 \frac{\cos(\phi)}{\sin(\phi)} d\phi \Rightarrow \\
 f_{z,P1} &= K \int_0^\Phi (1 - \cos(\phi))^2 \frac{\cos(\phi)}{\sin(\phi)} d\phi
 \end{aligned} \tag{B.31}$$

where

$$K = \mu \frac{\mu I^2}{4\pi(1 - \cos(\Phi))^2} \tag{B.32}$$

The following substitution is used

$$x = 1 - \cos(\phi) \quad , \quad \frac{dx}{d\phi} = \sin(\phi) \tag{B.33}$$

$$\begin{aligned}
 \sin^2(\phi) &= 1 - \cos^2(\phi) \\
 &= 1 - (1 - x)^2 = 1 - (1 + x^2 - 2x) = x(2 - x)
 \end{aligned} \tag{B.34}$$

We get

$$\begin{aligned}
 f_{z,P1} &= K \int_0^{1-\cos(\Phi)} x^2 \frac{1-x}{x(2-x)} dx \Rightarrow \\
 f_{z,P1} &= K \int_0^{1-\cos(\Phi)} \frac{x - x^2}{2-x} dx
 \end{aligned} \tag{B.35}$$

and we use the following substitution

$$y = 2 - x \quad , \quad \frac{dy}{dx} = -1 \tag{B.36}$$

$$x = 2 - y \quad , \quad x^2 = (2 - y)^2 = y^2 - 4y + 4 \tag{B.37}$$

and we get

$$\begin{aligned}
 f_{z,P1} &= K \int_2^{1+\cos(\Phi)} \frac{(2-y) - (y^2 - 4y + 4)}{y} (-dy) \Rightarrow \\
 f_{z,P1} &= K \int_2^{1+\cos(\Phi)} \frac{-y^2 + 3y - 2}{y} (-dy) \Rightarrow
 \end{aligned}$$

$$\begin{aligned}
 f_{z,P1} &= K \int_2^{1+\cos(\Phi)} \left(y - 3 + \frac{2}{y}\right) dy \Rightarrow \\
 f_{z,P1} &= K \left(\frac{1}{2} [y^2]_2^{1+\cos(\Phi)} - 3[y]_2^{1+\cos(\Phi)} + 2[\ln|y|]_2^{1+\cos(\Phi)} \right) \Rightarrow \\
 f_{z,P1} &= K \left(\frac{1}{2} (1 + \cos^2(\Phi) + 2 \cos(\Phi)) - \frac{1}{2} 2^2 - 3(\cos(\Phi) - 1) \right. \\
 &\quad \left. + 2 \ln \left(\frac{1 + \cos(\Phi)}{2} \right) \right) \tag{B.38}
 \end{aligned}$$

and we see that

$$\begin{aligned}
 &\frac{1}{2} (1 + \cos^2(\Phi) + 2 \cos(\Phi)) - \frac{1}{2} 2^2 - 3(\cos(\Phi) - 1) \\
 &= \frac{1}{2} (1 + \cos^2(\Phi) + 2 \cos(\Phi) + 2 \cos(\Phi) - 2 \cos(\Phi)) - 2 - 3 \cos(\Phi) + 3 \\
 &= \frac{1}{2} (1 + \cos^2(\Phi) - 2 \cos(\Phi)) + 2 \cos(\Phi) - 3 \cos(\Phi) + 1 \\
 &= \frac{1}{2} (1 - \cos(\Phi))^2 + (1 - \cos(\Phi)) \tag{B.39}
 \end{aligned}$$

Finally, the following result is obtained.

$$\begin{aligned}
 f_{z,P1} &= K \left(\frac{1}{2} (1 - \cos(\Phi))^2 + (1 - \cos(\Phi)) + 2 \ln \left(\frac{1 + \cos(\Phi)}{2} \right) \right) \Rightarrow \\
 f_{z,P1} &= \frac{\mu I^2}{4\pi} \left(\frac{1}{2} + \frac{1}{1 - \cos(\Phi)} + \frac{2}{(1 - \cos(\Phi))^2} \ln \left(\frac{1 + \cos(\Phi)}{2} \right) \right) \tag{B.40}
 \end{aligned}$$

B.3 The total electromagnetic force

The total electromagnetic force is given by

$$\begin{aligned}
 f_z &= f_{z,Q} + f_{z,P2} + f_{z,P1} \Rightarrow \\
 f_z &= -\frac{\mu I_d^2}{\pi 16} + \frac{\mu}{4\pi} I_d^2 \ln \left(\frac{r_w}{a \sin(\Phi)} \right) + \frac{\mu I_d^2}{4\pi} \left(\frac{1}{2} + \frac{1}{1 - \cos(\Phi)} \right. \\
 &\quad \left. + \frac{2}{(1 - \cos(\Phi))^2} \ln \left(\frac{1 + \cos(\Phi)}{2} \right) \right) \Rightarrow
 \end{aligned}$$

$$\begin{aligned}
 f_z &= \frac{\mu I_d^2}{\pi 4} \left[-\frac{1}{4} + \ln \left(\frac{r_w}{a \sin(\Phi)} \right) + \frac{1}{2} + \frac{1}{1 - \cos(\Phi)} \right. \\
 &\quad \left. + \frac{2}{(1 - \cos(\Phi))^2} \ln \left(\frac{1 + \cos(\Phi)}{2} \right) \right] \Rightarrow \\
 f_z &= \frac{\mu I_d^2}{\pi 4} \left[\frac{1}{4} - \ln \left(\frac{a \sin(\Phi)}{r_w} \right) + \frac{1}{1 - \cos(\Phi)} \right. \\
 &\quad \left. - \frac{2}{(1 - \cos(\Phi))^2} \ln \left(\frac{2}{1 + \cos(\Phi)} \right) \right] \quad (B.41)
 \end{aligned}$$

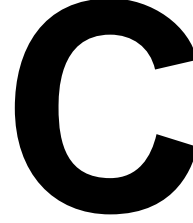
If the axial electromagnetic force F_{em} is defined positive downwards the final result is obtained.

$$\begin{aligned}
 F_{em} &= \frac{\mu I_w^2}{\pi 4} \left[-\frac{1}{4} + \ln \left(\frac{r_d \sin(\Phi)}{r_e} \right) - \frac{1}{1 - \cos(\Phi)} \right. \\
 &\quad \left. + \frac{2}{(1 - \cos(\Phi))^2} \ln \left(\frac{2}{1 + \cos(\Phi)} \right) \right] \quad (B.42)
 \end{aligned}$$

A result that has been derived with respect to the assumptions stated below. Notice, that in Chapter 3, the symbol θ is used instead of Φ for describing the conducting zone.

- The rotational part the electromagnetic forces acting within the drop is neglected. For a discussion of this assumption, see Chapter 3.
- The drop is symmetrical, sphere formed, and has a radius larger than the solid electrode.
- The current is always uniformly distributed.
- The upper surface, Q , is modelled as a cone.
- No current is emitted from the solid part of the electrode, such that $I = I_w = I_d$.

The Pinch Effect



In GMAW, metal is melted from the tip of the electrode and the melted material forms a fluid cylinder as an extension to the solid electrode. For such a liquid system there exists a criterion for which the system becomes unstable, and when this happens, the liquid metal column breaks up into drops. This kind of instability can also be observed when water, running from a water facet, breaks up into drops.

In welding the current, mainly, flows axially in the metal cylinder. This gives a force $\mathbf{J} \times \mathbf{B}$ acting inwards on the cylinder. If the current density, \mathbf{J} , is increased sufficiently it may overcome the stabilizing effect of other forces acting on the liquid cylinder, and this causes the cylinder to collapse inwards. In welding this phenomenon is known as the pinch effect [28, Chapter 3].

From the law of Biot and Savart one get a formula for the relationship between the magnetic field integrated around a conducting wire and the surface integral of the enclosed current.

$$\oint_L \mathbf{B} \cdot d\mathbf{l} = \mu_0 \int_S \mathbf{J} \cdot d\mathbf{s} \quad (\text{C.1})$$

In welding, the current mainly flows axially and symmetrically along the electrode. This means that the field lines lies uniformly distributed around the electrode, and therefore, the equation (C.1) can be rewritten as below.

$$2\pi r B = \mu_0 J \pi r^2 \Leftrightarrow \quad (\text{C.2})$$

$$B = \frac{\mu_0 J \pi r}{2} \quad (\text{C.3})$$

The B-field, B , and the current density, J , are shown in Figure C.1. The current and the self-induced B-field generates a radially electromagnetic force, f_{emr} ,

acting on a small piece of electrode.

$$f_{em,r} = |\mathbf{J} \times \mathbf{B}| = JB = \frac{\mu_0 J^2 \pi r}{2} \quad (\text{C.4})$$

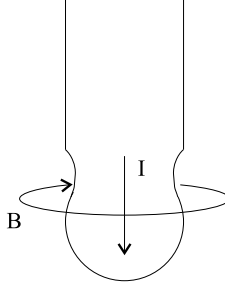


Figure C.1: The current flows axially along the electrode and drop and causes the B-field.

In steady state the electromagnetic force, f_{emr} , is balanced by a radial pressure within the liquid electrode. This means that

$$\frac{\partial p}{\partial r} + \frac{\mu_0 J^2 r}{2} = 0 \quad \Rightarrow \quad (\text{C.5})$$

$$p = -\frac{\mu_0 J^2 r^2}{4} + k \quad (\text{C.6})$$

p is the radial pressure, r is the radial distance from the center of the electrode (or drop), and k is a constant. The constant, k , can be found by considering the boundary conditions. At the surface, at the radial distance $r = R$, the electromagnetic force vanishes, and leaves the pressure to be a sum of the ambient pressure, p_0 , and the pressure due to surface tension of the liquid cylinder. The pressure due to surface tension for a cylinder is $\frac{\gamma}{R}$, where γ is the surface tension coefficient, and R is the radius of the liquid cylinder. Now, the total pressure can be written as

$$p = p_0 + \frac{\gamma}{R} + \frac{\mu_0 J^2}{4}(R^2 - r^2) \quad (\text{C.7})$$

To determine the condition under which the pinch effect occurs instability for a liquid cylinder is considered. Initially, it is assumed that no current is flowing in

the cylinder, however, the cylinder can be described by a frequency determined by the wavelength λ . The radius in such a system can be expressed as

$$r = R + \varepsilon \cos \left(\frac{2\pi}{\lambda} z \right) \quad (\text{C.8})$$

The parameter ε is the amplitude of the sinusoidal-formed liquid surface, and z is the distance in the longitudinal direction. See Figure C.2.

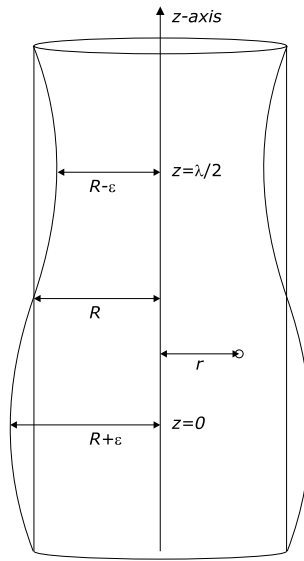


Figure C.2: The cylinder.

The pressure due to surface tension inside a liquid is equal to

$$p_\gamma = \gamma \left(\frac{1}{R_1} + \frac{1}{R_2} \right) \quad (\text{C.9})$$

where R_1 and R_2 are principal radii of curvature for the surface. For a distributed cylinder the pressure in the outward bulge can be expressed as

$$p_{\gamma b} = \gamma \left(\frac{1}{R + \varepsilon} + \frac{1}{R_0} \right) \quad (\text{C.10})$$

where R_0 is the longitudinal radius of curvature at the bulge, and $R + \varepsilon$ is the principal radius of curvature with the circular form, and thus, equals the radius, r , at the bulge. The radius of curvature can be calculated from a geometric relationship between radius and curvature.

$$\frac{1}{R_0} = \frac{\partial^2 r}{\partial z^2} \Big|_{z=0} = \left(\frac{2\pi}{\lambda} \right)^2 \varepsilon \quad (\text{C.11})$$

This gives the following pressure caused by surface tension in the bulged region.

$$p_{\gamma b} = \gamma \left(\frac{1}{R + \varepsilon} + \left(\frac{2\pi}{\lambda} \right)^2 \varepsilon \right) \quad (\text{C.12})$$

Similarly, the pressure caused by surface tension in the pinched region of the cylinder can be derived. This pressure, $p_{\gamma p}$ can be expressed as

$$p_{\gamma p} = \gamma \left(\frac{1}{R - \varepsilon} + \frac{1}{R_{\gamma/2}} \right) \quad (\text{C.13})$$

where

$$\frac{1}{R_{\gamma/2}} = \frac{\partial^2 r}{\partial z^2} \Big|_{z=\lambda/2} = - \left(\frac{2\pi}{\lambda} \right)^2 \varepsilon \quad (\text{C.14})$$

Now, this gives the following expression for the pressure due to surface tension in the pinched region.

$$p_{\gamma p} = \gamma \left(\frac{1}{R - \varepsilon} - \left(\frac{2\pi}{\lambda} \right)^2 \varepsilon \right) \quad (\text{C.15})$$

If the pressure in the bulged region is greater than the pressure in the pinched region, the liquid metal tends to flow from the bulged region to the pinched region. This means that the system is stable. On the other hand, if the pressure is greater in the pinched region, the liquid metal tends to flow from the pinched region to the bulged region, and thus, the system is unstable, and the liquid column breaks into drops. Stability can be expressed as

$$\text{Stable if } p_{\gamma b} - p_{\gamma p} > 0 \quad (\text{C.16})$$

Also, stability can be expressed by the derivative of the pressure in the boundary region between the bulged region and the pinched region. If the derivative, with respect to ε , of the pressure at $\varepsilon = 0$ is greater than zero, liquid metal flows from the bulged region to the pinched region, and thus, the system is stable. However, if the derivative is less than zero the system is unstable.

Stability if

$$\frac{d}{d\varepsilon}(p_{\gamma b} - p_{\gamma p}) > 0 \quad , \quad \varepsilon \rightarrow 0 \quad (\text{C.17})$$

\Rightarrow

$$\left(-\frac{\gamma}{(R + \varepsilon)^2} + \gamma \left(\frac{2\pi}{\lambda} \right)^2 \right) - \left(\frac{\gamma}{(R - \varepsilon)^2} - \gamma \left(\frac{2\pi}{\lambda} \right)^2 \right) > 0 \quad , \quad \varepsilon \rightarrow 0 \quad (\text{C.18})$$

\Rightarrow

$$-\frac{2}{R^2} + 2 \left(\frac{2\pi}{\lambda} \right)^2 > 0 \quad (\text{C.19})$$

\Rightarrow

$$\lambda < 2\pi R \quad (\text{C.20})$$

Now, a criterion have been derived for a liquid cylinder, deformed by the wavelength, λ , but not influenced by radially electromagnetic forces. Including the electromagnetic forces gives the following expression for stability. As before, constants, such as the ambient pressure, are left out.

Stability if

$$\frac{d}{d\varepsilon}(p_{\gamma b} - p_{\gamma p}) > 0 \quad , \quad \varepsilon \rightarrow 0 \quad (\text{C.21})$$

\Rightarrow

$$\frac{d}{d\varepsilon} \left[\left(\frac{\gamma}{R + \varepsilon} + \gamma \left(\frac{2\pi}{\lambda} \right)^2 \varepsilon - \frac{\mu_0 I^2}{4\pi^2 (R + \varepsilon)^2} \right) \right]$$

$$-\left(\frac{\gamma}{R+\varepsilon} + \gamma\left(\frac{2\pi}{\lambda}\right)^2\varepsilon - \frac{\mu_0 I^2}{4\pi^2(R+\varepsilon)^2}\right) > 0, \quad \varepsilon \rightarrow 0 \quad (\text{C.22})$$

$$\Rightarrow$$

$$\begin{aligned} &\left(-\frac{\gamma}{(R+\varepsilon)^2} + \gamma\left(\frac{2\pi}{\lambda}\right)^2 - \frac{\mu_0 I^2}{2\pi^2(R+\varepsilon)^3}\right) \\ &\quad - \left(\frac{\gamma}{(R-\varepsilon)^2} - \gamma\left(\frac{2\pi}{\lambda}\right)^2 + \frac{\mu_0 I^2}{2\pi^2(R-\varepsilon)^3}\right) > 0, \quad \varepsilon \rightarrow 0 \end{aligned} \quad (\text{C.23})$$

$$\Rightarrow$$

$$-2\frac{\gamma}{R^2} + 2\gamma\left(\frac{2\pi}{\lambda}\right)^2 - 2\frac{\mu_0 I^2}{2\pi^2 R^3} > 0 \quad (\text{C.24})$$

$$\Rightarrow$$

$$\left(\frac{2\pi}{\lambda}\right)^2 R^2 > 1 + \frac{\mu_0 I^2}{2\pi^2 \gamma R} \quad (\text{C.25})$$

$$\Rightarrow$$

$$\lambda < \frac{2\pi R}{\left(1 + \frac{\mu_0 I^2}{2\pi^2 \gamma R}\right)^{\frac{1}{2}}} \quad (\text{C.26})$$

Now, a criterion have been derived for the liquid cylinder, deformed by the wavelength, λ , and influenced by radially electromagnetic forces. From the criterion above a critical wavelength, λ_c , can be formulated.

$$\lambda_c = \frac{2\pi R}{\left(1 + \frac{\mu_0 I^2}{2\pi^2 \gamma R}\right)^{\frac{1}{2}}} \quad (\text{C.27})$$

Some assumptions are needed to transform the criterion for instability into a drop detachment criterion for GMAW. In [28, Chapter 7] the following assumptions are made

$$l_d = 0.8\lambda \quad (\text{C.28})$$

$$R = \frac{r_e + r_d}{2} \quad (\text{C.29})$$

$$l_d = nr_d \quad (\text{C.30})$$

l_d is the drop length, r_e is the electrode radius, r_d is the drop radius, and n is a constant. n is set to $(x_d + r_d)/r_d$ as in [21], where x_d is the axial drop extension. Inserting these assumptions into equation (C.27) gives a new criterion for drop detachment, now based on a critical radius, r_{dc} , of the drop. For $\lambda = \lambda_c$ the following final criterion is obtained.

$$r_{dc} = \frac{\pi(r_e + r_d)}{1.25 \left(\frac{x_d + r_d}{r_d} \right) \left(1 + \frac{\mu_0 I^2}{\pi^2 \gamma (r_e + r_d)} \right)^{\frac{1}{2}}} \quad (\text{C.31})$$

$$\text{Drop detachment if } r_d > r_{dc} \quad (\text{C.32})$$

Nomenclature

Symbols

A list of variables, parameters, and constants are given below. Some symbols are assigned a value, and some are not. In general, parameters and constants are assigned a value.

The electrical circuit exclusive the arc

Symbol	Value	Unit	Description
U_c		V	Control voltage.
U_t		V	Terminal voltage.
I, I_w		A	Welding current.
L_m	10e-6	H	Welding machine output inductance.
R_w	0.004	Ω	Total welding wire resistance.
L_w	15e-6	H	Total welding wire inductance.
R_e		Ω	Electrode resistance.
ρ_r	0.2821	Ω/m	Resistivity of the electrode.

The arc

Symbol	Value	Unit	Description
l_a		m	Arc length.
U_a		V	Arc voltage.
U_0	15.7	V	Arc voltage constant.
R_a	0.022	Ω	Arc current coefficient.
E_a	636	V/m	Arc length coefficient.

The electrode

Symbol	Value	Unit	Description
r_e	0.00050	m	Electrode radius.
A_e, A		m	Electrode cross section area.
l_s		m	Electrode stick out.
ρ_e, ρ	7860	kg/m^3	Electrode density.

Nomenclature

The drop states

Symbol	Value	Unit	Description
x_d		m	Drop displacement.
v_d		m	Drop velocity.
m_d		kg	Drop mass.

The forces acting on the drop

Symbol	Value	Unit	Description
F_{em}		N	Force due to electromagnetic induction.
F_g		N	Force due to gravity.
F_m		N	Force due to momentum.
F_d		N	Force due to aerodynamic drag.
F_s		N	Surface tension force.

Other symbols related to the drop

Symbol	Value	Unit	Description
r_d		m	Drop radius.
k_d	3.5	N/m	Drop spring constant.
b_d	0.0008	kg/s	Drop damping constant.
μ_0	1.25664e-6	(kg m)/(A ² s ²)	Permeability of free space.
γ_{st}	2	N/m ²	Surface tension of liquid steel.
θ	$\pi/2$	rad	Conducting area.
A_d		m ²	Drop area not covered by the electrode.
C_d	0.44	-	Drag coefficient.
v_p	10	m/s	Relative fluid to drop velocity.
ρ_p	1.6	kg/m ³	Plasma density.

Static electrode melting

Symbol	Value	Unit	Description
M_R		m ³ /s	Melting rate.
v_m		m/s	Melting speed.
c_1	2.885e-10	m ³ /(A s)	Melting rate constant.
c_2	5.22e-10	m ² /(A ² s)	Melting rate constant.
k_1		m/(A s)	Melting speed constant.
k_2		(A ² s) ⁻¹	Melting speed constant.

Dynamic electrode melting

Symbol	Value	Unit	Description
T		$^{\circ}\text{C}$	Temperature.
T_0	20	K	Ambient temperature.
T_m	1427	K	Melting temperature.
T_d		K	Drop temperature.
h_m	2.5e+5	J/kg	The heat of fusion.
h		J/kg	Specific inner energy.
h_d		J/kg	Specific inner energy of the drop.
c	510	J/(kg K)	Specific heat capacity, below T_m .
c_m	510	J/(kg K)	Specific heat capacity, above T_m .
P_a		J/s	The anode heat flow (flux).
P_d		J/s	The drop heat flow (flux).
P_l		J/s	Thermal conduction heat flow (flux).
P_J		J/s	Ohmic heat flow (flux).
c_{an}		-	Anode heat constant.
V_{an}		V	Anode voltage.
ϕ_w		V	The work function.
K_c	0.267	J/K	Drop convection constant.
E_p		J	Inner energy.
λ	17	W/(m K)	Thermal conductivity.
ψ	0.2821	Ω/m	Resistivity of the electrode.

The Control architecture

Symbol	Value	Unit	Description
I_m		A	Measured welding current.
U_{tm}		V	Measured terminal voltage.
l_{am}		m	Estimated arc length.
l_{ar}		m	Arc length reference.
I_{rc}		-	Output from the arc length controller.
I_r		A	Reference input to the current controller.

Other symbols

Symbol	Value	Unit	Description
τ_i	1/15000	s	Approximated current dynamics time constant.
l_c		m	Contact tip (or tube) to workpiece distance.
v_e		m/s	Wire feed speed.

Abbreviations

GMAW	Gas Metal Arc Welding.
GTAW	Gas Tungsten Arc Welding.
SMAW	Shielded Metal Arc Welding.
MMA	Manual Metal Arc (stick welding).
MIG	Metal inert Gas.
MAG	Metal Active Gas.
TIG	Tungsten Inactive Gas.
PIT	Pinch Instability Theory.
SFBM	Static Force Balance Model.
SFBM	Dynamic Force Balance Model.

Other

Matlab	A high-level technical computing language from MathWorks.
Simulink	Platform for simulation and model-based design of dynamic systems from MathWorks.

Bibliography

- [1] M. AbdelRahman. Feedback linearization control of current and arc length in gmaw system. *Proc. of the American Control Conference*, 1998.
- [2] J.A. Johnson A.D. Watkins, H.B. Smartt. A dynamic model of droplet growth and detachment in gmaw. In *Recent Trends in Welding Science and Technology*. ASM, 1992.
- [3] C.J. Allum. Metal transfer in arc welding as a varicose instability: I. varicose instabilities in a current-carrying liquid cylinder with surface charge. *J. Phys. D: Appl. Phys.*, (18):1431–1446, 1985.
- [4] C.J. Allum. Metal transfer in arc welding as a varicose instability: Ii. development of model for arc welding. *J. Phys. D: Appl. Phys.*, (18):1447–1468, 1985.
- [5] J.C. Amson. Lorentz force in the molten tip of an arc electrode. *Brit. J. Appl. Phys.*, 16:1169–1179, 1965.
- [6] T. Klein G. Simon B. Rethfeld, J. Wendelstorf. A self-consistent model for the cathode fall region of an electric arc. *J. Phys. D: Appl. Phys.*, (29):121–128, 1996.
- [7] Henrik Vie Christensen. *Student project: Control of Melting Velocity for MIG Welding Device*. Department of Control Engineering, Aalborg University, 2002.
- [8] G.E. Cook. Keynote address - decoupling of weld variables for improved automatic control. pages 1007–1015, 1998.
- [9] K.L. Moore D.S. Naidu. Automatic control strategies for gas metal arc welding: A status survey. In *Trends in Welding Research: Proc. 5th International Conference*, pages 1027–1032, 1998.
- [10] K.L. Moore D.S. Naidu, S. Ozcelik. *Modeling, Sensing and Control of Gas Metal Arc Welding*. Elsevier, 2003.
- [11] J.A. Johnson H.B. Smartt T. Harmer K.L. Moore E.W. Reutzel, C.J. Eirson. Derivation and calibration of a gas metal arc welding (gmaw) dynamic droplet model. In *Trends in Welding Research*, pages 377–384. Proc. of the 4th International Conference, 1995.
- [12] Abbas Emami-Naeini Gene F. Franklin, J. David Powell. *Feedback Control of Dynamic Systems*. Addison-Wesley, third edition, 1994.

BIBLIOGRAPHY

- [13] H. Ebrahimirad A.E. Ashari H. Jalili-Kharaajoo, V. Gholampour. Robust nonlinear control of current and arc length in gmaw systems. *Proc. Conference on Control Applications*, 2:1313–1316, 2003.
- [14] J. Haidar. An analysis of the formation of metal droplets in arc welding. *J. Phys. D: Appl. Phys.*, (31):1233–1244, 1998.
- [15] N.M. Carlson M. Waddoups J.A. Johnson, H.B. Smartt. Dynamics of droplet detachment in gmaw. In *Trends in Welding Research: Proc. 3th International Conference*, pages 987–991.
- [16] C.D. Yoo J.H. Choi, J. Lee. Dynamic force balance model for metal transfer analysis in arc welding. *J. Phys. D: Appl. Phys.*, (34):2658–2664, 2001.
- [17] M.J. Piena J.H. Waszink. Experimental investigation of drop detachment and drop velocity in gmaw. *Welding Research Supplement*, November 1986.
- [18] K. Glover K. Zhou, J.C. Doyle. *Robust Optimal Control*. Prentice-Hall, 1996.
- [19] Hassan K. Khalil. *Nonlinear Systems*. Prentice-Hall, third edition, 2002.
- [20] D.S. Naidu K.L. Moore, M.A. Abdelrahman. Gas metal arc welding control: Part 2 – control strategy. *Nonlinear Analysis*, (35):85–93, 1999.
- [21] R. Yender J. Tyler K.L. Moore, D.S. Naidu. Gas metal arc welding control: Part 1 – modeling and analysis. In *Nonlinear Analysis, Methods and Applications*, volume 30, pages 3101–3111. Proc. 2nd World Congress of Nonlinear Analysts, 1997.
- [22] R. Yender J. Tyler K.L. Moore, D.S. Naidu. Modeling, calibration, and control-theoretic analysis of the gmaw process. In *Nonlinear Analysis, Methods and Applications*, volume 3, pages 1747–1751. Proc. American Control Conference (ACC), 1998.
- [23] R.F. Yender J. Tyler S. Ozcelik K.L. Moore, D.S. Naidu. Experimental calibration of an automated gmaw model. In *Trends in Welding Research: Proc. 5th International Conference*, pages 314–319, 1998.
- [24] D. Weiss T.W. Eagar L.A. Jones, P. Mendez. Dynamic behavior of gas metal arc welding. In *9th Conf. on Iron and Steel Technology*, 1997.
- [25] J.H. Lang L.A. Jones, T.W. Eagar. The temporal nature of forces acting on metal drops in gas metal arc welding. In *Trends in Welding Research: Proc. 4th International Conference*, pages 365–370, 1995.
- [26] J.H. Lang L.A. Jones, T.W. Eagar. A dynamic model of drops detaching from a gas metal arc welding electrode. *J. Phys. D: Appl. Phys.*, (31):107–123, 1998.

-
- [27] J.H. Lang L.A. Jones, T.W. Eagar. Magnetic forces acting on molten drops in gas metal arc welding. *J. Phys. D: Appl. Phys.*, (31):93–106, 1998.
- [28] J.F. Lancaster. *The Physics of Welding*. Pergamon Press, 1984.
- [29] A. Lesnewich. Control of the melting rate and metal transfer in gas shielded metal arc welding, part i. *Welding Research Supplement*, pages 343–353, August 1958.
- [30] A. Puklavec B. Torvornik M. Golob, A. Koves. Modelling, simulation and fuzzy control of the gmaw welding proces. In *15th Triennial World Congr. Int. Fed. of Automatic Control*, 2002.
- [31] J. Tusek M. Suban. Dependence of melting rate in mig/mag welding on the type of shielding gas used. *Journal of Materials Processing Technology*, (119):185–192, 2001.
- [32] P.E. Murry. Stability of a pendant droplet in gas metal arc welding. In *Trends in Welding Research: Proc. 5th International Conference*, pages 308–313, 1998.
- [33] V.A. Nemchinsky. Size and shape of the liquid droplet at the molten tip of an arc electrode. *J. Phys. D: Appl. Phys.*, (27):1433–1442, 1994.
- [34] V.A. Nemchinsky. The effect of the type of plasma gas on current constriction at the molten tip of an arc electrode. *J. Phys. D: Appl. Phys.*, (29):1202–1208, 1996.
- [35] V.A. Nemchinsky. Heat transfer in a liquid droplet hanging at the tip of an electrode during arc welding. *J. Phys. D: Appl. Phys.*, (30):1120–1124, 1997.
- [36] V.A. Nemchinsky. Electrode melting during arc welding with pulsed current. *J. Phys. D: Appl. Phys.*, (31):2797–2802, 1998.
- [37] V.A. Nemchinsky. Heat transfer in an electrode during arc welding with a consumable electrode. *J. Phys. D: Appl. Phys.*, (31):730–736, 1998.
- [38] V.A. Nemchinsky. The rate of melting of the electrode during arc welding, the influence of discrete removal of the melt. *J. Phys. D: Appl. Phys.*, (31):1565–1569, 1998.
- [39] S. Tøffner-Clausen P. Andersen, T.S. Pedersen. *Dynamiske modeller af termiske systemer*. Department of Control Engineering, Aalborg University, 1996.
- [40] J. Dowden P. Solana, P. Kapadia. A mathematical model for the stochastic behaviour of species near the cathode in arc welding. *J. Phys. D: Appl. Phys.*, (30):871–878, 1997.

BIBLIOGRAPHY

- [41] S.W. Simpson P. Zhu. Theoretical study of a consumable anode in a gas metal welding arc. In *Trends in Welding Research, Proc. 4th Int. Conf.* Proc. 4th International Conference, 1995.
- [42] S.W. Simpson P. Zhu, M. Rados. A theoretical study of a gas metal arc welding system. *Plasma Sources Sci. Tech.*, (4):495–500, 1995.
- [43] S.W. Simpson Q. Lin, X. Li. Metal transfer measurements in gas metal arc welding. *J. Phys. D: Appl. Phys.*, (34):347–353, 2001.
- [44] J. Dowden M. Thornton I. Richardson R. Ducharme, P. Kapadia. A mathematical model of the arc in electric arc welding including shielding gas flow and cathode spot location. *J. Phys. D: Appl. Phys.*, (28):1840–1850, 1995.
- [45] S.D. Naidu J. Tyler S. Ozcelik, K.L. Moore. Classical control of gas metal arc welding. In *Trends in Welding Research: Proc. 5th International Conference*, pages 1033–1038, 1998.
- [46] B. Nuon S. Ramakrishnan. Prediction of properties of free burning welding arc columns. *J. Phys. D: Appl. Phys.*, (13):1845–1853, 1980.
- [47] D.R. White S. Subramaniam. Study of droplet surface tension and plasma forces in overhead position pgmaw. In *Trends in Welding Research: Proc. 5th International Conference*, pages 320–325, 1998.
- [48] Subbaram D. Naidu Selahattin Ozcelik, Kevin L. Moore. Application of mimo direct adaptive control to gas metal arc welding. *Proc. of the American Control Conference*, 1998.
- [49] Ian Postletwaite Sigurd Skogestad. *Multivariable Feedback Control*. John Wiley & Sons, 1996.
- [50] Y.S. Kim S.K. Choi, C.D. Yoo. The dynamic analysis of metal transfer in pulsed current gas metal arc welding. *J. Phys. D: Appl. Phys.*, (31):207–215, 1998.
- [51] Y.S. Kim S.K. Choi, C.D. Yoo. Dimensional analysis of metal transfer in gma welding. *J. Phys. D: Appl. Phys.*, (32):326–334, 1999.
- [52] B.L. Walcott Y.M. Zhang, Liguó E. Active metal transfer control by monitoring excited droplet oscillation. *Welding Research Supplement*, September 1998.
- [53] B.L. Walcott Y.M. Zhang, Liguó E. Interval model based control of gas metal arc welding. *Proc. of the American Control Conference*, 1998.
- [54] B.L. Walcott Y.M. Zhang, Liguó E. Robust control of pulsed gas metal arc welding. *Journal of Dynamic Systems, Measurement and Control*, 124(2):281–289, 2002.

- [55] E. Liguó Y.M. Zhang. Numerical analysis of the dynamic growth of droplets in gas metal arc welding. In *Proc. Instn Mech Engrs*, volume 214, 2000.
- [56] P.J. Li Y.M. Zhang. Modified active metal transfer control and pulsed gmaw of titanium. *Welding Research Supplement*, February 2001.
- [57] G.E. Cook Z. Bingul. Dynamic modeling of gmaw process. In *Int. Conf. on Robotics Automation*, 1999.
- [58] R.J. Barnett A.M. Strauss B.S. Wells Z. Bingul, G.E. Cook. An investigation of constant potential gmaw instability behavior. In *Trends in Welding Research: Proc. 5th International Conference*, pages 289–294, 1998.
- [59] P. Zhu. Keynote address - computer simulation of gas metal welding arcs. In *Trends in Welding Research: Proc. 5th International Conference*, pages 283–288, 1998.

